1. REPORT NO.	2. GOVERNMENT ACCESSION NO.	3. RECIPIENT'S CATALOG NO.
WA-RD 581.1		

4. TITLE AND SUBTITLE	5. REPORT DATE
Investigation of Flow and Local Scour Characteristics around a Partially Submerged Permeable WSDOT Barb	February 2004
	6. PERFORMING ORGANIZATION CODE

7. AUTHOR(S)	8. PERFORMING ORGANIZATION REPORT NO.
A.N. Thanos Papanicolaou, Lisa J. Kjos, James F. Fox	

9. PERFORMING ORGANIZATION NAME AND ADDRESS	10. WORK UNIT NO.
Washington State Transportation Center (TRAC) Civil and Environmental Engineering Sloan Hall, Room 101 Washington State University Pullman, Washington 99164-2910	11. CONTRACT OR GRANT NO. T2696-03

12. SPONSORING AGENCY NAME AND ADDRESS	13. TYPE OF REPORT AND PERIOD COVERED
Research Office Washington State Department of Transportation Transportation Building, MS 7370 Olympia, Washington 98504-7370 Kathy Lindquist, Project Manager, (360)705-7976 Rocio (Rose) Peralta, Technical Monitor	Final Report 14. SPONSORING AGENCY CODE

15. SUPPLEMENTARY NOTES

This study was conducted in cooperation with the U.S. Department of Transportation, Federal Highway Administration.

Dr. Thanos Papanicolaou and James F. Fox have moved to the University of Iowa, IIHR. Mrs. Lisa Kjos is with the WSDOT

16. ABSTRACT

Barbs are wide crested trapezoidal structures, typically constructed of riprap gravel, which project out from the streambank and are oriented upstream into the main flow. Barbs reduce erosion along streambanks by defelcting current into the center of the channel aiding in the protection of bridge piers and abutments. The overall objective of this study is to establish design criteria for permeable barbs within non-navigable mild sloped gravel bed streams. The report consists of two major parts. Part one focuses on the flow characteristics around a submerged permeable barb to understand the flow regimes "formed" within the vicinity of a barb. Part two utilizes the quantitative data that are gathered in part one and investigates the complex evolution of local scour around the permeable barb under clear-water scour conditions.

17. KEY WORDS	18. DISTRIBUTION STATEMENT
Key words: permeable and impermeable barbs, Scaling, time-averaged flow and turbulent parameters, backwater analysis, scour depth	No restrictions. This document is available to the public through the National Technical Information Service, Springfield, VA 22616

19. SECURITY CLASSIF. (of this report)	20. SECURITY CLASSIF. (of this page)	21. NO. OF PAGES	22. PRICE
None	None		

Acknowledgements

The researchers gratefully acknowledge the technical assistance and support from the Tecnhical Advisory Committee, and especially the contributions of the following people during the planning, development, and execution of this project:

Rose Peralta	Washington State Dept. of Transportation
Matt Witecki	Washington State Dept. of Transportation
Kathy Lindquist	Washington State Dept. of Transportation
Bob Winter	Washington State Dept. of Transportation
Jim Fox	General Contractor, Akron, Ohio
Casey Kramer	Undergraduate Research Assistant at WSU
Brandon Hobbs	Undergraduate Research Assistant at WSU
Randy Dinehart	USGS Scientist, Sacramento, CA

Organization of this Report

This report consists of two parts. The first part focuses on the qualitative and quantitative description of flow around an impermeable and permeable barb of identical shape and size over a fixed roughness bed. The conclusions from the first part are: 1) Three main flow regimes form around both impermeable and permeable barbs; 2) The permeable barb performs better "hydraulically" and "ecologically" and no further studies of the impermeable barb are required. The second part focuses on scour around only the permeable barb. The evolution of scour hole is tested for various flow conditions and various relative submergences. A scour formula applicable to mild sloped, gravel-bed streams is developed.

1. Introduction

1.1 Stream Barbs – Definition and Purpose

Barbs are defined as wide crested trapezoidal-shaped structures that project out from the streambank into the main channel flow. Typically, constructed of large angular rock (riprap); barbs protrude into the flow at an angle upstream to the channel sidewall (bank) for the purpose of deflecting current away from the bank and minimizing the erosion potential (Ghodsian and Tehrani, 2001; Breusers and Raudkivi, 1991). Barbs are typically designed to incorporate beneficial elements of existing hydraulic structures with the intent to be used specifically in non-navigable, mild-sloped, gravel-bed streams typical of the state of Washington and surrounding Pacific Northwest. In addition to bank protection, barbs can be used to enhance aquatic habitat by creating resting pools for fish organisms (Kuhnle et al., 2002; Shamloo et al., 2002; Mayerle et al., 1995; Przedwojski et al., 1995; Klingeman et al., 1984).

1.2 Stream Barbs – Current Uses in Washington State

The Washington State Department of Transportation (WSDOT) has employed barbs for bank protection along highways or river crossings and/or to improve aquatic conditions, especially in shallow gravel bed streams. Such examples include the Wenatchee River along state route (SR) 2 and SR 207; Newaukum River along SR 5 and SR 508 (South fork); Snoqualmie River along SR 202; and the North Fork of the Toutle River along SR 504. While barbs are quite similar to spur dikes, groynes (groins), and submerged vanes, they have some distinct features. The most defining feature is the trapezoidal shape of the structure with inclined sides and a wide sloped crest, which allows the barb to 'behave" as a partially submerged structure (weir) when flow is low and fully submerged when bankfull flow conditions are present. When pointed upstream the submerged "weir section" forces the water flowing over the structure into a hydraulic jump (Fox, 2002). The flow separation induced by the hydraulic jump promotes the formation of eddies and sediment deposition on the leeward side of the barb (Lloyd and Stansby, 1997).

Other distinguishing features of barbs include the riprap material composition of the structure and fixed angle with respect to the channel sidewall or bank. Based on the degree of riprap gradation, the induced permeability aids in flow dissipation and minimizes backwater effects along with the effects of flow acceleration on local scour. Furthermore, an optimal fixed angle with respect to the channel sidewall of 130-degrees (50-degree from the upstream, or equivalently 130-degree to the downstream, channel sidewall) has been reported to have the best potential for providing suitable habitats for aquatic organisms while minimizing the effects of currents on bank erosion (Kuhnle et al., 2002).

1.3 Critical Review of Literature

Although there is a vast amount of research that has been done for flows around hydraulic structures (primarily when non-submerged conditions are present), the majority

of the investigations have treated flow, around these structures, in a rather time-averaged sense. As a result, research focus is placed on mean flow variables without considering the unsteady nature of turbulent flow around these structures and the non-uniform spatial characteristics of the flow. Subsequently, estimations of the bed shear stress around a structure are mainly based on the consideration that flow around these structures is unidirectional and steady, which leads to miscalculation of scour volume quantities in the vicinity of a structure (Whitehouse, 1998; Kuhnle et al., 2003). Moreover, estimation of the depth of local scour around a structure, such as a barb, remains a perplex problem for hydraulic and restoration engineers and reliable scour formulas (especially for gravel bed streams) are lacking. This is attributed to two primary reasons: (i) an oversimplification of the flow field in the vicinity of a barb by considering steady unidirectional and in some cases uniform flow conditions as mentioned earlier and (ii) most investigations have just reported measurements of the maximum depth of scour without giving any information about the geometry (i.e. shape) of the scour hole and how this geometry changes with time (Kuhnle et al., 2002).

As reported by Kothyari and Raju (2000), the primary focus of previous investigations, such as, Gill (1972), Garde et al. (1961), Liu et al. (1961), Laursen and Toch (1956), and Ahmad (1953), on the study of scour at abutments and spur dikes was to predict an equilibrium or maximum design scour depth. Few studies have been performed which measured the velocity distribution associated with spur dikes and scour holes and none to the author's knowledge which measure the 3-dimensional (3-D) nature of flow in the vicinity of the structures as the scour hole evolves. Coupling of scour measurements with near bed-turbulent flow parameters is imperative for the development of scour formulas that incorporate the transient nature of flow in the vicinity of a structure where reportedly the bed shear stress becomes amplified by a factor of 4-5 (Ahmed and Rajaratnam, 2000; Kothyari and Raju, 2000; Whitehouse, 1998; Dongol, 1993).

Once the above pre-mentioned are addressed, it is expected that the stability issues of barbs will not be based on time-averaged flow quantities but on turbulent quantities. In addition, inclusion of turbulent flow parameters in the design of barbs will lead to the development of scour formulas that do not underestimate scour depth around a structure. The sections that follow below elaborate further on the existing knowledge that has been gathered on interaction of flow, structure and sediment and outline the current research limitations. The objectives of this study are then formed based on well-founded hypotheses.

1.4 Interaction of Structure and Flow

Quantitative research has been conducted on hydraulic structures such as embankments, weirs, bluff bodies, and islands by several researchers (e.g., Ohtsu et. al., 1997; Wu and Rajaratnam, 1996) to improve our understanding regarding the interaction of these structures with flow. It has been suggested (e.g., Fox, 2003; Chen and Ikeda, 1997; Schmidt et al., 1993) that the 3-D flow field is, typically, comprised of distinct flow regimes, namely, the main core flow, the wake region, and the shear layer region.

Dongol (1993) and Kwan (1988), among others, provided the flow microstructure within the aforementioned flow regimes, for the case of unsubmerged bridge abutments. According to Kwan, the flow around abutments is a complex system of vortices, namely a back eddy (or downflow) vortex, a primary vortex, secondary vortices, and wake vortices. The back eddy vortex forms as flow encounters the frontal face of the structure and is forced downward toward the bed in a jet motion impinging on the bed. The downflow is further deflected up parallel to the bottom surface of the structure forming the primary vortex. Coupled with the deflected up back eddy flow the primary vortex forms in the main core flow and is pushed around the tip of the structure in a continuation of scour along the bed surface. These frontal vortices are further coupled with secondary vortices due to flow constriction from the presence of the abutment (Papanicolaou and Hilldale, 2002), and lastly, wake vortices formed at the downstream end of the abutment. Boundaries of the stagnant wake region are defined by the secondary and wake vortices. Figure 1.1 provides a sketch of the vortex microstructures around an abutment.

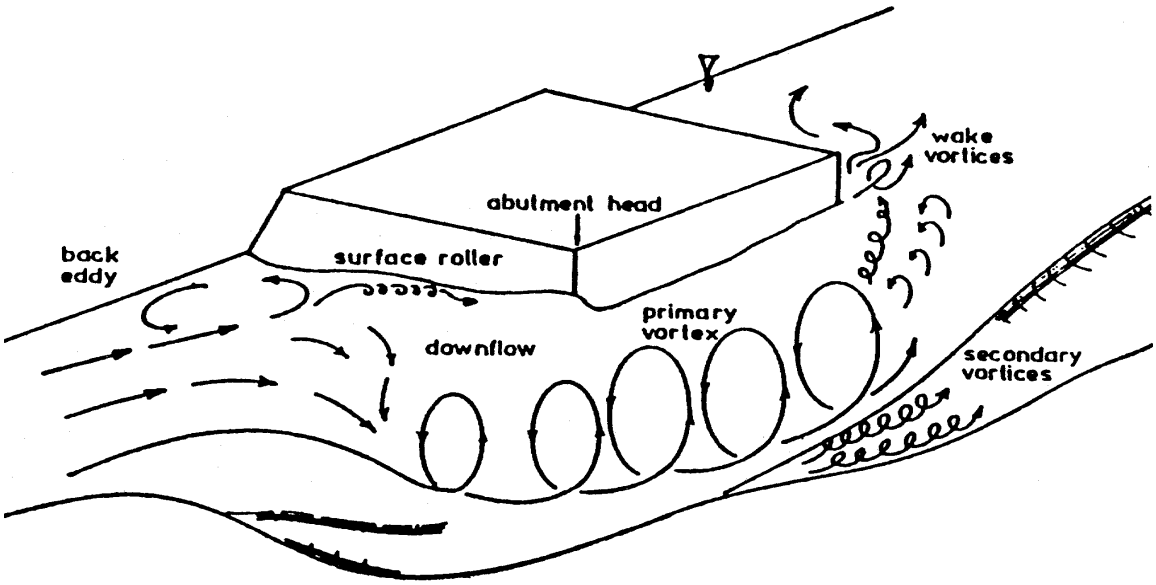

Figure 1. Schematic of Vortex Microstructure Around Abutment (after Kwan, 1984)

The pioneering work of Lloyd and Stansby (1997) further extended such research by investigating submerged flow regimes for embankment-shaped weirs. In the latter case, due to flow overtopping of the structure four transitional regimes are identified to form: (1) a hydraulic jump, (2) plunging jet, (3) surface wave, and (4) surface jet. These transitional regimes are predominately formed between the stagnant wake and shear layer regions as defined in Figure 2.

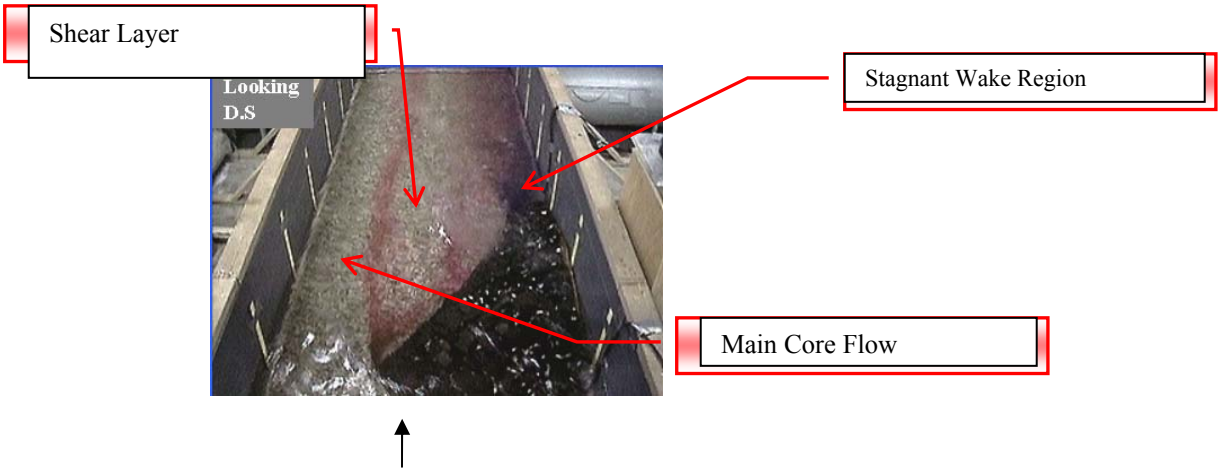

Figure 2. Flow Around Barb Using Dye Depicting 3 Flow Regions

In figure 2 the barb is aligned along the channel sidewall in the longitudinal direction. The main core flow extends from the tip of the barb to the main channel flow and occurs within the channel longitudinal direction. The wake region regime, a stagnant flow region, is found to form behind the structure and along the downstream near the sidewall. The shear layer region is formed between the stagnant wake region and the accelerating main core flow.

1.5 Interaction of Flow and Sediment Movement

The process of fluid dynamics and sediment transport is characterized by the inherent physical properties of each combined with the interactive nature between flow and sediment movement. The local patterns and magnitudes of flow and sediment are further compounded in the vicinity of hydraulic structures. As stated by Melville and Coleman (2000), localized changes include those due to the presence of the structure (local scour) and those due to geometric alterations of the stream (contraction scour). This compilation of scour processes occurs simultaneously and is challenging to distinguish them apart (Wallerstein, 2003; Melville and Coleman, 2000). Therefore, the interaction between flow and sediment in the vicinity of a structure is often referred to as localized scour.

1.6 Research Limitations

The above literature survey clearly indicates the complicated nature of the flow around submerged or non-submerged structures and explains why very few attempts have been made to quantitatively describe the 3-D nature of turbulence around these structures for design considerations. Furthermore, it highlights the need for an accurate representation of the bed shear stress in hydrodynamic and scour simulations when complex flow regimes are eminent. Not accounting for the interaction between flow and sediment movement (eroding mobile bed) could result in under/over prediction of scour volume around a structure.

Based on the above, it is not surprising that existing scour formulas are mainly empirical, lack a theoretical basis, and do not incorporate the unsteady nature of flow around structures. Considerable information is available on the prediction of the maximum scour depth around impermeable non-submerged hydraulic structures. To date, however, less attention has been paid to the study of other scour hole characteristics. Existing design considerations do not incorporate the rate at which the geometry of a scour hole associated with submerged barbs changes with time by accounting for the continuous feedback between flow and sediment. Recent prominent research by Wallerstein (2003), Kuhnle et al. (2003) and Lim and Chiew (1992) partially addressed this issue by attempting to predict the temporal evolution of scour hole geometry (not only the maximum depth) in a sand bed mixture. Still though, none of the above studies have examined the complex hydrodynamic conditions associated with the evolution of a scour hole. This is primarily attributed to the high degree of difficulty involved in obtaining simultaneous flow and scour measurements over an area. Conventional experimental techniques such as Acoustic Doppler Velocimetry (ADV) and Laser Doppler

Velocimetry (LDV) along with point gauge measurements provide point specific information about flow and scour, respectively. Nonetheless, by their nature, these techniques do not facilitate simultaneous aerial flow and scour analysis. Furthermore, very few studies have examined the effects of permeability and submergence of the structure in scour measurements over gravel beds (Ghodsian and Tehrani, 2001).

The most recent advancements made using image analysis techniques to monitor bed changes and scour hole evolution coupled with the development of state-of-the-art Large Scale Particle Image Velocimetry (LSPIV) allow the performance, at least at the laboratory level, of capturing simultaneous aerial flow and scour measurements. Although underwater cameras allow unimpeded mapping of the changes in the bed bathymetry, LSPIV algorithms provide free-surface velocities spanning over larger areas, such as scour holes. LSPIV also accounts for changes in the turbulent velocity magnitude due to scour-hole formation and evolution when synchronized with bed measurements.

2. Scope and Objectives

The overreaching goal of this research, through the use of powerful experimental techniques, such as, ADV and LSPIV, is to examine the complex hydrodynamic conditions associated with the geometric evolution of scour around a barb. To illustrate the effects of scour evolution, this paper provides unique hydrodynamic information for a test performed under equivalent bulk flow conditions, when a barb is placed upon both an immobile and mobile gravel bed of identical roughness. Several techniques to determine the bed shear stress distribution are considered, analyzed and compared during the course of this research. Dimensional analysis is employed to provide a general expression for scour depth as a function of the governing parameters (e.g. flow, sediment size and gradation, and flow depth). This analysis is complemented with clear water scour tests performed for a wide range of flow conditions (starting from almost a non-submerged condition to almost fully submerged barb condition). During these tests, rates of cumulative scour volume changes are recorded due to local and constriction scour effects. These rates are used to develop generic scour relations for clear water conditions by indirectly accounting for the effects of stress amplification due to the presence of complex vortical structures.

In summary, the objectives of this investigation are: (1) establishment of model scaling methodology and the experimental setup and construction of the model; (2) analysis of the time-averaged flow parameters, Reynolds stresses, and other turbulence parameters in the immediate downstream vicinity of the model barb; (3) develop a generic scour equation that predicts the evolution of the scour hole volume and depth in gravel beds under varied flow conditions; (4) analyze available methods and determine the best predictive shear stress results for varied flow regimes; (5) examine the effects of relative submergence, with a permeable barb, on scour hole predictions, and (6) determine for the first time free-surface aerial flow measurements as the scour hole evolves and compare it to an equivalent flow over a fixed roughness, (7) assess optimal barb streambank protection and spacing criteria using large scale particle image velocimetry.

Comparisons of the results of this study will be made with other studies that closely represent the experimental work of this research.

The ultimate goal of the current research at Washington State University is to establish design criteria for barbs within non-navigable, mild sloped, gravel-bed streams. Specifically, the barbs are investigated for high flow conditions when bridge pier and abutment scour and streambank migration are most damaging. The objectives and tasks per objective are described in a great detail below.

3. Objective 1: Establishment of model scaling methodology and the experimental setup and construction of the model

When performing an experimental case study, that is, modeling and analyzing a specific occurrence within a specific site, it is necessary to replicate field conditions as closely as possible.

The WSDOT has recommended a new design for rock barbs that is applicable to non-navigable, mild-sloped, gravel bed streams in the Pacific Northwest. Therefore, assessment of such streams is necessary in order to ensure that pertinent hydraulic and geomorphologic parameters are included within the scaling process. Previous sites where barbs were utilized by the Washington State Department of Transportation (WSDOT) were researched and the available data pertaining to such streams was compiled. Ultimately, the North Fork of the Toutle River in Cowlitz County, Washington (illustrated in Figure 3) was designated as a representative prototype stream due to the multiple barb constructions along its course, as well as the availability of its river characteristic data including its discharge, channel dimensions, and particle size distribution. The flow data for the North Fork are obtained from the United State Geological Survey (USGS) gaging station and research reach located near Kid Valley, Washington. This area has been strictly monitored since the early 1980s because of its close proximity to the active volcano Mt. St. Helens. The stream data is published in the State of Washington Water Resources Records by the USGS, at www.wa.usgs.gov., and in Dinehart (1992).

Figure 3. North Fork of the Toutle River

The design discharge of the prototype was determined by assessing mean monthly flow rates averaged over a 14-year period. Historical data for the North Fork of the Toutle River was obtained from the *State of Washington Water Resources* records for the 1981-1995 water years. During this period a failure of three barbs along the North Fork of the Toutle River was reported by WSDOT. Upon consultation with the DOT personnel the highest mean monthly flow was considered here as the representative design flow event for barbs of the proposed WSDOT design. At higher flows, the usefulness of barbs was considered minimal since barbs became fully submerged to the flow. The highest mean monthly flow rate occurs in February, when discharge reaches 2,028 cfs.

The prototype average bed slope (S= 0.00377) and channel width (w= 74 feet) were obtained from www.wa.usgs.gov. Because the streambank slope was unknown, it was assumed to be 45-degrees, while the gradation of bedload sediment within the prototype was obtained from Dinehart (1992). Dinehart also provided values for the phi-scale sorting index (1.68) and the bedload D_{50} (28 mm). The specific gravity of the sediment was assumed to be 2.65, a typical value for gravel. Hydraulic and roughness calculations were performed for the prototype assuming steady, uniform flow. In addition, water viscosity and density were based on a water temperature of 40-degress F.

The prototype Manning's roughness coefficient, n, was calculated using the equation of Anderson (1970) to be 0.0265. Anderson's equation is:

$$n = 0.0395\, D_{50}^{1/6} \qquad (1)$$

where D_{50} is the mean particle diameter. This equation was developed using data from laboratory flumes and natural rivers with angular and rounded stones 0.0005 – 1.0 feet in diameter for channel slopes < 1% (Rice et al. 1998). The relationship is independent of slope and depth of flow, and assumes a straight, stable channel with uniform flow. Therefore, this relation was used to scale the sediment size well-upstream of the barb.

Using design discharge, channel geometry, and roughness, the normal depth of the prototype was calculated with the Manning's Equation and determined to be 3.5 feet. In English units, Manning's Equation follows:

$$Q = (1.49/n)\, A\, R^{2/3}\, S^{1/2} \qquad (2)$$

where Q is the fluid discharge, A is the channel cross-sectional area, R is the hydraulic radius, and S is the energy slope. Manning's Equation was pertinent because it is valid for lowland rivers experiencing steady, uniform flow (Chang 1998). The friction velocity, u^*, was calculated to be 0.65 fps using the relationship:

$$u^* = (g\, H\, S)^{1/2} \qquad (3)$$

where g is gravitational acceleration and H is water depth. This relation is valid for a wide channel where bedforms are not present. Using the design discharge and normal depth, the bulk velocity was determined to be 7.52 fps, when:

$$V = Q\,A \tag{4}$$

Barb Prototype

The prototype barb geometric dimensions and orientation within the stream are based on the barb design presented by the WSDOT. A description of the WSDOT barb based on *the WSDOT Hydraulic Manual* and cut-sheets for barbs constructed in Washington follows:

> *"The barb should extend upstream one-third of the way into the channel at a 50 degree angle. The barb crest should be located at 1.5 feet above the streambed at the nose (this corresponds to low flow). The crest should rise at a 10:1 slope for the first 15 feet from the nose at which time the slope should break and continue at a slope necessary for the barb crest to meet the top of the bank, typically a 4:1 or 5:1 slope. At the bank, a 5 feet (streamwise) by 10 feet (deep) riprap key should be constructed into the bank. The barb should have a 10 feet width. From the crest, riprap should be sloped at a 1:1 slope for D50 riprap greater than or equal to a three feet diameter and 2:1 slope for D50 riprap less than a three feet diameter. Sizing of the riprap should be based on charts relating shear stress to sediment size from Hydraulic Engineering Circular No. 15 Design of Roadside Channels with Flexible Linings and Hydraulic Engineering Circular No. 11 – Use of Riprap for Bank Protection".*
>
> A compilation of WSDOT barb design criteria is presented in Table 1.

Upon investigation of literature (more than 100 documents) that is mainly related to unsubmerged or partially submerged spur dikes, groins, and other barb-like structures, it is found that the WSDOT design produces the most desirable flow redistribution and sediment movement for the riverine ecosystems, as well as, for bank and bridge protection. A sketch of the WSDOT design is shown in figure 4.

The following section describes the WSDOT barb geometric characteristics, namely, orientation, length, width and height/crest angle.

Orientation: The flow deflection produced by the barb was shown to reach a maximum at an upstream angle of 60 degrees (Francis et. al. 1968; FHWA 1984). However, an angle of 45 degrees with the upstream flow was "judged to be the best design to minimize the potential for bank erosion, while maximizing the volume of the scour hole and the potential benefits to the aquatic habitat" (Kuhnle et. al. 1998). A barb angle of 50 degrees is a compromise between a maximum protected zone and potential environmental benefits.

Length: A maximum protruding length of 1/4 to 1/3 the channel width creates a sufficient downstream protected region while minimizing future barb maintenance and environmental impact. As the length is increased, the protected region also increases (Lu and Xu 1989). However, the scour depth at the spur tip increases, the magnitude of flow at the tip increases, and the flow is deflected farther into the main stream (FHWA 1984). It is possible that these flow conditions could affect the stability and habitat along the

opposite bank, as well as affect the stability of the barb structure itself. Based on Alvarez (1989) and projects with similar structures on the Rio Grande River (Klump and Baird 1991), a length of ¼ to 1/3 the channel width is optimal.

Height/crest angle: The sloping crest of the WSDOT design has been shown to effectively allow different amounts of flow constriction and to accommodate changes in meander trace with stage. In addition, the slope crest allows submergence at higher flows, which helps minimize the impacts of local scour at the nose or tip (FHWA 1984). Also, the sloped crest has not been shown to reduce the protected region downstream the structure (Uijttewaal et al. 2001; Francis et al. 1968).

Width: The 10 feet of width and side slopes of the barb are primarily for stability. No harmful environmental side effects of these details were found in the literature.

Finally, empirical relations were proposed by the WSDOT in their manual to determine the stability of the rocks that formed a barb. In this study, the available design methodologies for riprap and stone were considered to provide a fundamental evaluation of the stability criteria. For the scaling process, a prototype riprap D_{50} = 2.5 feet was decided upon.

Table 1. WSDOT Barb Dimensions.

Prototype – from the North Fork of the Toutle River							
Dimensions							
Barb tip:							
height	1.5	ft					
width	10	ft	*plus rock sloped to the bed				
15 feet towards bank:							
length	15	ft	*WSDOT always sets 10 to 1 ratio for a 15 ft barb length				
height	3	ft					
slope	10	to	1				
width	10	ft	*plus rock sloped to the bed				
The rest of the barb to the bank:							
length	9.667	ft					
height							
slope	4%	to	1%				
width	10	ft	*plus rock sloped to the bed				
The length of barb z:							
z = 15' plus rest of distance							
z	24.667	ft					
Angle of barb with							

upstream bank:							
	50	degrees					

Scaling of flow, bed sediment and riprap

Scaling of a hydraulic model is a rather cumbersome process involving an assessment of the mechanically governing parameters for the given experimental study, the laboratory limitations, and the necessary hydraulic controls. **FLOW** are scaled using similarity relationships

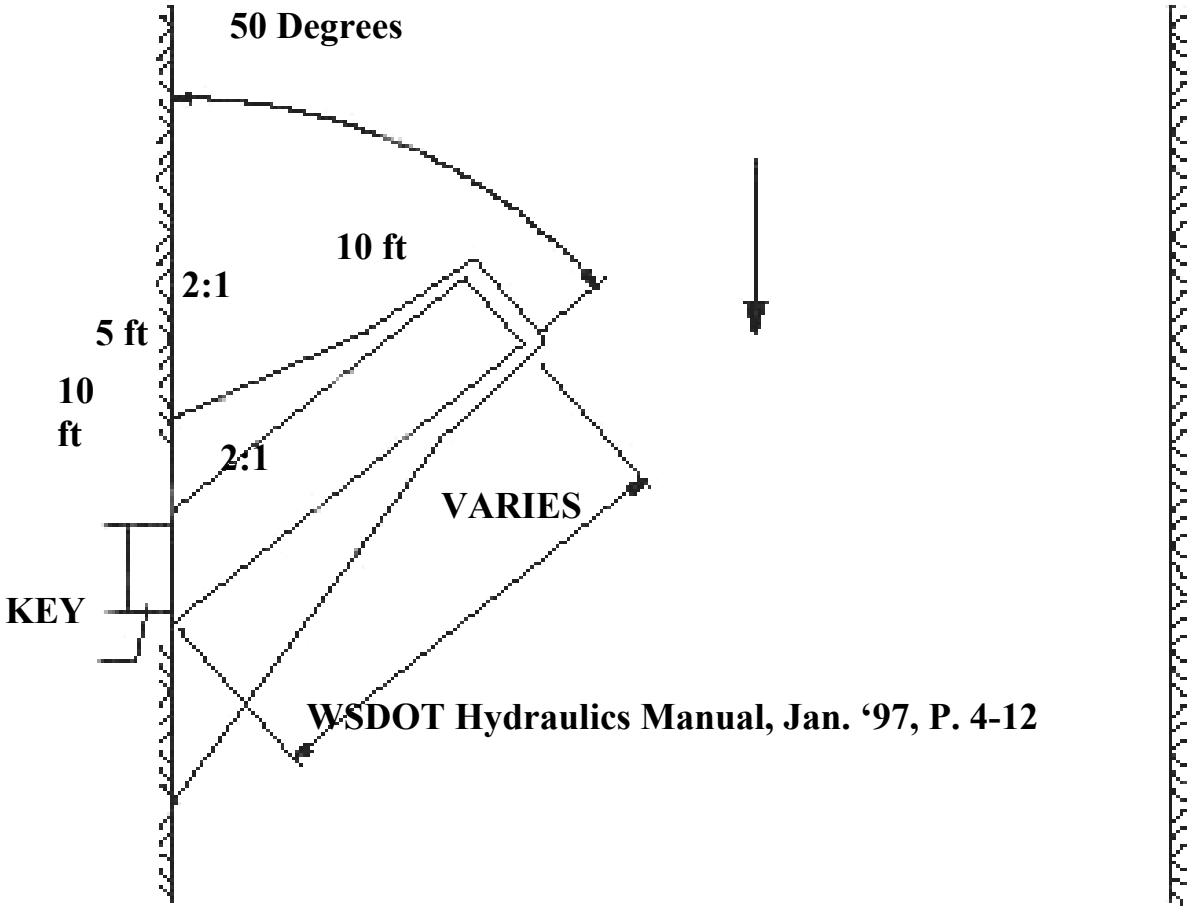

Figure 4. Schematic of Prototype Barb Configuration

including: the Reynolds number, a ratio of inertial to viscous forces, the Froude number, a ratio of inertial to gravitational forces, and geometry. Based on the research objective, a model is designed to study the effects of a few dominant forces by utilizing one or more of these relationships (Hwang and Houghtalen 1996). When the study comprises a rough bed or walls with moving sediment, the modeling methodology must be expanded to include sediment transport and/or roughness similitude under mobile or fixed bed conditions. Parameters taking these relations into account are the particle Shield's stress, a parameter of incipient motion, the particle Reynolds number, the Manning's roughness coefficient, and sediment discharge as related to hydraulic discharge (Maxwell 2000;

Przedwojski et al. 1995). It is impractical to provide similarity between all hydraulic and sediment parameters, as this would lead to the trivial solution of the full-scale model or prototype (Przedwojski et al. 1995). Therefore, it is the task of the modeler to maintain similitude between the hydraulic and/or sediment parameters which justly satisfy the given objective.

Complicating matters is the availability of space, maximum channel dimensions, and pump capacity within the laboratory. These factors must be included early within the modeling process to ensure feasibility of the experiments (Przedwojski et al. 1995). Finally, hydraulic controls must be included to ensure the model accurately depicts its prototype and avoid disturbances, such as gate effects or unwarranted secondary currents. Often, a methodical trial and error scaling process is necessary until all specific objectives and limitations are satisfactorily addressed. Next scaling is performed for the flow, sediment and riprap.

Flow and Fixed bed Roughness scaling

*Th*is scaling is useful when the flow tests around the vicinity of a barb are performed. Table 2 includes the stream flow and sediment characteristics for the prototype and the model. The "prototype" column in table 2 includes the original channel, flow and sediment data.

Following the laws of similitude the following scaling ratios were obtained (see Table 2 for input variables):

$$X_r = \frac{X_p}{X_m} = 9.25$$, where X is the longitudinal direction

$$Y_r = \frac{Y_p}{Y_m} = 7.12$$, where Y is the transverse direction

$$\frac{X_r}{Y_r} = 1.3$$ (Distortion)

$$Flow_r = \frac{Flow_p}{Flow_m} = 175.57$$

$$V_r = \frac{V_p}{V_m} = 2.67$$, where V is the velocity

$$S_r = \frac{S_p}{S_m} = 0.77$$, where S is the slope

$$Fr_r = \frac{Fr_p}{Fr_m} = 1.0$$, where Fr is the Froude number

The scaling of the fixed bed roughness is determined using the similitude of the Manning's roughness coefficient for the model was obtained using,

$$n_r = \frac{Y_r^{2/3}}{X_r^{1/2}}$$

where, n_r is the Manning's coefficient ratio, Y_r is the vertical geometry ratio, and X_r is the horizontal geometric ratio.

$n_r = \frac{n_p}{n_m} = 1.39$, where n is the Manning's roughness coefficient (dictated from the distortion number)

STREAM CHARACTERISTICS	PROTOTYPE	MODEL
Channel Geometry		
Channel Slope	0.00377	0.00450
Bank Slope	1:1	N/A
Channel Width (m)	22.50	1.22
Channel Depth (m)	1.07	0.15
Roughness Coefficient (n)	0.0265	0.0191
Flow		
Discharge (m^3/s)	57.40	0.16
Velocity (m/s)	2.29	0.90
Sediment		
Median Particle Size (mm)	28	4
Specific Gravity	2.65	2.65

Table 2 Input Parameters for Prototype and Model

Mobile sediment scaling

The mobile sediment scaling is necessary when the scour tests are performed. Experimental modeling of mobile-beds must satisfy similitude criteria characterizing sediment movement by stream flow and the interactive nature between flow and the deformable nature of particulate boundaries (ASCE, 2000). As such, dimensional analysis is not only strongly governed by gravity, but also must take into account submerged particle weight, interparticle friction, and the hydrodynamic forces exerted on particles. For sediment modeling similitude is based on the dimensionless bed shear stress (Przedwojski et al., 1995),

$$\tau^*_p = \tau^*_m \tag{5}$$

and expressed as the Shield's parameter,

$$\tau^* = \frac{\tau_0}{(\gamma_s - \gamma)d_{50}} \tag{6}$$

where, $\tau_0 = \gamma RS$ is the bed shear stress, γ_s and γ are the specific weight of sediment and water, respectively, R is the hydraulic radius, S is the slope, and other variables are as previously defined.

Two other important parameters utilized in mobile bed modeling are the relative roughness and relative submerged particle weight of the sediment. These terms are represented by the following equations:

$$\frac{R}{d_m} \tag{7}$$

$$(\gamma_s - \gamma)_p = (\gamma_s - \gamma)_m \tag{8}$$

where, d_m is the characteristic grain size of sediment usually taken as the mean sediment size, and other variables are as previously defined.

The bed roughness was scaled using the dimensionless Darcy friction factor (f). Due to dimensionless homogeneity this factor was adopted in lieu of the Manning's roughness coefficient. The equation for the Darcy friction factor is as follows:

$$f = \frac{8gRS}{V^2} \tag{9}$$

Due to distortion, similitude of the friction factor was not attainable. Following the criteria set forth by Yalin 1971 (Ch 4 River Models), for straight reaches with rough boundaries and uniform flow, skin friction is only considered and the equation for f becomes:

$$f = \frac{1}{\delta} \tag{10}$$

where, δ is the distortion factor equivalent to X_r/Y_r. Under these assumptions the Reynold's particle mobility number, Re_*, must also be taken into consideration. For these assumption to hold true, the particle Reynold's number must be greater than 70 (Yalin, 1971), where,

$$Re_* = \frac{u_* d_m}{\nu} \tag{11}$$

and u_* is the friction velocity, ν is the kinematic viscosity, and other variables are as previously defined.

Manipulation of these governing equations resulted in a mean particle size of 5.2 mm. As a check a comparison was made using the Manning's coefficient and the flow scaling process and a median particle size of 5.1 mm was determined.

Barb Model

The model barb was scaled following geometric similitude; where both the prototype and model are identical in shape but differ in size. The horizontal and vertical scaling ratios were based on Froude similarity. Table 3 outlines the dimensions of each.

BARB CHARACTERISTICS	PROTOTYPE	MODEL
Barb Tip		
Height (m)	0.45	0.06
Crest Width (m)	3.05	0.34
Slope	2:1	2:1
Main Body Section		
Height (m)	0.91	0.12
Crest Width (m)	3.05	0.34
Length (m)	4.57	0.49
Slope	10:1	10:1
Transition Section to Bank		
Height (m)	Varies	N/A
Crest Width (m)	3.05	0.34
Length (m)	2.96	0.30
Slope (m)	4:1 to 5:1	4:1 to 5:1

Table 3. Comparisons of Prototype and Model Stream Parameters

Riprap Model

Riprap is the most adopted means commonly used in countermeasures for the protection of erodible channel boundaries (Maynord et al., 1989; Escarameia, 1998; Melville and Coleman, 2000). There are many contributing factors for riprap stability, such as, gradation, shape, stone density, thickness including filter layer, channel side slope, channel bend, angle of repose, angle of flow impingement to the bank, and adequate embedment of toe (Maynord et al., 1989; Escarameia, 1998; Cotton, 1998; Melville and Coleman, 2000). Improper design of riprap parameters can lead to several modes of failures including particle erosion, translation slide, modified slump, and slump failure (HIRE, 1990). The most common failure, particle erosion, occurs when particles are dislodged due to hydrodynamic forces of flow. Translation slide failures typically occur due to undermining of base material resulting in the downward slope movement of rock mass. Modified slump failure or winnowing, much like translation slide failure, is generated when the mass of rock movement occurs due to internal slip surfaces. Lastly, slump failure occurs due to shear failure of the underlying base material, which can result in the riprap material becoming embedded beneath the sediment bed. As detailed in Highways in a River Environement (HIRE), Table 4 summarizes the typical modes and probable causes of riprap failure (FHWA, 1990).

Numerous equations exist for the determination of riprap sizing and are typically based on shear stress or velocity parameters. The major downfall to this type of approach resides in the accuracy of obtaining the measurements and the determination of where to take the measurements. As stated by Cotton (1998), the boundary shear stress distribution is difficult to estimate in non-symmetrical cross-sections, particularly where there is a complex interaction between the floodplain and main channel (e.g., river bends). This statement holds true with respect to velocity measurements as well.

Coupled with measurement accuracy, empirical equations are typically based on one-dimensional flow analyzed in rectangular flumes, i.e., simple channel geometry that does not account for the presence of a floodplain. A natural river environment encompasses a combination of flow conditions and channel configurations. For these reasons, riprap-sizing equations may contain the inclusion of an empirical coefficient(s) or a factor of safety.

Another contention of concern is the role that turbulence plays on riprap stability. Flow in rivers and channels are predominately turbulent in nature. As stated by Escarameia (1998), out of the numerous stability equations available, almost all for the design of riprap, only three incorporate parameters that account for the turbulent nature of flow. These equations are Escarameia and May (1992); Pilarczyk (1990); and Maynord (1993) – US Army Corps of Engineers' Design Procedure.

Table 5 outlines various equations that were used to determine an appropriate riprap size for this case study. As one can see, a designer must choose between numerous valid equations that produce extreme variations of results. Due to the nature of this variability it was determined to use a prototype mean diameter of 0.37 m, which scaled to a mean diameter of approximately 63.5 mm for the model barb. This was based on engineering judgment and averaging the most reasonable calculated values. The mean diameter of 0.37 m was also close to the WSDOT prediction.

The stability of a structure is increased with well-graded angular riprap mixtures, increased riprap thickness, the addition of filter material between the riprap structure and the channel bottom, and embedded riprap (FHWA, 1990). As such, adequate replication of the shape and roughness of riprap material were the most critical parameters analyzed; with sizing being a secondary concern. In this research size gradation of the riprap material was relatively uniform, thus utilizing a more conservative approach for embedment depth. Increased riprap thickness and filters for riprap were not included in the scope of this study.

Mode of Failure	Probably Cause of Failure
Particle Erosion	Stone size to small Removal of stones due to impact or abrasion Side slope angle larger than angle of repose Uniform gradation of riprap
Translation Slide	Steep side slope Excess pore pressure Loss of toe foundation due to erosion
Modified Slump	Side slope angle close to angle of repose resulting in imbalance or movement of individual stones Settlement of submerged riprap, impact, abrasion, particle erosion, or some other cause resulting in dislodge of upslope riprap
Slump	Impermeable layers of nonhomgeneous base material resulting in fault line when excess pore pressure present Side slope angle large enough that gravitational forces exceed inertial forces of riprap and base material

Table 4. Modes of Riprap Failure (after FHWA, 1990)

Method	D_{50} (m)	Comments
Federal Highway Administration, (HEC-11) 2000	2.01	Based on shear stress Equation for an abutment; does not account for backwater effects
Abt et al. 1998	0.30 0.91	Based on unit discharge; applicable for small range of flows; Accounts for flow bwtween layers using moderate hazard condition
Washington State Department of Trans.1997	0.34	Based on shear stress, channel slope, and normal depth Shear stress charts - Hydraulic Engineering Circular No. 15 & No. 11
US Army Corps of Engineers 1994	1.87	**D_{30} diameter Based on thickness coefficient factor; defines stability of large range of gradations if placed to a thickness of D_{100}(max)
Kilgore & Young 1993	0.08	Based on shear stress and Froude number
Abt & Johnson 1991	0.37 0.39	Based on bank overtopping flow; empirical curves; 1%, 2% & 8% embankment slope; 4 failure tests Safety factor of 1.2 used
Escarameia & May 1992	0.61	Based on turbulent intensities and near bed velocity measurements at 10% of the water depth
Highways In A River Environment 1990	0.07 0.24	Based on displacement due to velocity impingement Safety factor of 2.0 used
Pilarczyk 1990	2.78 1.67	Based on empirical coefficients derived from prototype trials Turbulence factor of 1.5 used (high river turbulence) Turbulence factor of 1.0 used (normal river turbulence)
Wang & Shen 1985	0.12	Based on shear stress
Gessler 1971	0.49	Based on local boundary shear and Shields parameter of 0.049; incipient motion of one particle on a flat bed
Bureau of Reclamation 1974	1.52	Based on using velocity downstream of hydraulic structure and field observations
Federal Highway Administration, 1956	0.20	Plane sloping bed; safety factor less than 1.0 using Simons and Senturk (1992)

Table 5. Summary of values obtained for D_{50} using various riprap sizing equations

Experimental Set-up

The flume experiments are conducted in the Albrook Hydraulic Laboratory located at Washington State University. The water-recirculating flume, which is constructed by the first author, is 10.4 m long, 1.2 m wide, and 1.2 m deep. The flume frame is constructed of wood panels for the walls and floor, made of 0.6 m x 1.2 m and 0.09 m thickness plywood. A PVC membrane (PVC liner with 30 mm thickness) is placed within the wood framed flume to waterproof the structure.

The upstream end of the flume is attached to a headbox connecting the pipe supply system to the flume. The headbox of the flume is equipped with a honeycomb structure to provide rectilinear flow. The downstream end of the flume is attached to an outlet cage mounted on the return pipe. The floor of the flume is covered with aggregate composite panels to form an artificial immobile roughness. The aggregate panels are made from natural worn gravel with a median diameter of 5.2 mm. More information on the construction of the model is provided by Fox (2002) and Kjos (2003).

Water distribution through the 0.51 m diameter supply pipe is facilitated by means of a 100 HP single-stage propeller pump that carries water from a recirculating sump with 95 m^3 useful volume. The discharge is measured via a water/air U-tube manometer. Tail water is controlled by the use of different combinations of rods placed at the free-fall exit of the flume. Rulers pre-placed along the length of the flume wall are used to determine flow uniformity for each condition.

The test section, where the barb structure is placed, is located 6.8 m downstream of the headbox to ensure that fully-developed flow conditions are present during the experiments. Figure 2 on page 5 illustrates the barb in the experimental flume used during the test. The model barb is constructed of aggregate concrete poured in a prefabricated geometric mold with dimensions derived from scaling procedures.

To ensure that the incoming flow is two-dimensional during testing, the ratio of the top width to the average flow depth, B/h, is greater than 5 (Song et al. 1994). The ratio of the average flow depth to the bed roughness, h/d_{50}, is greater than 3, so that no surface effects are pronounced during the tests (Bettess 1984). The wall effects are determined to be minimal at a distance of 10 cm from the flume walls (Vanoni and Brooks 1957).

Table 6 summarizes the flow conditions during the tests. S is the gradient of the flume bed, B is the internal width of the flume, h denotes the normal-depth of the flow, Q is the volumetric discharge obtained from the manometer, $U_{bulk} = Q/A$ is the mean bulk fluid velocity where A is the cross-sectional flow area, the Reynolds number, $Re = U_{bulk} h / \nu$ and the Froude number, $Fr = U_{bulk} / \sqrt{gh}$, the median diameter d_{50}, the specific gravity, *S.G.*, the width to the average flow depth ratio (i.e. aspect ratio), B/h, and the ratio of the average flow depth to the bed roughness, h/d_{50}.

Experimental Design

As part of the experimental design of this investigation, the following tasks are

undertaken: (1) performance of pilot visualization tests to identify the main flow regions around the partially submerged barb; (2) performance of detailed turbulence flow measurements to complement the

Table 6. Flow conditions during barb testing.

S	*B*	*h*	*Q*	*Ubulk*	*Re*	*Fr*	d_{50}	*s.g.*	*B/h*	h/d_{50}
m/m	m	m	m3/s	m/s	-	-	mm	-	-	-
0.0045	1.22	0.152	0.162	0.87	130,000	0.59	5.2	2.65	8.0	29.2

visualization tests and determine the time-averaged flow characteristics and mean turbulent statistics around the barbs; and (3) identification of a selected number of measuring locations, representative of flow regions, which are later utilized within the eddy classification methodology.

Dye visualization tests are performed to qualitatively describe the flow patterns around the barb and investigate the effects of permeability on the flow characteristics around a barb. The dye setup consists of dye containers, dye needles, tubing connecting the two, lighting, and a digital video camera. The dye containers are placed on platforms constructed above the flume to allow pressure dye flow. Three dye needles are fixed to the downstream edge of the barb, one close to the barb tip, one close to the flume wall, and one in between. A halogen lamp is placed above the setup to allow proper illumination of the test section and facilitate recordings of the flow patterns around the barb via the video camera. Figure 2 illustrates the flow regions that are developed around the barb. Three distinct regions are visually distinguished, namely, the main core, the shear layer, and the stagnant wake. The main core flow extends from the tip of the barb to the main channel flow and occurs within the channel longitudinal direction. The wake region regime, a stagnant flow region, is found to form behind the structure and along the downstream near sidewall. The shear layer region is formed between the stagnant wake region and the accelerating main core flow, and is indicative of an overtopping-accelerating regime.

The three flow regimes are present in both rock (permeable) and concrete (impermeable) barb. Figures 5 and 6 illustrate the flow in the vicinity of the barbs. It is found that the concrete barb causes higher backwater water effects by increasing the water depth by almost 15-20% comparatively to the rock barb. The rock barb being permeable allows flow to transport (known as percolating flow) through its structure. The same time it is found that flow accelerates at a higher degree downstream the concrete barb comparatively to the rock. The separation flow is greater for the concrete barb due to the decreased roughness and increased convective streamwise acceleration.

Once the main flow regimes are identified, a testing grid is established to facilitate detailed measurements of turbulence and map the velocity patterns formed within the vicinity of the barb. For this purpose, a SonTek Acoustic Doppler Velocimeter (ADV 10 MHz) with sampling rate 0.1-25 Hz, velocity resolution of 0.01 cm/s and accuracy 1% of measured velocity is employed. An important advantage of the ADV is that it measures the flow in a small sampling volume (approximately 0.25 cm^3) that is 5 cm away from the transmitting transducer. This enables the collection of turbulence measurements without interfering with the flow. During sampling, the ADV is mounted on a rigid beam

placed well above the water surface to avoid flow-induced vibrations, as such vibrations may cause elevated intensity readings (Dancey 1990).

Detailed flow measurements around the barb are obtained over a fixed Cartesian grid system.

Figure 5. Flow around the concrete barb

The grid system is expressed by the following convention: x=0 cm is the upstream test section extent for the streamwise direction; y=0 cm corresponds to the barb-wall boundary and denotes the transverse direction; and z=0 cm corresponds to the flume bed and denotes the vertical direction. Within the established *x, y, z* grid system, 768 total measuring points are administered—256 points at the (*x*-*y*) plane are mapped at three vertical levels, that is, at *z=0.2h, z=0.4h,* and *z=0.7h* from the fixed bed. Measurements at the (*x*-*y*) plane are obtained every 10 cm in the *x*-direction and every 5 cm in the *y*-direction. For each measuring point, 3,000 samples of the instantaneous velocity vector are measured with the ADV to produce a quasi-continuous time-series.

The postprocessing and analysis of velocity data is performed using the *WinADV32 Version 1.843* software developed by the U.S. Bureau of Reclamation. *WinADV* computes mean (time-averaged) velocities (*U, V,* and *W*; where *U* corresponds to the streamwise direction *x*, *V* corresponds to the transverse direction *y*, and *W* corresponds to the vertical direction *z*), standard deviations of velocities or turbulent intensities ($\sqrt{\overline{u^2}}, \sqrt{\overline{v^2}}, \sqrt{\overline{w^2}}$), and covariance velocities ($\overline{uv}, \overline{uw}, \overline{vw}$).

The data obtained for the 768 measuring points of the Cartesian grid system are filtered to remove "bad" measurements or measurements with poor correlations (Fox 2002). Bad measurements are obtained mainly near the free surface (at $z = 0.7\ h$) due to water surface fluctuations caused by the barb obstacle. One of three problems generally result at this depth, including: surface waves may cause the exposure of the tip of the ADV probe to air; aliasing of the velocity data due to acoustic reflections of the bottom of the flume or the structure of the barb

Figure 6. Flow in the vicinity of the rock barb

biases the average velocities and makes instantaneous velocity measurements uncertain; and measurements contain correlations less than 70%, and are deemed poor, due to inadequate signal strength and excessive air bubbles (Nielsen et al. 1997).

Upon completing the removal of erroneous measurements from the dataset, a detailed mapping of the velocity vectors along the (x-y) plane via the computer graphic package *Tecplot 8.0* is obtained. Figure 7 details the distinct flow patterns around the barb at $z = 0.2\ h$, $z = 0.4\ h$, and $z = 0.7\ h$ and supports the findings of the visualization tests. For all depths, the stagnant wake region is depicted as a slow moving "dead zone" with wake flow stagnation to be pronounced at $z = 0.7\ h$. The middle regime, the shear layer region, reveals a transitional energy dissipation zone. Thus, a direct correlation can be seen between the qualitative and quantitative test data.

The last course of the experimental design entails the identification of a select number of measuring locations for performing detailed eddy analysis. Five measurement locations are chosen based on the qualitative and time–averaged flow measurements and the geometric characteristics of the barb. Three of the chosen points correspond to the main core flow region, the stagnant region, and the shear layer region. The remaining two points correspond to the nose of the barb and to the backwater region upstream of the

barb. Figure 8 illustrates the five locations, A17, K13, N20, P17, and P7, around the partially submerged barb chosen for the in-depth eddy analysis. Table 6 compiles mean velocity and turbulent intensity information for the locations chosen.

Conclusions for objective 1

1. Scaling is performed for fixed and mobile roughness. The Manning's criterion is appropriate for the scaling of the fixed roughness and the Shields criterion for the mobile roughness.
2. Rock barbs behave overall better hydraulically than the concrete barbs and cause less backwater effects. Therefore, the concrete barb will not be examined further for detailed flow and scour analysis.
3. Three flow regimes form around a partially submerged barb: 1. main flow region, shear layer region and the wake flow region.

a)

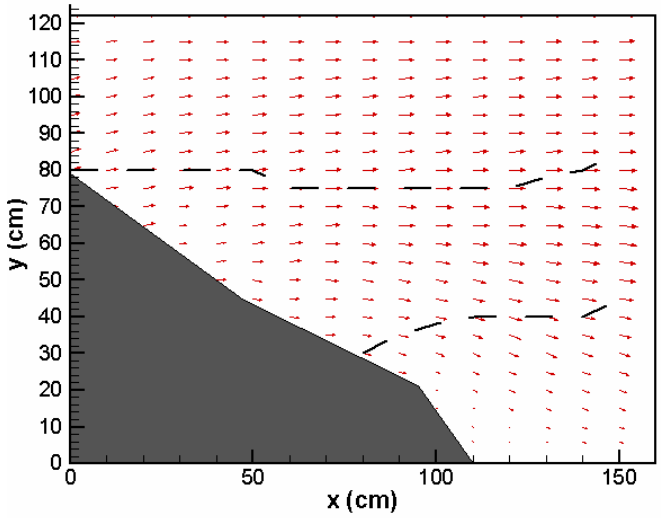

b)

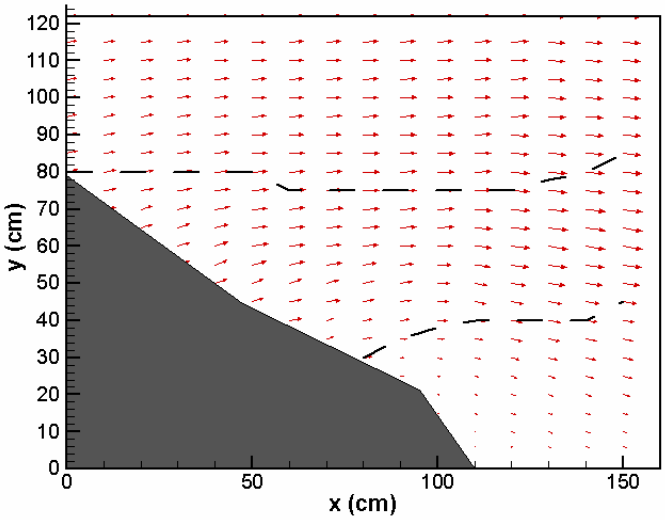

c)

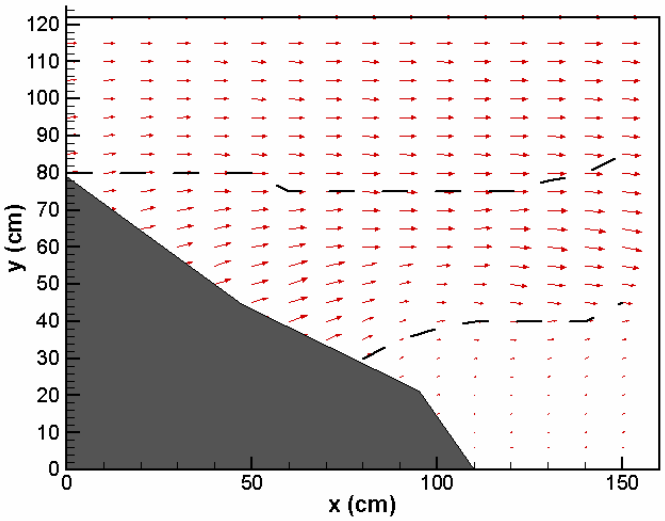

Figure 7. The velocity vector around the barb

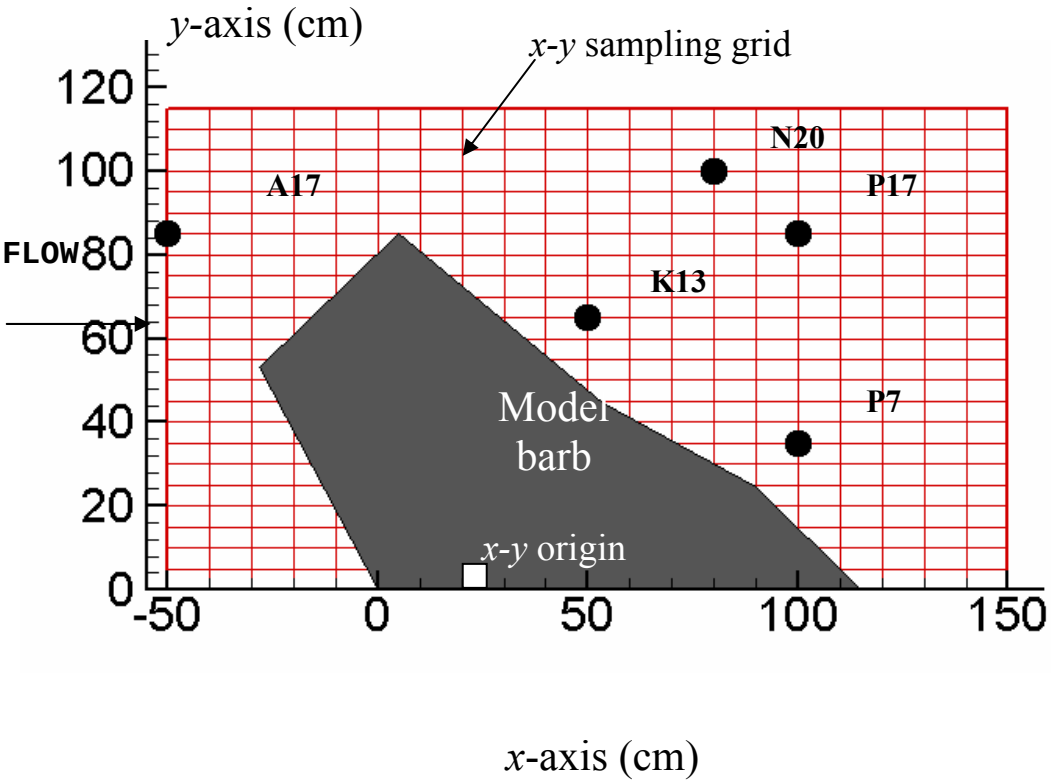

Figure 8. The five locations where detailed measurements were obtained

Objective 2. Analysis of the time-averaged flow parameters, Reynolds stresses, and other turbulence parameters in the immediate downstream vicinity of the model barb

The objective of this task is twofold and includes the following: (1) the presentation of an eddy classification methodology, which couples an innovative statistical technique with traditional procedures to isolate small- and large-scale eddies and discern their properties; and (2) application of the eddy classification methodology to quantitatively describe the frequency and size of eddies produced by the presence of the model barb structure. It is expected that the methods and results contained within this paper will be utilized and built upon to further turbulence research in environmental settings.

Determination of the size of eddies formed around a barb is of paramount importance for evaluating the aquatic health of a stream. It is well documented in the literature that eddy size relates directly to the fork length of fish species. The distribution of eddies around a barb will affect also the size of the scour hole.

The present methodology is based on the consideration that fast-frequency velocity fluctuations correspond to small-scale eddies, while slow-frequency velocity fluctuations correspond to large-scale eddies (e.g. Dargahi 1997; Buffin-Belanger and Roy 1998; Tamburrino and Gulliver 1999; Shvidchenko and Pender 2001). Determination of the fast and slow frequency velocity fluctuations is quantitatively described by utilizing the triple decomposition theorem introduced by Hussain and Reynolds (1972). According to this theory an instantaneous velocity signal at a fixed geometric location can be decomposed into a mean velocity component and two fluctuating velocity components representing larger and smaller eddy-structures, respectively. The decomposition of the 3-D velocity measurements at a fixed location is expressed as follows:

$$u(t) = U + u'(t) + u''(t) \qquad (12)$$

$$v(t) = V + v'(t) + v''(t) \qquad (13)$$

$$w(t) = W + w'(t) + w''(t) \qquad (14)$$

where u, v, w are the instantaneous velocity measurements, *U, V, W* are the temporal mean velocities, u', v', w' are the slow fluctuating component of the instantaneous velocities, and u'', v'', w'' are the fast fluctuating component of the instantaneous velocities.

For eddy analyses, the slow fluctuating components are isolated using the moving average over a time step T_s (Muller 1982; Tamburrino and Gulliver 1999), as follows:

$$u'(t) = \frac{1}{T_s}\int_{t-\frac{T_s}{2}}^{t+\frac{T_s}{2}} [u(t')dt] - U \qquad (15)$$

The slow fluctuations are then plotted and analyzed. In addition, the fast fluctuations are isolated by:

$$u''(t) = u(t) - [u'(t) + U] \qquad (16)$$

Table 2. Mean velocities and turbulence intensities for eddy analysis locations.

Sampling Location		Depth	Mean Velocities			Turbulent Intensities		
Location	*z=*	*H*	*U*	*V*	*W*	*rms u'*	*rms v'*	*rms w'*
		cm	cm/s	cm/s	cm/s	cm/s	cm/s	cm/s
A17	**0.2*h***	22.1	52.5	1.9	0.0	7.4	5.5	3.5
A17	**0.4*h***	22.1	56.7	6.8	-0.4	7.3	7.6	3.8
A17	**0.7*h***	22.1	67.2	3.6	-0.2	7.0	5.4	4.0
N20	**0.2*h***	16.1	121.7	2.4	-7.6	8.8	8.0	3.1
N20	**0.4*h***	16.1	132.6	6.3	-5.9	5.4	4.1	5.0
N20	**0.7*h***	16.1	136.7	7.9	-0.3	5.1	5.3	4.0
P17	**0.2*h***	15.2	126.0	-1.6	-8.1	12.9	8.6	4.3
P17	**0.4*h***	15.2	143.5	-6.8	-10.6	6.9	4.3	5.2
P17	**0.7*h***	15.2	158.3	-16.4	-12.5	5.2	5.1	3.9
K13	**0.2*h***	15.8	120.9	5.7	-7.8	13.4	11.7	8.4
K13	**0.4*h***	15.8	138.3	2.7	-3.2	9.3	6.0	8.4
K13	**0.7*h***	15.8	144.3	1.1	-4.2	5.8	5.7	4.4
P7	**0.2*h***	15.2	39.7	7.8	0.4	60.9	53.2	12.4
P7	**0.4*h***	15.2	78.8	-24.4	1.3	32.3	16.2	29.6
P7	**0.7*h***	15.2	103.5	-71.5	19.5	28.2	35.2	15.5

Table 7 clearly indicates that the level of turbulence is the highest at location P7 where eddies shed from the barb surface, wake eddies, and eddies associated with the Kelvin-Helmotz instability are present. This is evident in the "turbulent intensities" column.

Conclusions for objective 2

The eddy analysis leads to the following conclusions:

1. Large eddies in the main-core flow region pass the barb with little alteration of their periodicity or dimensions.

2. The barb presence decreases spacing and reduces the longitudinal dimensions of the large-scale eddies passing over the structure due to acceleration and increased energy dissipation.
3. Sweeping small eddies persist upstream of the barb; ejection small eddies dominate in the main core region; and a number of small shedding and ejection eddies exist within the shear layer and wake regions including eddies shed from the barb surface, wake eddies, and eddies associated with the Kelvin-Helmotz instability.

Objective 3. Analyze Available Methods and Determine the Best Methods and Determine the Best Predictive Shear Stress Results for Varied Flow Regimes

Shear stress, a force per unit area, is a controlling mechanism in the erosion and deposition process of streambed sediment (Kim et al. 2000). Open-channel flow may be classified as uniform flow, gradually varied flow, and rapidly varied flow on the basis of its depth rate variation with respect to longitudinal distance variation (Chang, 1998). Currently, estimation of the bed shear stress around hydraulic structures is mainly based on the assumption that flow is uniform and steady. This can greatly attribute to miscalculations of localized scour depths. As such, an accurate method for computing bed shear stress is required.

The objective of the shear stress analysis was to examine and determine the most suitable method of estimating near-bed shear stress. In this study a sensitivity analysis was conducted to determine the appropriate method for calculating the bed shear stress. Four different methods were explored. Each method is described below. Assumptions and equations for each method are also listed.

An analysis was done utilizing four shear stress methods, Uniform Flow Method, 1-D Transitional Flow Method, Rapidly Varied Flow Method, and Reynold's Shear Stress Method. These methods were utilized along a longitudinal line in the fast moving main core flow where flow appears to be less affected by the structure. Data was analyzed at y = 100 (transverse direction) along the longitudinal at x = -50; 0; 50; 100; 150 (Figure 6.9). Shear stress was calculated using each method at 0.2 of the depth in order to compare ADV results taken at the same depth.

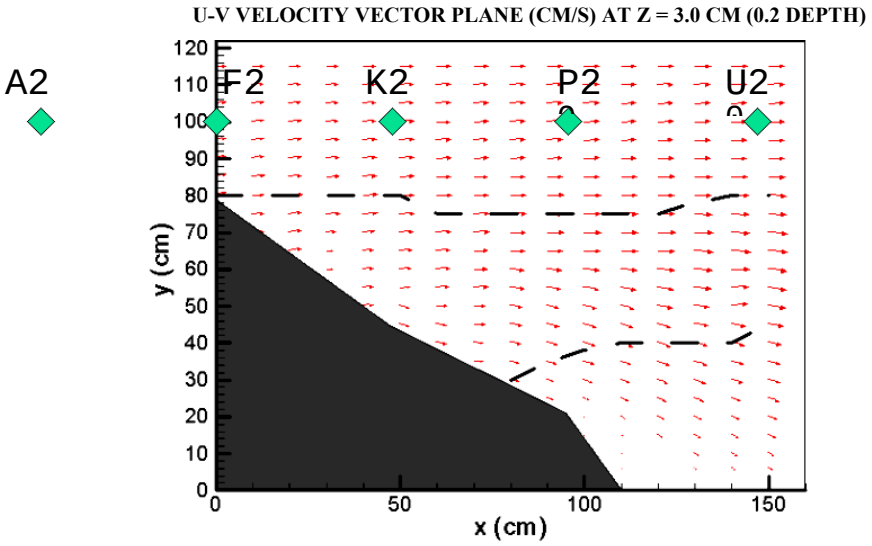

Figure 6.9 Diagram Depicting Points Analyzed in Shear Stress Analysis

Uniform Flow Method (UFM)

Under uniform flow conditions physical properties such as velocity, depth, and roughness stay constant along the flow direction (Chang, 1998). Although the natural river environment can rarely be considered uniform flow, uniform flow equations are still used assuming an equivalent energy loss is experienced between a gradually varied flow and uniform flow section. Under this assumption uniform flow relationships may be implored to evaluate the energy gradient in a gradually varied flow section. Governed by these assumptions and conditions of hydrostatic pressure, it is easily discernible that the bottom channel slope, S_0, and the surface slope or EGL slope, S_f, are equivalent in a one-dimensional (1-D) steady uniform flow field (Figure 6.10). Thus the bottom shear stress can be calculated from the following equation:

$$\tau_{UFM} = \rho g H S_0 \qquad (17)$$

where, τ_{UFM} is the bottom shear stress, ρ is the density of water, H is the flow depth, and S_0 is the channel bottom slope.

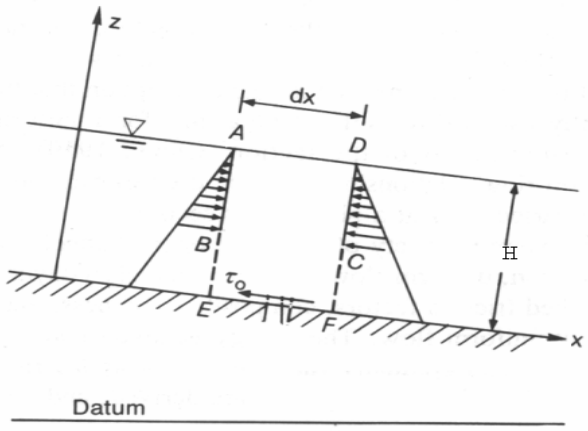

Figure 6.10 Schematic of Uniform Flow Variables (after Chang, 1998)

1-D Transitional Flow Method (TFM)

The premise behind this method entails the concept of gradually varied flow. Gradually varied flow is described as flow where the rate of variation of depth with respect to distance is small, or significant depth changes occur gradually over a long distance (Chaudhry, 1993). Characteristically the channel bottom of a gradually varied flow regime is generally mildly sloped, less than 5%. Long straight channels infer parallel streamlines and thus the pressure distribution can be assumed hydrostatic. Over a long distance frictional losses cannot be ignored. Under these assumptions of steady uniform flow, head losses associated with gradually varied flow can be determined using the following equation:

$$\frac{dy}{dx} = \frac{\left(S_0 - S_f\right)}{\left[\frac{1-\left(\alpha B Q^2\right)}{gA^3}\right]} \tag{18}$$

Noting that $(\alpha BQ^2)/(gA^3) = (Q/A)^2/(gA/\alpha B)$; the Froude number, $Fr = V/(gH)^{1/2}$, and assuming that α is unity, Equation 6-2 becomes

$$\frac{dy}{dx} = \left[\frac{\left(S_0 - S_f\right)}{\left(1 - Fr^2\right)}\right] \tag{19}$$

OR

$$S_f = \left[\left(\frac{-dy}{dx}\right)\left(1 - Fr^2\right)\right] + S_0 \tag{20}$$

The bottom shear stress can be calculated from the following equation:

$$\tau_{TFM} = \rho g H S_f \tag{21}$$

where, τ_{TFM} is the bottom shear stress, S_f is the slope of the energy grad line, and other variable are as previously defined.

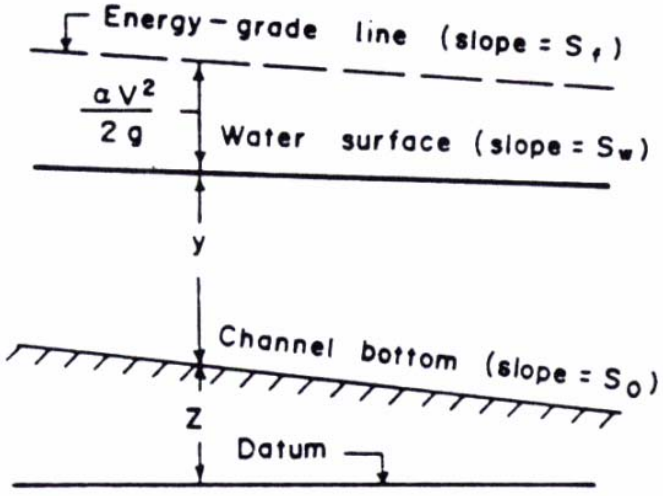

Figure 6.11 Schematic of 1-D Transitional Flow Variables (after Chaudry, 1993)

2-D Rapidly Varied Flow Method (RVFM)

Rapidly varied flow exists when the rate of variation of depth with respect to distance is large, or when significant depth changes occur gradually over a short distance (Chaudhry, 1993). Under rapidly varied flow conditions the calculation of the water surface slope is derived from the following equation

$$S_{fx} = \left[\frac{n^2 U \left(U^2 + V^2\right)^{1/2}}{\left(C_0{}^2 H^{1.33}\right)} \right] \tag{22}$$

where, S_{fx} is the friction slope in the x-direction, U and V are the depth-averaged flow velocities in the x and y-directions, respectively, and other variables are as previously defined. As shown in 6-6 the calculation of the water slope is a function of velocity components in the x and y directions. This equates to a 2-dimensional; unsteady flow; surface slope equation. An underlying assumption related to this equation implies that the pressure distribution at every point is hydrostatic; except in the area of a hydraulic jump or surge wave. As stated by Cunge (1975), details are lost in this area, but for engineering purposes the overall results are sufficient (Chaudhry, 1993). Another assumption inherent in this equation is that over short distances friction losses associated with boundary shear are negligible. The bottom shear stress can be calculated from the following equation:

$$\tau_{RVFM} = \rho g H S_{fx} \tag{23}$$

where, τ_{RVFM} is the bottom shear stress, and other variable are as previously defined.

Reynolds Shear Stress Method (RSSM)

The natural river environment is typically classified as turbulent flow (Roberson and Crowe, 1997). The premise of the three previous methods relied on the concept of parallel streamlines. In turbulent flow the streamlines are disrupted by eddies moving in all directions. Turbulent eddies are formed when fluids come in contact with a solid boundary or when two fluid layers moving at different speeds come in contact. The collision between two particles of different speed causes momentum to be exchanged between the particles, thus, producing eddy formation resulting in chaotic or turbulent flow. As such, the instantaneous velocity can be broken down into two components (Figure 6.12):

$$u = \bar{u} + u' \tag{24}$$

where, u is the instantaneous velocity, $\bar{u}$, to be denoted u (bar), is the time-averaged velocity component, and u' is the fluctuating velocity component (Kim et al., 2000). In turbulent flow environments the determination of channel bottom shear stresses is difficult, if not impossible, by direct means (Stapleton and Huntley, 1995). Instruments, such as an ADV have the capability of capturing the time-averaged and fluctuating velocity components simultaneously. Indirectly the Reynolds stress, or 'eddy correlation' method as stated by Soulsby (1983), can be obtained from the ADV output data. The Reynolds shear stress is defined by,

$$\tau_{Re} = -\rho\overline{u'w'} \tag{25}$$

where, τ_{Re} is the Reynolds shear stress, ρ is the density of water, u' and w' are the horizontal and vertical turbulent velocity fluctuations, and the overbar denotes averaging in time (Heathershaw and Simpson, 1978). Turbulent eddies are parameterized as causing a downward diffusion of momentum, thus defining the negative sign in the Reynolds shear stress equation. From Equation 6-9 it can be seen that the magnitude of stress is directly related to the magnitude of the instantaneous velocity fluctuations.

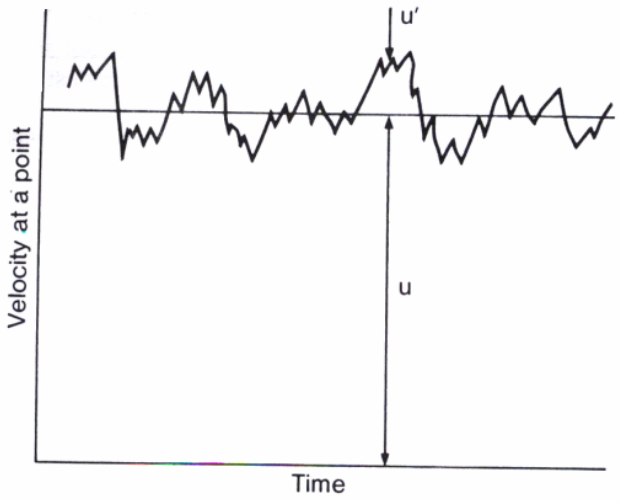

Figure 6.12 Schematic of Velocity Components for Reynolds Shear Stress Method (after Chang, 1998)

Results

Using the aforementioned methods the near bed shear stress (0.2 of the flow depth) was calculated at the five determined points (See Figure 6.9). Table 6.1 below summarizes these results.

BED SHEAR STRESS AT 0.2 DEPTH COMPARISONS						
RAW DATA			UFM	TFM	RVFM	RSSM
Point	x cm	y cm	At 0.2 H tau_{UFM} N/m^2	At 0.2 H tau_{TFM} N/m^2	At 0.2 H tau_{RVFM} N/m^2	At 0.2 H tau_{Re} N/m^2
A20	-50	100	7.86		1.62	0.93
F20	0	100	7.47	21.53	3.84	0.62
K20	50	100	6.02	102.22	7.70	9.56
P20	100	100	5.43	57.90	10.16	1.20
U20	150	100	4.93	56.97	12.40	2.18

Table 6.1 Summary of Calculated Bed Shear Stress Values

Looking at the data in Table 6.1 it is evident that the Rapidly Varied Flow Method RVFM correlates the best with the actual data used in the RSSM for points A20, F20, and K20 where hydraulic jump is not present and no significant surface waves exist. It is, also, shown that for points P20 and U20 where surface waves are present (no hydrostatic pressure exists) the UFM approximates closer the RSSM data. It was, therefore, concluded that the Rapidly Varied Flow Method provides the best available means for calculating near bed shear stress in turbulent flow when instantaneous velocity measurements are not available. Figures 6.13 and 6.14 show contour maps of the RSSM and RVFM, respectively. These plots provide a graphical comparison between the two methods for the entire test section.

Each plot shows trends between flow zones, and is further comparative with the flow mechanics found in the quantitative and qualitative flow analysis. The fast moving main core flow depicts low positive values of shear stress indicative of scour, while the stagnant wake region (slow moving flow) depicts negative or near zero values indicative of deposition or no scour. The shear layer region becomes blurred in the RVFM contour plot. At high flow, the barb is submerged and a hydraulic jump is seen just on the leeward side of the structure in the mid-section of this zone. Due to the inherent hydrostatic assumption associated with this equation, the method does not adequately capture the area within a hydraulic jump or surge. For this reason, the RVFM does not fully capture the shear stress changes in the shear zone region.

As a comparison/contrast, a contour map for the UFM is also included (Figure 6.15). Clearly the UFM does not capture the detail (or distinguish) between the three flow regions. This strongly confirms the need for a method of shear stress prediction (when real-time velocity data is unavailable) not based on uniform steady flow conditions.

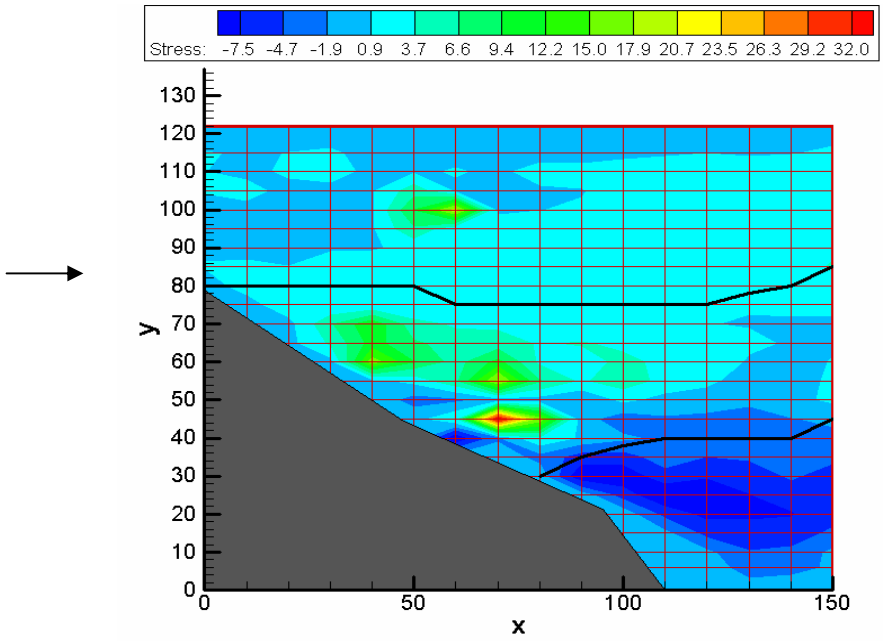

Figure 6.13 Contour Plot of Reynold's Shear Stress (N/m^2) in the X-Z Plane at Z= 3.0 cm (0.2 Depth)

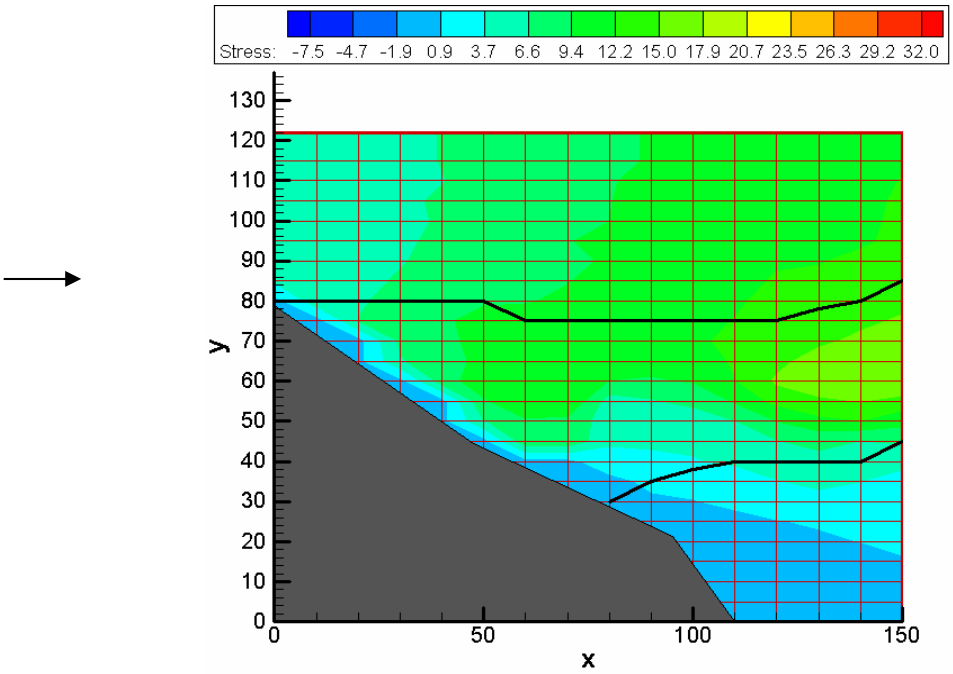

Figure 6.14 Contour Plot of Shear Stress (N/m^2) using RVFM at Z= 3.0 cm (0.2 Depth)

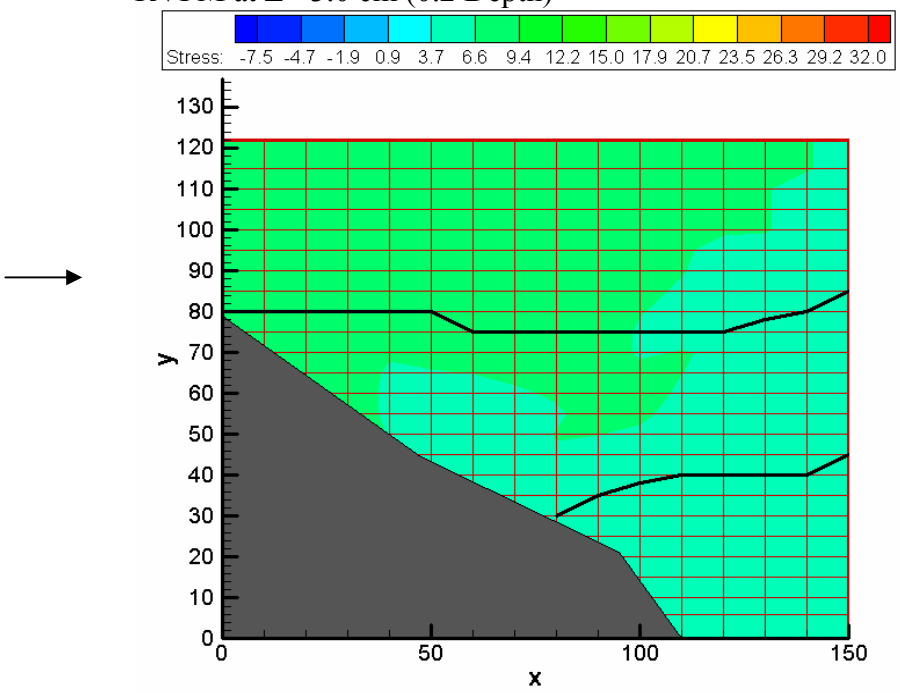

Figure 6.15 Contour Plot of Shear Stress (N/m^2) using $\tau_0 = \rho gHS$ at Z= 0.0 cm (Bed Depth)

Local Energy Loss

The mechanisms of local energy loss (h_f) associated with barbs are attributed to roughness, flow constriction, and the presence of the structure (blocked flow) (Kaatz and James, 1997). The change in total energy is defined by the conservation of energy equation:

$$\alpha_{app}\left(\frac{U_{app}^2}{2g}\right) + y_{app} + z_{app} = \alpha_{cont}\left(\frac{U_{cont}^2}{2g}\right) + y_{cont} + z_{cont} + k_e\left(\frac{U_{cont}^2}{2g}\right) + \bar{S}_f \Delta x_{cont} \quad (26)$$

where the subscripts "app" and "cont" refer to approach and contraction sections, respectively; α is the energy coeffiecient; U is the depth-averaged velocity in the x-direction; g is the acceleration due to gravity; y is the depth of flow; z is the vertical distance of the channel bottom above the datum; k_e is the local energy loss coefficient; $\bar{S}_f$ is the average friction slope through the contracted reach; and Δx is the change in distance in the longitudinal direction. The last two terms on the right hand side of Equation 6-10 account for the energy losses due to turbulence, flow separation, and friction (Molinas et al., 1998). In Equation 6-10 all variables are known except the energy coefficients (α) for the approach and contracted sections, the constraction velocity (U_{cont}), and the local energy loss coefficient (k_e). For this study, k_e represents the contraction loss coefficient.

The energy coefficient is a multiplying factor used in conjunction with the mean flow velocity component to compute the velocity head at a section (Chaudhry, 1993).

Calculation of the energy coefficients was achieved through an integrated process. An equation for U, the governing velocity flow component in the longitudinal direction, was first calculated. This was accomplished by taking the ADV flow measurements obtained at 02, 0.4, and 0.7 depths of the standard grid system, plus an additional velocity measurement obtained at 0.4 of the water column flow depth, and plotting these point measurements in excel. A best-fit polynomial line was fit to the data. The equation of this line (u(z)) was then integrated from zero to the total depth of the water column (z). The depth average velocity for the transect was then determined with the following equation:

$$U = \frac{1}{h}\int_0^z u(z)dz \tag{27}$$

From here α was calculated using the following equation:

$$\alpha = \frac{W}{AV^3}\int_0^z u(z)dz \tag{28}$$

where, W is the unobstructed transect width, A is the transect area, V is the depth average velocity, and u(z) is the equation generated in excel. Using this method, the computed energy coefficient values for the approach, constriction, and exit transects were 1.185, 1.100, and 1.435, respectively. An average for the velocity, area, and flow depth for each transect were computed by breaking the transect into sections (following stream surveying procedures) and averaging the data to obtain a "bulk" characteristic variable. The individual friction slope values for each partitioned section of the transect was determined using Equation 6-5 which incorporates both the velocity components in the x and y-directions. A "bulk" friction slope (S_f) was calculated by summing the individual values and dividing by the number of variables summed. In the contracted section, due to the sloping crest of the barb and lack of ADV measurements along the crest area, a more definitive measure was needed to calculate the velocity in the constricted section. The following equation from Xiangbai and Nianshen (1990) for a submerged spur dike was used to compute the effective discharge blocked:

$$Q_b = Db\left[U_{\max} - \frac{u_*}{k_1}\left(1 - \ln\left(\frac{2b}{B}\right)\right) - \frac{u_*}{k}\left(1 - \ln\frac{D}{H}\right)\right] \tag{29}$$

where, D is the height of the dike; b is the length of the dike; B is the flume width; U_{max} is the maximum point velocity in the transect; u_* is the shear velocity equivalent to $\sqrt{gRS_f}$; g is the acceleration of gravity; R is the hydraulic radius, S_f is the friction slope; k_1 and k are coefficients, 0.75 and 0.40, respectively; and H is the average depth. The effective discharge flowing through the constricted reach (Q_{cont}) was determined by subtracting the blocked discharge from the approach discharge. The velocity in the constricted section could then be discerned ($U_{cont} = Q_{cont}/A_{cont}$). The last unknown value, k_e, was then calculated using Equation 6-10. The calculated k_e-value was 0.59. Lastly, the total local head loss was calculated (0.034 meters) from the following equation:

$$h_f = \Delta x\bar{S}_f + k_e\left|\frac{\alpha_1 V_1^2}{2g} - \frac{\alpha_2 V_2^2}{2g}\right| \tag{30}$$

where points 1 and 2 are located well-upstream and downstream of the constriction.

In conclusion, the total local head loss was calculated as equal to 0.034 m from the barb hydraulic experiments.

Conclusions for objective 3

1. The UFM overpredicts the shear stress around the barb in the longitudinal direction. The RSSM provides the best predictions while the RVFM works well for the points found upstream of the barb.
2. The UFM overpredicts the shear stress in the longitudinal direction because the flow around the barb is 3-D and not 1-D as the UFM assumes.
3. Both RSSM and RVFM methods incorporate into their formulation the transverse or the vertical velocity component.
4. Friction losses in the barb are attributed to skin roughness (riprap), flow constriction, and the presence of the structure (size of barb, form roughness)

Objective 4. Backwater Analysis

An approach reach, contraction or obstruction reach, and an exit reach define flow in the vicinity of a constriction (Hunt et al., 1999; Molinas et al., 1998). Typically the exit reach is located four times the contracted width downstream (Hunt et al., 1999; Kaatz and James, 1997). The contracted width of this study is 0.46 meters, therefore the transverse transect for the exit reach was located at x=150. This is slightly less than four times the contracted reach, but was required to ensure flume outlet effects were not present. For this research the approach reach is defined at the transverse transect, x = -50 and the contraction reach was located at x=0. The location of the approach reach corresponds well to the distance upstream equivalent to the contracted width as suggested in the HEC-2 Bridge Analysis manual (Kaatz and James, 1997). The following figure further depicts the location of the above-mentioned sections.

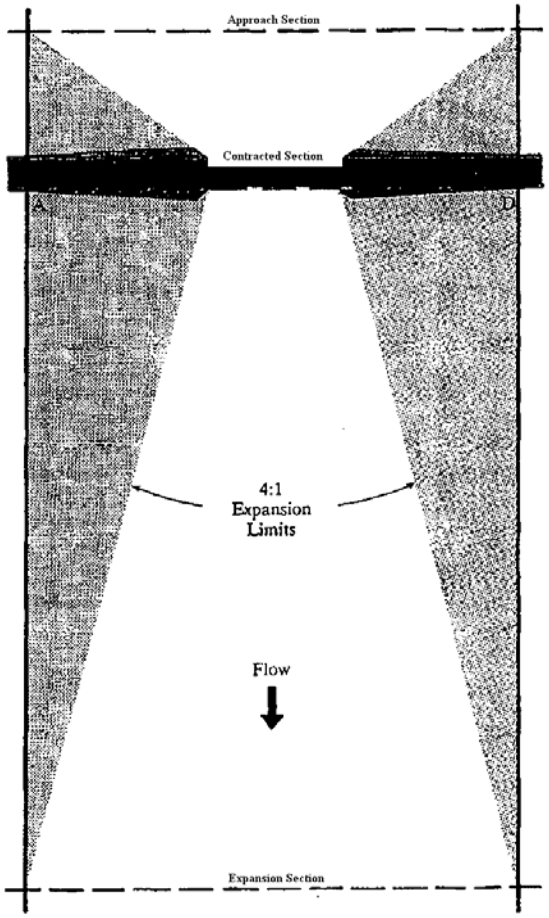

Figure 6.16 Schematic of Approach, Contraction, and Expansion Reaches (after Kaatz and James, 1997)

Backwater is defined as the increase in water surface elevation above the natural, unconstricted condition for a particular discharge due to a constriction of flow (Kaatz et al., 1997). As seen in Figure 6.17 backwater effects prevail upstream of the barb for the entire length of the flume.

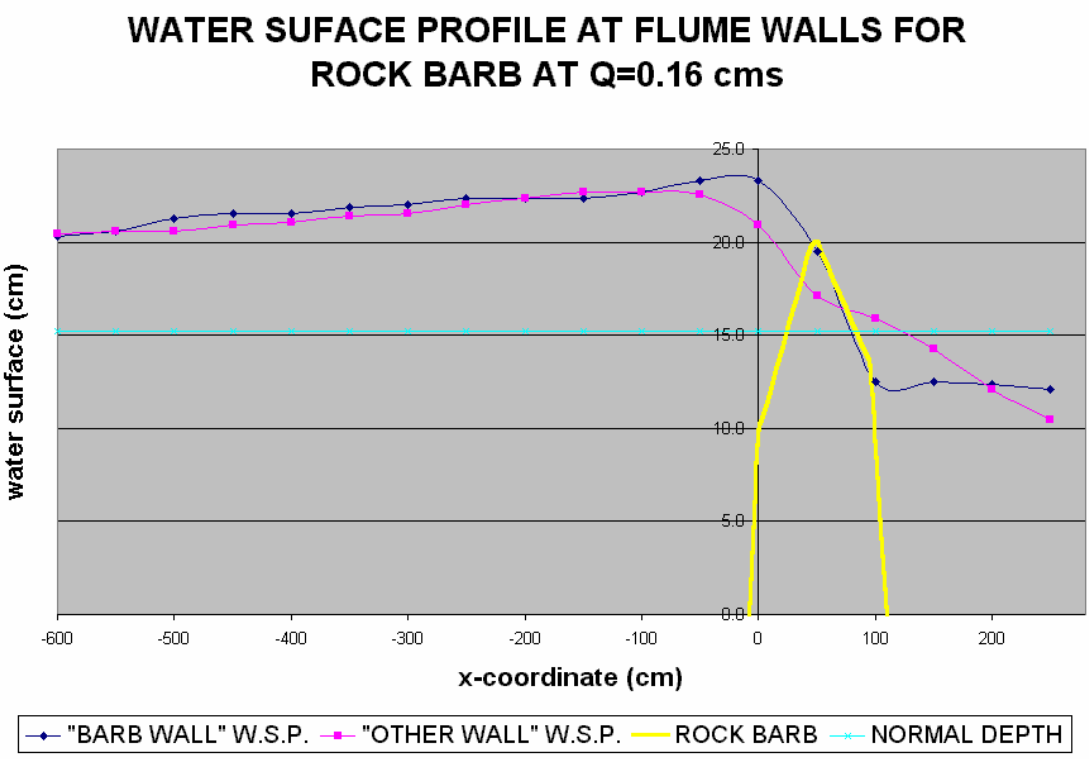

Figure 6.17 Water Surface Profile (WSP) Depicting Backwater Effects

Backwater was determined by using the direct step method. This method is appropriate for determining the location where a known specified flow depth would occur. By utilizing the following definitions:

$$z_2 = z_1 - S_0(x_2 - x_1) \tag{31}$$

$$E_1 = y_1 + \frac{\alpha_1 V_1^2}{2g} \tag{32}$$

$$E_2 = y_2 + \frac{\alpha_2 V_2^2}{2g} \tag{33}$$

$$\bar{S}_{fx} = \frac{1}{2}\left(S_{f_1} + S_{f_2}\right) \tag{34}$$

the location, or the change in longitudinal direction, can be found as follows:

$$x_2 = x_1 + \frac{E_2 - E_1}{S_0 - \frac{1}{2}\left(S_{f_1} + S_{f_2}\right)} \tag{35}$$

where, the subscripts 1 and 2 refer to sections 1 and 2, respectively; S_0 is the slope of the channel bottom slope; x is the distance in the longitudinal direction; E is the specific energy; and other variables are as previously defined (Figure 6.18). The average slope method for calculating $\bar{S}_f$ returns a value with the lowest error when the distance

between sections 1 and 2 is short, or the flow depths, y_1 and y_2, are not significantly different (Chaudhry, 1993). For this case, the small differences in flow depth, 0.19 meters (normal flow depth for maximum discharge of 0.16 cms) at section 2 and 0.26 meters at section 1 validate the use of the average friction slope formula. Plugging the known variables into Equation 6-19 results in a change in longitudinal distance, or backwater effects, of –62.93 meters. The negative sign indicates that section 2 is upstream from section 1.

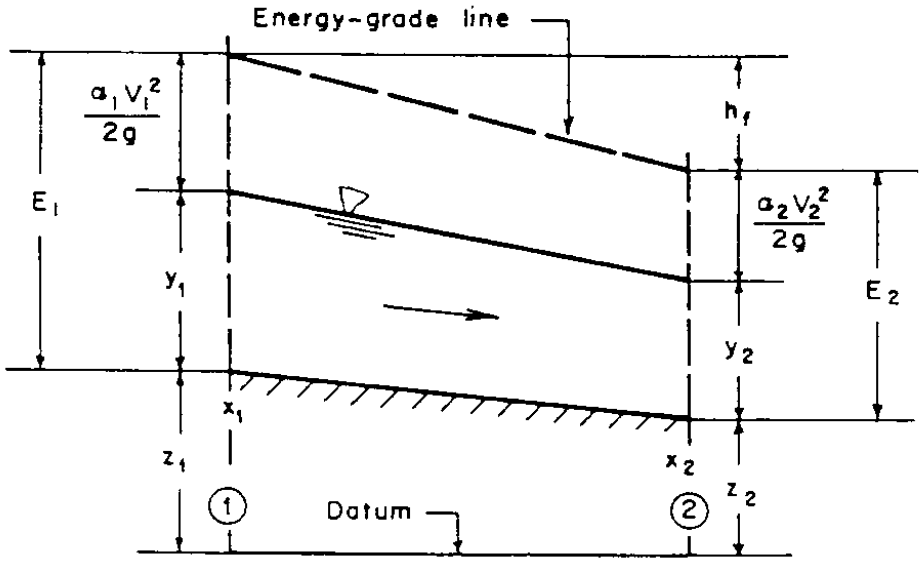

Figure 6.18 Schematic of Direct Step Method Variables (after Chaudhry, 1993)

Conclusions for Objective 4

Figure 6. 17 clearly indicates that the backwater effects propagate upstream at a distance of at least 6 m. In the field this will be about 54 m, assuming that we deal with a straight stretch channel. Therefore, caution should be used in employing the findings of this research in meandering river stretches or stretches that have small bed roughness. The designer should determine spacing of two subsequent barbs by taking into consideration the increase in the water depth due to the flow constriction caused by the barb. The presence of scour pools may reduce backwater effects but this reduction will not be significant. The researchers found that when the dimensionless distance between 2 subsequent barbs is about 13 no pronounced backwater effects are present between the 2 subsequent barbs (see objective 7).

Objective 5. Develop a generic scour equation that predicts the evolution of the scour hole volume and depth in gravel beds under varied flow conditions

The local patterns and magnitudes of flow and sediment movement in the vicinity of a significant local feature of a channel, such as a hydraulic structure, is of prime interest to hydraulic and restoration engineers (ASCE, 2003). Modeling of loose boundary flow provides a basis for determining the maximum depth of scour and aids in the design of more hydraulically stable structures. Coupling of scour measurements with near-bed turbulent flow parameters is imperative for the development of scour formulas that incorporate the transient nature of flow in the vicinity of a structure.

This research investigates the interaction of unsteady turbulent producing flow with scour hole progression and makes both qualitative and quantitative comparisons between the flows over immobile and mobile beds. Furthermore, it also models mobile bed scour migration utilizing a relatively uniform streambed gravel substrate. This is of particular importance due to the lacking research to date using gravel material in scour analysis. Typically past experimental studies were conducted with sand beds. The scour mechanics on a temporal and spatial basis for sand and gravel produce much different results (Kuhnle et al., 2003). This is attributed to the difference in submerged particle weight, fall velocity, and relative roughness between the two materials.

Scour in the vicinity of hydraulic structures is a compilation of local scour and contraction scour. As stated by Melville and Coleman (2000), local scour depths are strongly dependent on the protruding length of the structure, alignment with the flow, and to a lesser extent the shape of the structure. Contraction scour is caused by the increased concentration of streamlines due to the reduction in flow area.

The mechanics of flow and erosion in mobile bed channels has not been well defined and it is not possible to confidently estimate the geometric changes that may occur during channel forming flow (Melville and Coleman, 2000). Mobile roughness, induced by entrainment, affects the relationship between water movement and the deformable nature of particulate boundaries (ASCE, 2000). Existing scour formulas, mainly empirical, are based on flume studies conducted with sand beds; steady uniform flow and hydrostatic pressure conditions; and impermeable non-submerged hydraulic structures. Consequently, the prediction of maximum scour depth is typically over-estimated.

From the available literature, numerous scour equations were used to predict the maximum depth of scour. Table 6.3 shows the variability in scour depth determined for one case flow (three times incipient motion) generated under clear water scour conditions.

LOCAL SCOUR SUMMARY:

Parameters: Clear Water - Three times incipient flow conditions

Equation	d_s m	Comments
Lim (1997)	0.31	90 degrees
	0.33	Using correction factors for angle to flow (1.05) - From Melville (1997)
Froehlich (1989)	0.58	Assumption made for depth of flow at abutment & Ve computation
	0.48	std dev = 1.1
	0.35	std dev = 1.3
Laursen (1963)	0.70	Abutment encroaching into main channel / Assumes vertical blunt-ended, normal wall
		Assumed value for approach flow depth (includes backwater depth)
	0.33	Using correction factors for shape (0.45) and angle to flow (1.05) - From Melville (1997)
	0.58	Calculated value for approach flow depth (includes backwater depth)
	0.27	Using correction factors for shape (0.45) and angle to flow (1.05) - From Melville (1997)
Melville (1997)	0.35	Assumes linear backwater effect to estimate approach flow depth
Melville (1992)	0.27	Assumes flow depth does NOT include depth effects due to backwater
	0.34	**WRONG** according to Melville, 1997 interpretation - Assumes flow depth at constriction - estimate
	0.35	Assumes approach depth includes depth effects due to backwater - estimated
Ghodsian &Tehrani (2001)	0.19	R = 0, 90 degrees

CONTRACTION SCOUR SUMMARY:

Parameters: Clear Water - Three times incipient flow conditions

Equation	d_s m	Comments
Gill (1981)	0.07	Threshold conditions in approach channel
		Using correction factors for angle to flow (1.05) - From Melville (1997)
Komura (1966)	0.33	Assumes std dev = 1.0 / Assumes depth in unconstricted **with** backwater effects
	0.15	Assumes depth in unconstricted **without** backwater effects

Table 6.3 Analysis of Predicted Maximum Scour at 3x's Incipient Flow and Clear-Water Flow Conditions

A main objective of the scour analysis was to determine the maximum depth of scour for varied flow conditions induced by the permeable barb. This entailed comparing the maximum scour depth along the streamwise direction for each flow region (main core flow, shear layer region, and stagnant wake region). A second objective was to map the volumetric evolution of scour with the progression of time.

Procedures

Scour tests were run for 7 different clear-water flow rates ranging from incipient motion to channel forming flow. These flow rates are as follows:

Test SB1 – flow at incipient motion (0.034 cms)

Test SB2 – flow at 1.5 times incipient motion (0.051 cms)

Test SB3 – flow at 2.0 times incipient motion (0.068 cms)

Test SB4 – flow at 2.5 times incipient motion (0.084 cms)

Test SB5 – flow at 3.0 times incipient motion (0.102 cms)

Test SB6 – flow at 4.0 times incipient motion (0.136 cms)

Test SB7 – flow at approximately 5.0 times incipient motion (0.163 cms, channel forming flow for prototype)

where incipient motion refers to the onset of particle motion due to the presence of the structure (not incipient motion of the upstream reach).

Prior to running the scour tests, a pre-test at maximum flow condition was run to determine the geometric extent of scour. From this preliminary test it was concluded that four transects along the longitudinal would suffice in adequately capturing the volumetric and geometric progression of scour over time. These four transects were located longitudinally and transversely, respectively, at x = 15 cm and y = 75 to 115 cm; x = 45 and y = 55 to 115 cm; x = 75 cm and y = 35 to 115 cm; and x = 105 cm and y = 20 to 115 cm (Figure 6.16). Transects began near the nose where the largest concentration of flow prevailed and ended downstream approximately at the end of the structure.

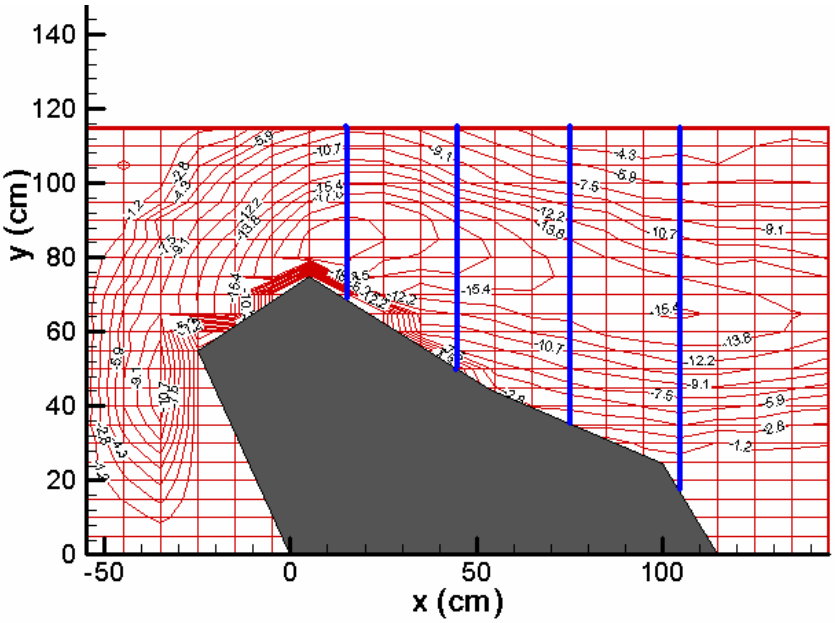

Figure 6.19 Contour Plot Showing Location of Transects

Incremental time steps for each test were determined using engineering judgment based upon visual examination and extent of scour depth change from the previous time step. As the flow rate was increased the rate of change, or rate of scour, also occurred at a more rapid pace (Papanicolaou, 1997). As such it was necessary to adjust the time accordingly between transects to sufficiently capture the progression of scour. Typically, at the early stages of a test where significant erosion occurs collection of sediment occurred more frequently than at later stages.

Sediment collection of the eroded material was captured at two different locations along the outlet pipe. The first site was located immediately at the flume outlet. Removable wire baskets with mesh liners were fed into the pipe by removing the upper portion of the backwater pipe section at the outlet. Another area of collection was located downstream of the outlet pipe. Again the upper portion of the pipe was removed and a wire screen was installed to collect sediment. The second site collected sediment overflow from the first collection site. The collected sediment for each incremental time was dried and weighed.

The first two test runs, SB1 and SB2, were conducted making both transect measurements and collecting weight samples simultaneously for incremental time steps until equilibrium scour conditions prevailed. At test SB3 it was no longer feasible to make both transect measurements and collect weight samples at the same time. Therefore, tests SB3, SB4, and SB5 were run as a two-step process. First the test was run collecting only weight measurements until it was feasible to collect weights and survey transects simultaneously again. The test was then rerun a second time to collect transect measurements.

For the last two tests, SB6 and SB7, it was physically impossible to collect the sediment at incremental time frames due to the high amount of bed material transported downstream. At these flow rates the outlet pipe began to overflow at the sediment collection sites. To rectify this problem it was necessary to replace the pipe lids and seal them shut. A final collection of sediment was taken at the end of each test. To compensate, the last two tests were each run three times and then averaged. In summary, tests SB1, SB2, SB4, and SB5 were each run once in their entirety, and tests SB3, SB6, and SB7 were each run three times.

Data collected was entered into the computer and analyzed using Microsoft Excel and Tecplot 8.0. The following section show the scour results obtained for tests SB1 through SB7.

Maximum Depth of Scour

The overall change in scour depth for each test run was established by subtracting the initial bed survey from the final bed survey. A maximum value, d_{sm}, was then obtained for each individual test run. The water depth, H, was calculated by means of rulers mounted along the flume wall. For each test the water surface depth was recorded in 50 cm increments from x = –600 cm (upstream of structure) to x = 250 cm (downstream of the structure). For all tests the water depth recorded at x = -400 was utilized for the value of H.

Sediment related values were obtained from a sieve analysis conducted by the supplier, Atlas Sand and Gravel. The lab test data supplied were plotted and the following values were obtained:

d_{16} = 4.7 mm

d_{50} = 7.1 mm
d_{84} = 9.8 mm
where, d_{16}, d_{50}, and d_{84} represent the 16th, 50th, and 84th percent finer grain diameters, respectively. From this information the geometric standard deviation, σ_g, of the sediment size distribution was calculated as 1.44, where

$$\sigma_g = \sqrt{\frac{d_{84}}{d_{16}}} \tag{36}$$

A geometric standard deviation of 1.44 is representative of a fairly uniform sediment (well-sorted) distribution.

Following the work of Maxwell and Papanicolaou (2001) for gravel bed streams the maximum scour depth is provided in a dimensionless form via the π-theorem. The dimensionless maximum scour depth is determined to be a function of a modified form of the Froude number, relative submergence, and the geometric standard deviation. Because the protruding length, angle of inclination, and permeability were held constant throughout the tests, these parameters were not considered in the equation. The equations for these two parameters (π-theorem) are shown, respectively.

$$\pi_1 = \frac{d_{sm}}{H}\sigma_g^{1/2} \tag{37}$$

$$\pi_2 = \left[\frac{Q}{\sqrt{gH^5}}\left(\frac{d_{50}}{H}\right)^{1.5}\right] \tag{38}$$

Figure 6.20 shows the variation of these two parameters. Use of the volumetric discharge instead of the local streamwise velocity makes this relation widely applicable to cases where velocity measurements are lacking. The experimental results are in close agreement with the aforementioned relation.

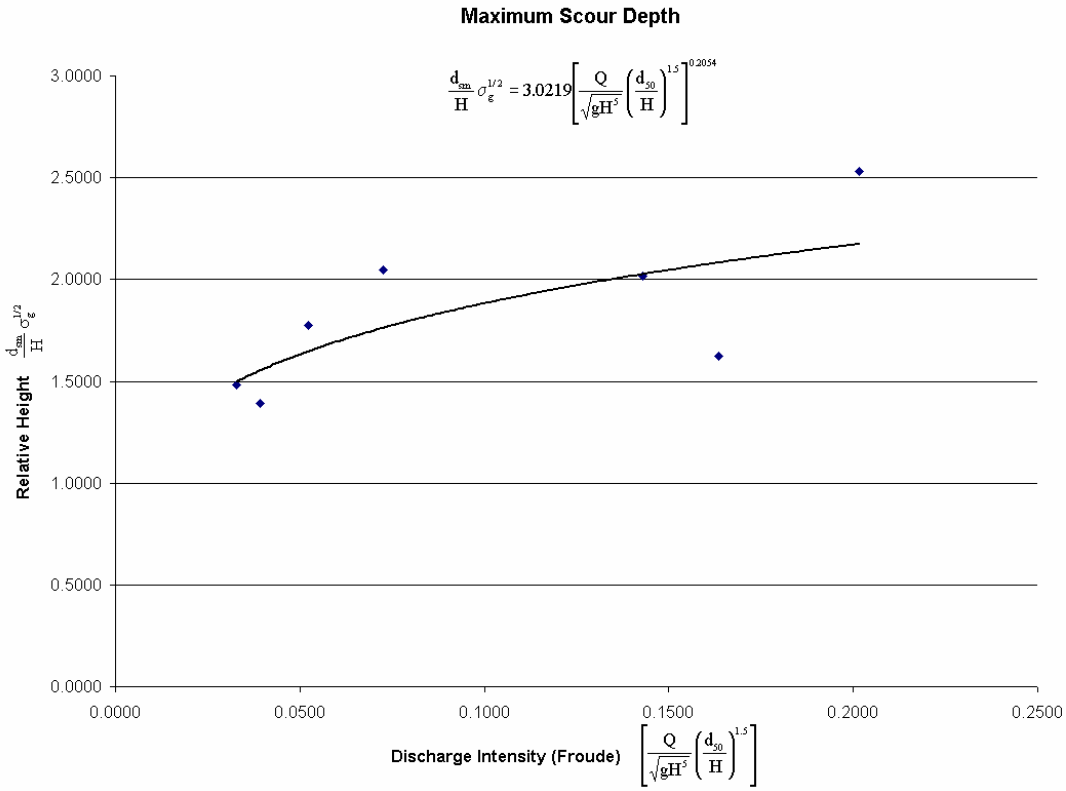

Figure 6.20 Plot of Maximum Scour Depth in Comparison to Maxwell and Papanicolaou (2001)

Investigation of a semi-empirical maximum scour depth equation proposed by Prezdwojski (1995), as reported by Sukhodolov et al. (2000), for groynes in a meandering river shows results less favorable. The maximum scour depth equation is as follows:

$$d_s = \beta H\left[\frac{y}{H} + \frac{Q_b}{Q}\cos\left(\frac{2\pi}{L}s\right) + \sin(\theta - 90)\right]^{b-2} \qquad (39)$$

where, d_s is the maximum scour depth, β is a coefficient, H is the mean flow depth, y is the unperturbed depth of flow, Q_b is the flow discharge blocked by the barb, Q is the flow discharge, L is the meander length, s is the distance from the entrance of the bend, θ is the angle of inclination, and b is the exponent in the sediment transport equation. The equation can further be simplified for the case of a straight reach with symmetrical channel to:

$$d_s = 53\left[1.707 + \frac{Q_b}{Q}\right]^{-1.7946} \qquad (40)$$

assuming that β=3.0219, H=17.5419 cm (flow depth for test SB7), y=H, and b=0.2054. Further manipulation of the obstructed flow ratio ($Q_b/Q = 0.282$) yields a maximum scour depth of 15.43 cm. In comparison to the actual maximum scour depth, 17.54 cm (test SB7), this equation under predicts the maximum depth of scour by almost 40%. Equation (40) was developed for alluvial channels.

There are very few studies that have examined scour in gravel bed streams. The maximum scour depths obtained in this research are compared against results from Buffington et al. (2002). Specifically, the normalized ratios of the scour depth to bankfull flow depth and obstruction width to bankfull flow depth for this research were calculated and compared with Buffington et al. (2002) experimental data for a vertical obstruction. The value of the first ratio is tabulated (Table 6.4) and ranged from 0.7 to 1.4. The second ratio was approximately 5. From Figure 6.21 it is shown that these values correspond to the upper scour regime, as determined by Buffington et al. (2002). This was particularly meaningful when considering the angle of inclination in the Buffington et al. experiment was 90 degrees as compared to the 130-degree angle of inclination for this study. Whereas, reported by many, (e.g. Kuhnle et al., 2002) the 135-degree angle is expected to cause larger scour holes.

Test	Max Scour Depth d_{smax} cm	Bankfull Flow Depth d_{bf} cm	Ratio of d_{smax} / d_{bf} (Dimensionless)
SB1	-10.6759	15.24	0.70
SB2	-17.5816	15.24	1.15
SB3	-15.6666	15.24	1.03
SB4	-20.8756	15.24	1.37
SB5	-20.5581	15.24	1.35
SB6	-18.5738	15.24	1.22
SB7	-21.6958	15.24	1.42

Table 6.4 Ratio of Maximum Scour Depth to Bankfull Flow Depth

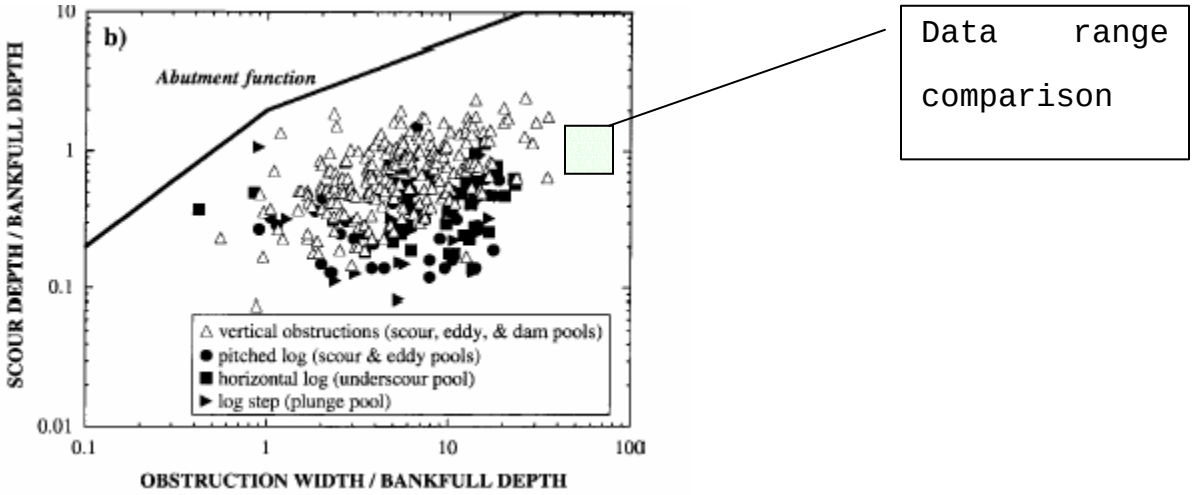

Figure 6.21 Plot from Buffington et al. (2002)

In conclusion, the maximum scour depth for test SB5 were compared with the predicted scour values (Table 6.3). These scour equations are based on clear-water flow conditions for sand bed streams. Out of the six formulas, it was found that all formulas over predicted the maximum scour depth except for the Ghodsian and Tehrani (2001) formula

(20.56 cm). This can be attributed to the fact that this equation was obtained from tests run with a permeable submerged structure and relative coarse sand.

Maximum Depth of Scour (3 Flow Regimes)

Three representative cross sections were taken along the centerline of each flow region (main core flow, shear layer region, and stagnant wake region) for all test cases. In the main core flow, Figure 6.22 shows that the maximum scour depth along the centerline occurs in the same general vicinity for all test conditions except test SB2. It is also shown that the shape of the scour hole along the centerline for all tests roughly follows the same trend.

Test SB2 shows a shift of the scour hole further downstream indicating the presence of overtopping. Upon review of test photos taken showing the submergence of the structure it was estimated that approximately 7-8 cm of the nose section was submerged during test SB2. It is speculated that this small extent of overtopping created a plunging effect on the bed. Test SB2 appears to be at a transitional stage between non-submerged and partially submerged conditions, and as such, has a combined effect of deflected flow around the structure and non-dissipated overtopping flow.

It is important to note that the shift in scour depth observed in tests SB1 through SB6 (not including SB2) are typical for unsubmerged vertical structures (test SB7 considered fully submerged condition). The research provides a qualitative comparison of these results with Nwachukwu and Rajaratnam (1980); a study conducted for scour of unsubmerged 90-degree oriented abutments. Although the study by Nwachukwa and Rajaratnam shows scour depth shapes that are similar with those of tests SB1, SB3, SB4, SB5, SB6, and SB7; it does not show the shift in the location of the maximum scour depth observed in test SB2.

The scour profile plotted for the centerline of the shear layer region (Figure 6.22) illustrates the scour pattern upstream and downstream of the structure. Upstream of the structure scour has the same shape for all tests SB1 through SB7. At low flow conditions, (e.g. SB1), there is negligible upstream scour. With progression of tests, and thus an increase in flow, the depth of scour upstream of the structure increases in depth in a predictable pattern. Plainly stated, as flow increases scour depth also increases.

Downstream of the barb scour depths along the centerline are about equivalent for tests SB4 and SB5 upstream and downstream of the barb. Figure 6.22 confirms the results depicted in the contour plots (Figures 6.24A & B through 6.30A & B) where sediment deposition occurs downstream of the barb. The deposition zone shifts within the shear layer region towards the wake region. This explains why SB5 and SB6 have smaller scour depth than SB4.

Lastly, Figure 6.23 depicts the scour profile plotted for the centerline of the stagnant wake region. The figure illustrates the scour patterns upstream and downstream of the structure. Upstream of the structure there is little or no scour for tests SB1 and SB2. With the increase in flow for subsequent tests the depth of erosion progressively

increases for tests SB3, SB4, SB5, and SB7 and a clear trend can be seen. It is shown that test SB6 does not follow this trend; no appreciable amount of scour occurs upstream of the structure.

Downstream of the barb scour depths along the centerline show a pattern of erosion for SB1, SB2, and SB3, then deposition for tests SB4 and SB5. The depth of erosion gets progressively less from test SB1 to SB3. There is a large jump from Test SB3 to SB4 marking the transition from erosion to deposition. As the flow increases the deposition declines in test SB5 and tends toward a plane bed configuration for tests SB6 and SB7. The results shown in the contour maps (Figures 6.24A & B through 6.30A & B) further illustrate these trends. This confirms that the movement of the shear layer region affects the stagnant wake region.

In comparison to the trends shown in the previous region (shear layer region) it is notable that the depth of deposition is of the same magnitude. The difference being that in the shear layer region deposition occurs in tests SB1, SB2, and SB3 while in the stagnant wake region deposition occurs in tests SB4 and SB5. It is also shown that the depth of scour is approximately 9 and 15 times larger in the shear layer region for tests SB6 and SB7, respectively, when compared to the stagnant wake region. Again this confirms that the deposition zone shifts within the shear layer region towards the wake region. It also shows that faster flows produce scour holes that have much steeper side slopes than those created in slower moving flows.

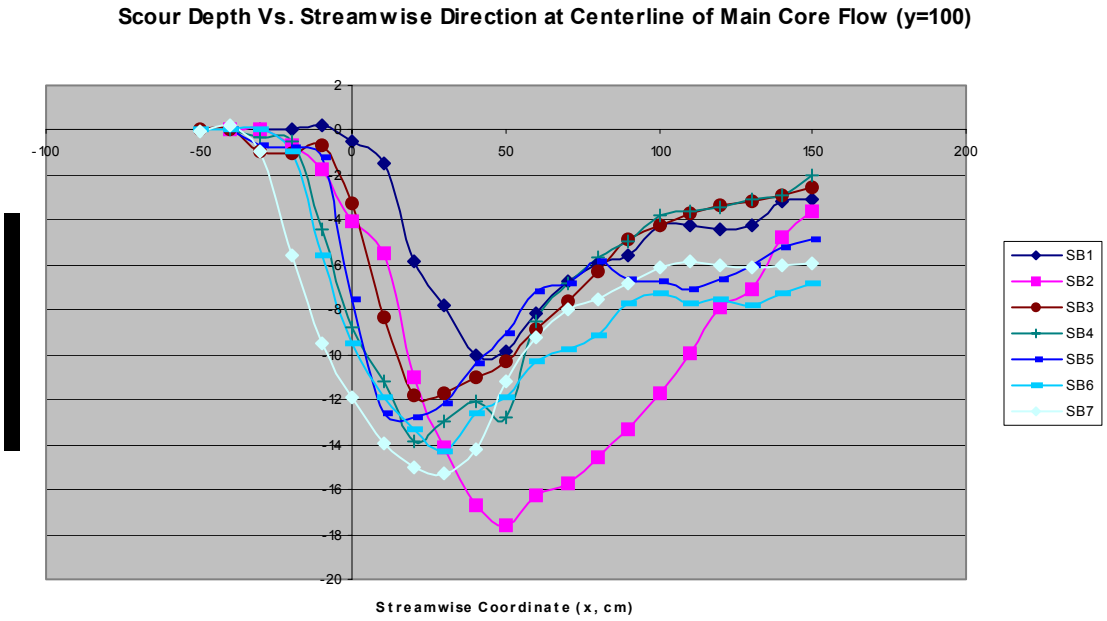

Figure 6.21 Profile Plot of Main Core Flow at Y = 100 cm

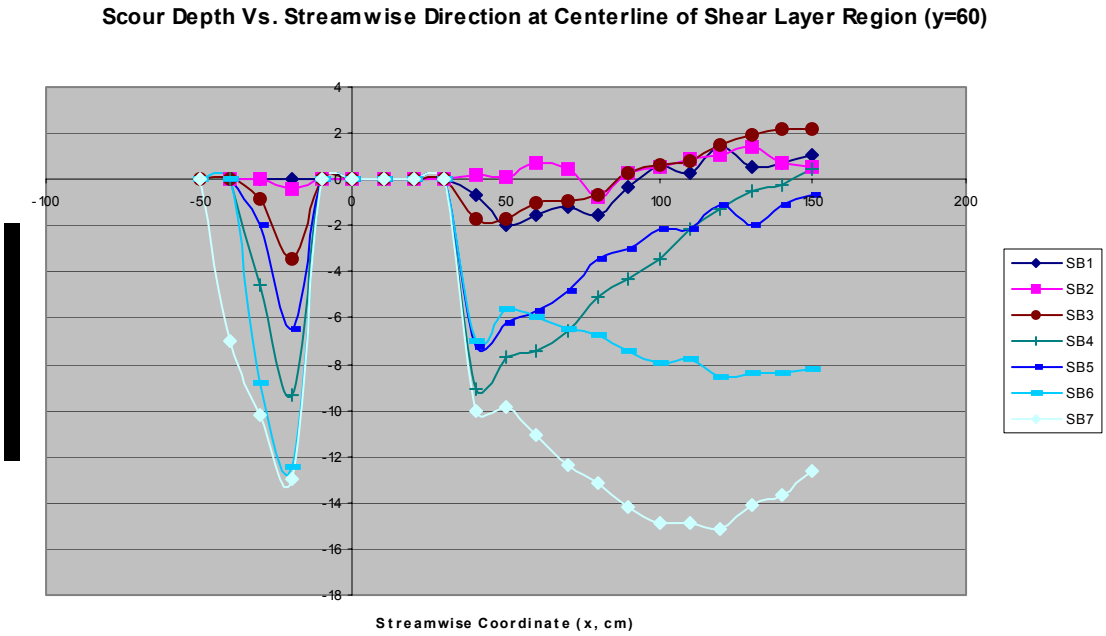

Figure 6.22 Profile Plot of Shear Layer Region at Y = 60 cm

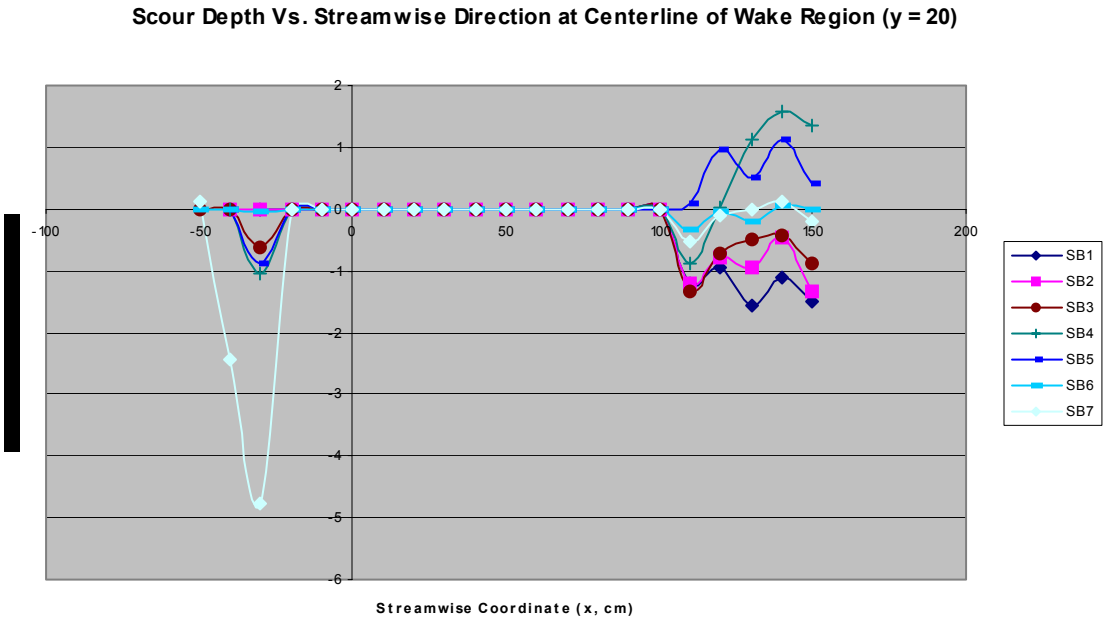

Figure 6.23 Profile Plot of Wake Region at Y = 20 cm

Total Scour and Deposition (Contour Maps)

The contour maps generated for each test provide a quantitative description of the effective scour and deposition zones and the associated trend of each flow. These trends depict a spatial shift of scour with the increase of flow. There is a depositional zone forming within the leeward area of the test section for tests SB1 through SB5. While no depositional zones were observed for tests SB6 and SB7, it is clear that a zone of deposition was present along the shear layer for tests SB1 and SB2. As flow increases deposition primarily only occurs in the stagnant wake region where sediment finds protection.

The primary vortex appears to play a significant role as the relative submergence of the barb increases. As a result scour occurs at the frontal section of the barb for tests SB3, SB4, SB5, SB6, and SB7. This scour occurs all the way to the back eddy region. Figures 6.24A & B through 6.30A & B show the extent of scour and deposition for each test flow.

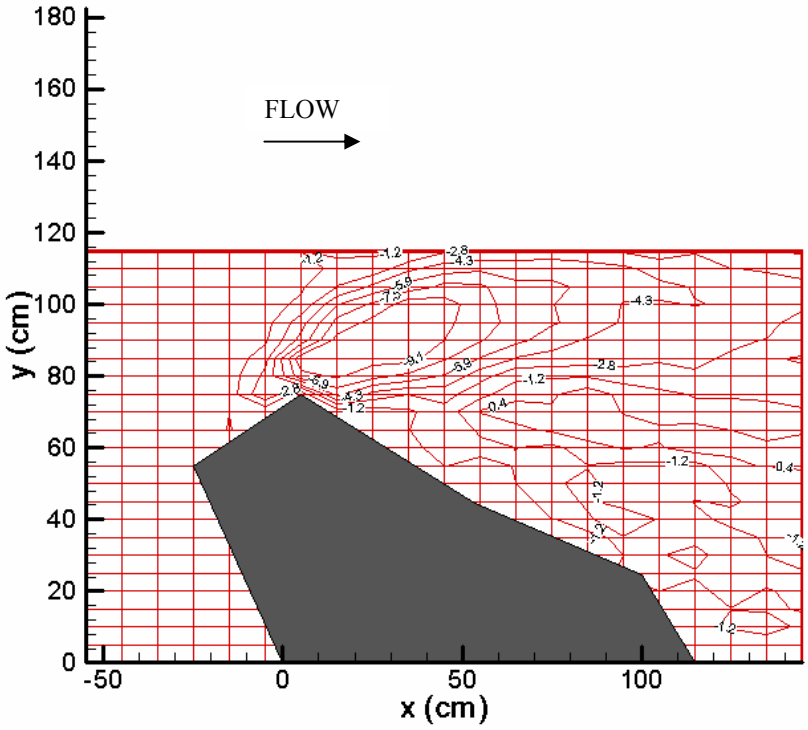

Figure 6.24A Elevation Contour Map,
Z (Depth) in cm (Test SB1 - 0.034 cms)

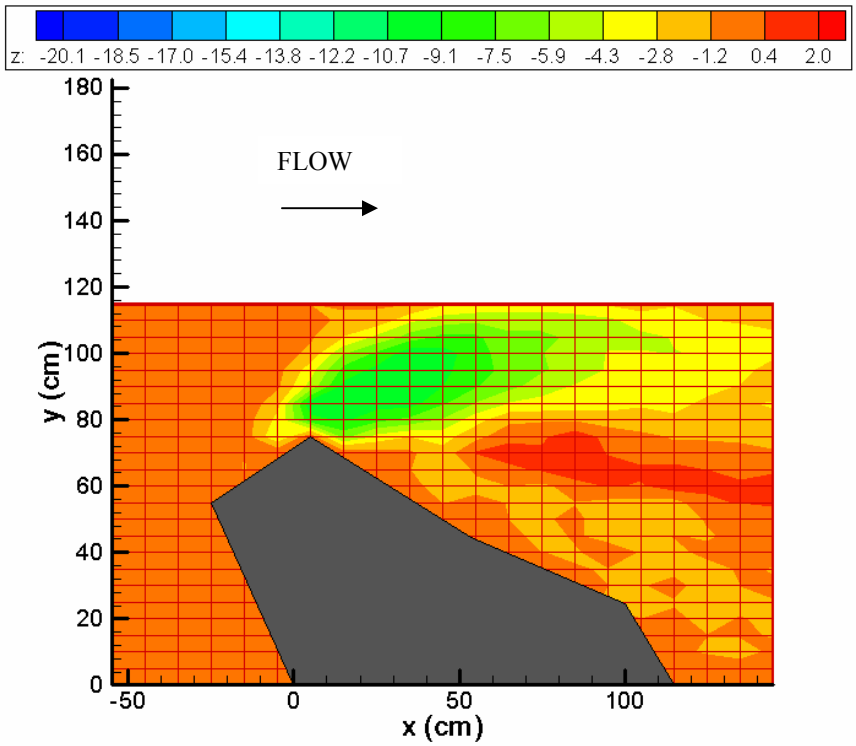

Figure 6.24B Elevation Contour Map in Color Pallets,
Z (Depth) in cm (Test SB1 - 0.034 cms)

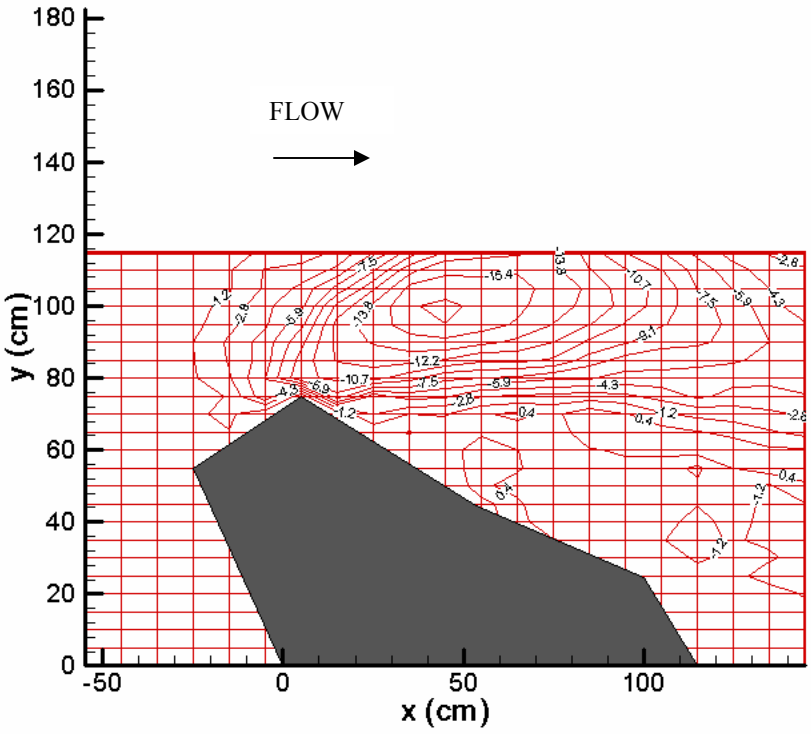

Figure 6.25A Elevation Contour Map,
Z (Depth) in cm (Test SB2 - 0.051 cms)

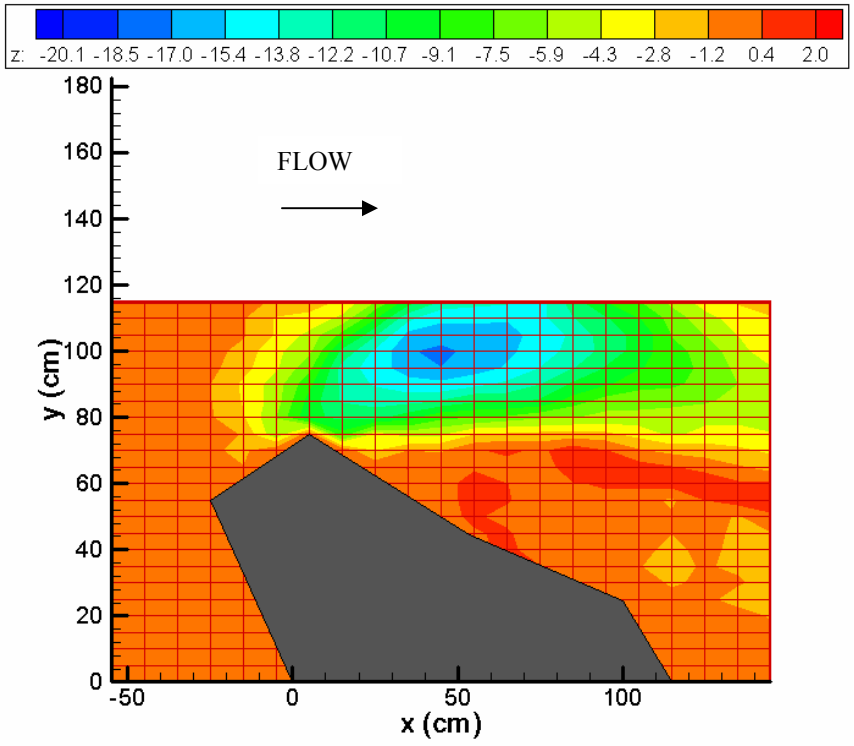

Figure 6.25B Elevation Contour Map in Color Pallets,
Z (Depth) in cm (Test SB2 - 0.051 cms)

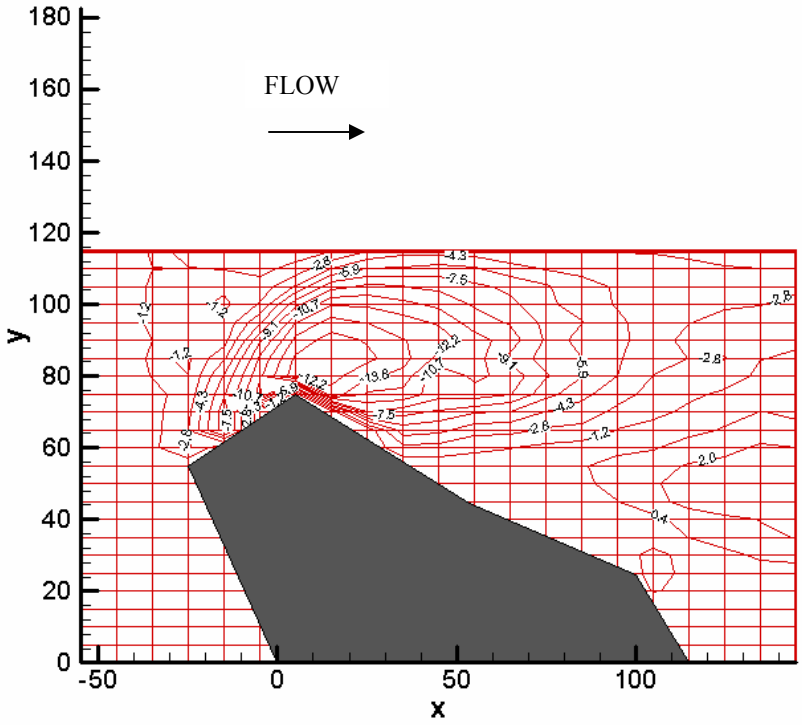

Figure 6.26A Elevation Contour Map,
Z (Depth) in cm (Test SB3 - 0.068 cms)

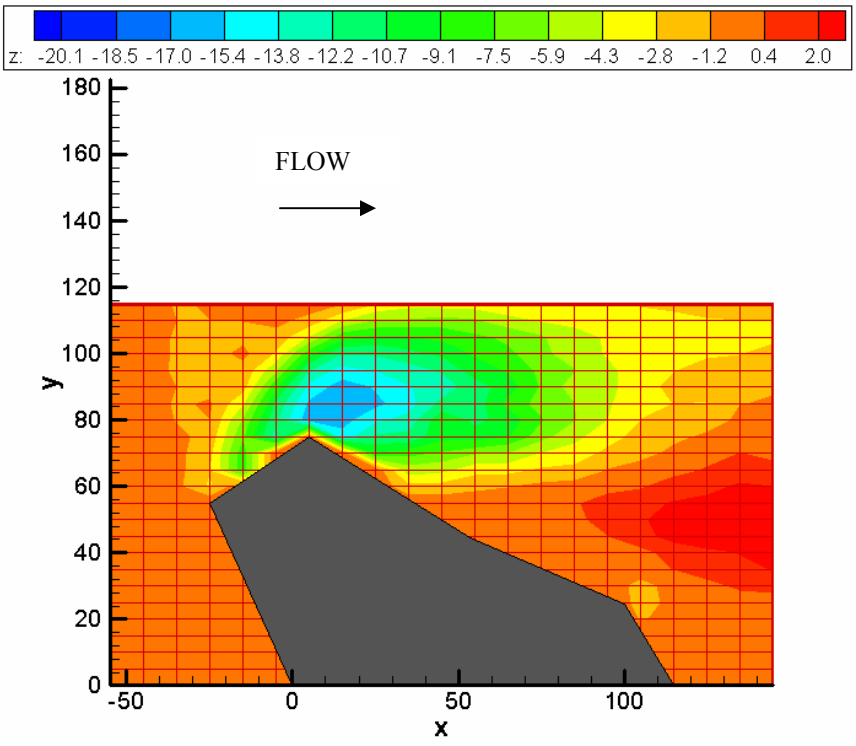

Figure 6.26B Elevation Contour Map in Color Pallets,
Z (Depth) in cm (Test SB3 - 0.068 cms)

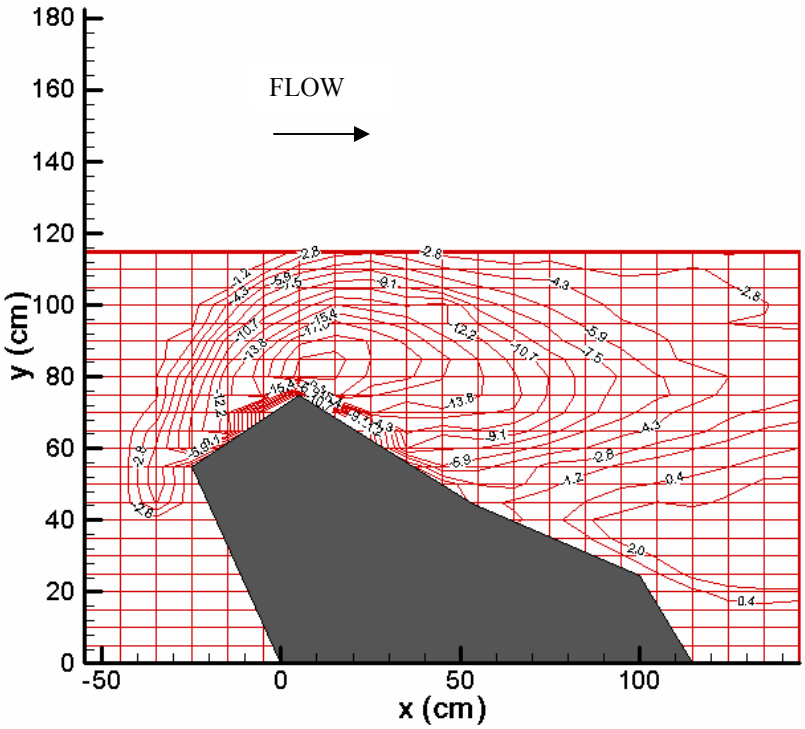

Figure 6.27A Elevation Contour Map,
Z (Depth) in cm (Test SB4 - 0.084 cms)

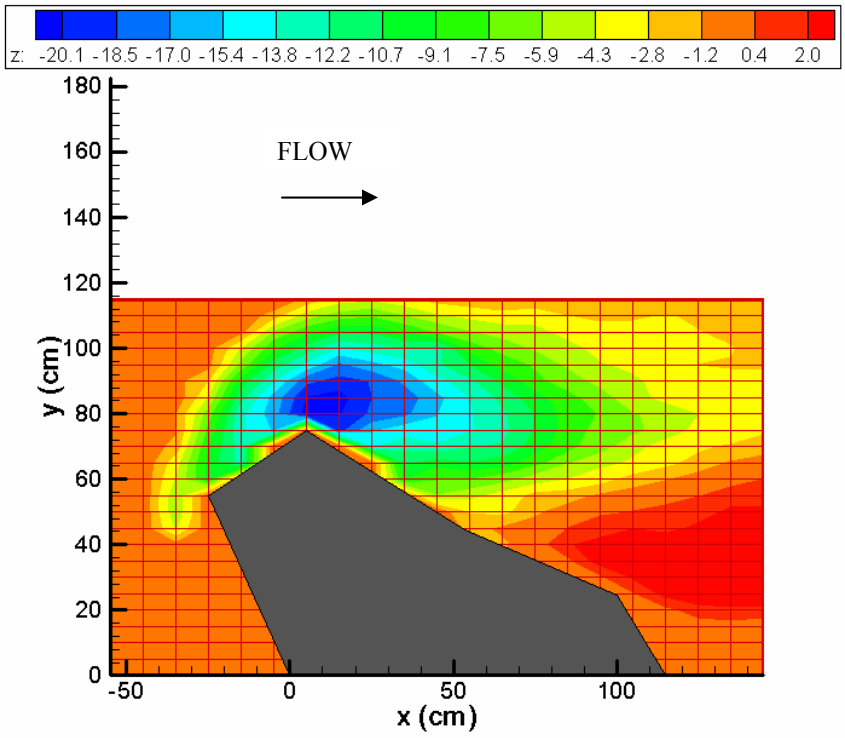

Figure 6.27B Elevation Contour Map in Color Pallets,
Z (Depth) in cm (Test SB4 - 0.084 cms)

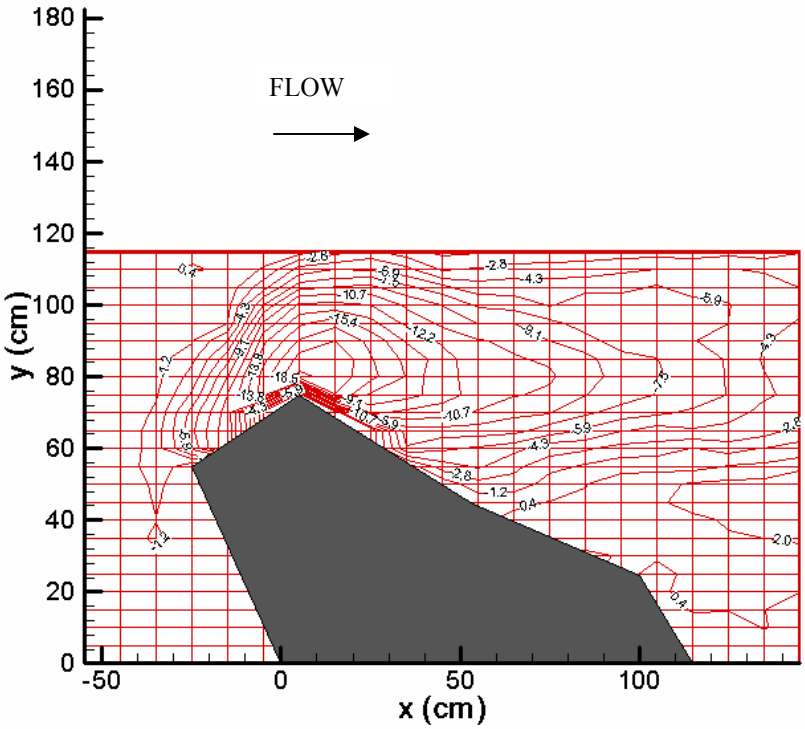

Figure 6.28A Elevation Contour Map,
Z (Depth) in cm (Test SB5 - 0.102 cms)

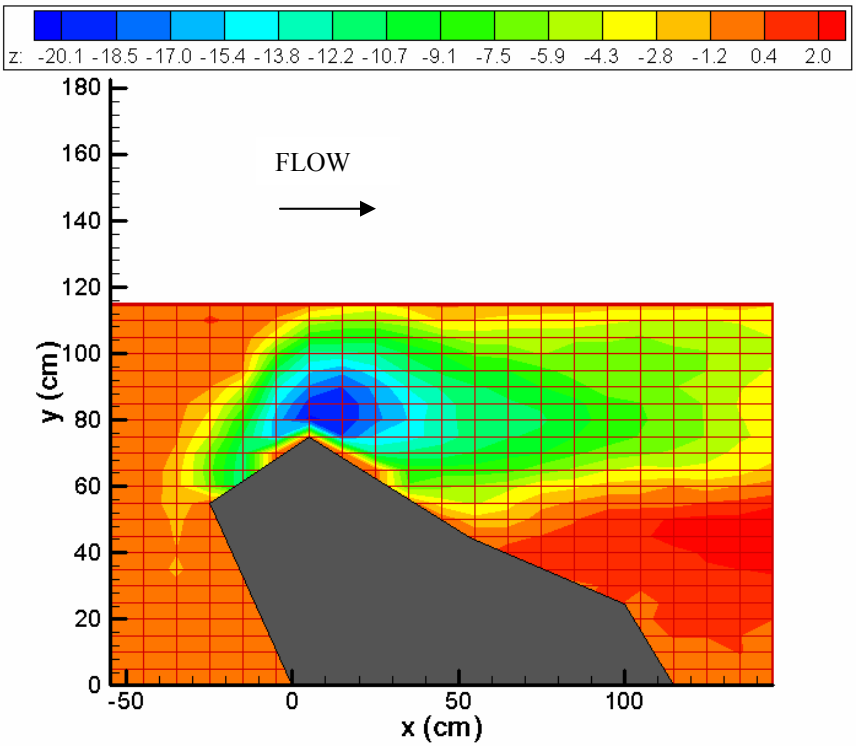

Figure 6.28B Elevation Contour Map in Color Pallets.
Z (Depth) in cm (Test SB5 - 0.102 cms)

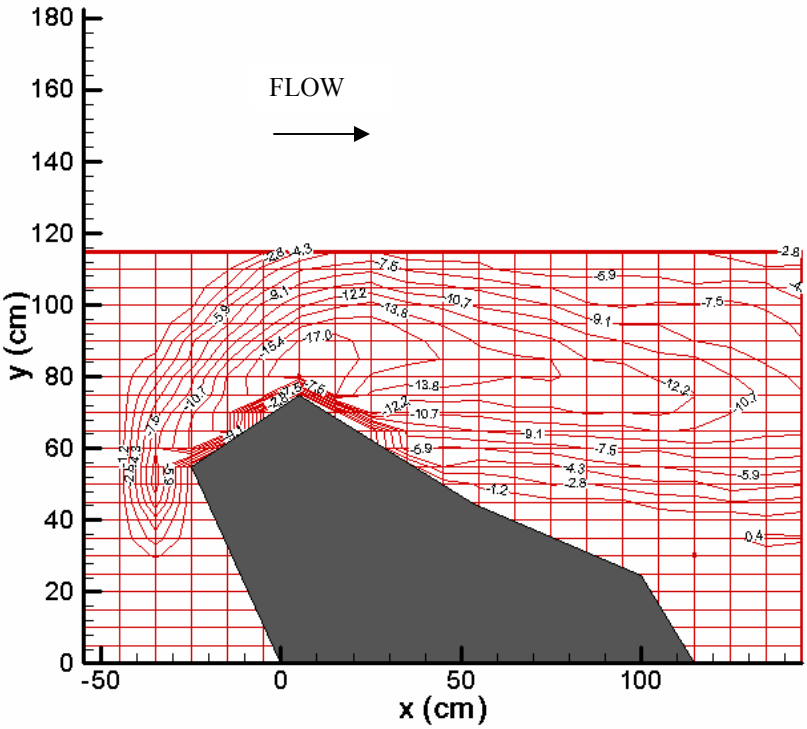

Figure 6.29A Elevation Contour Map,
Z (Depth) in cm (Test SB6 - 0.136 cms)

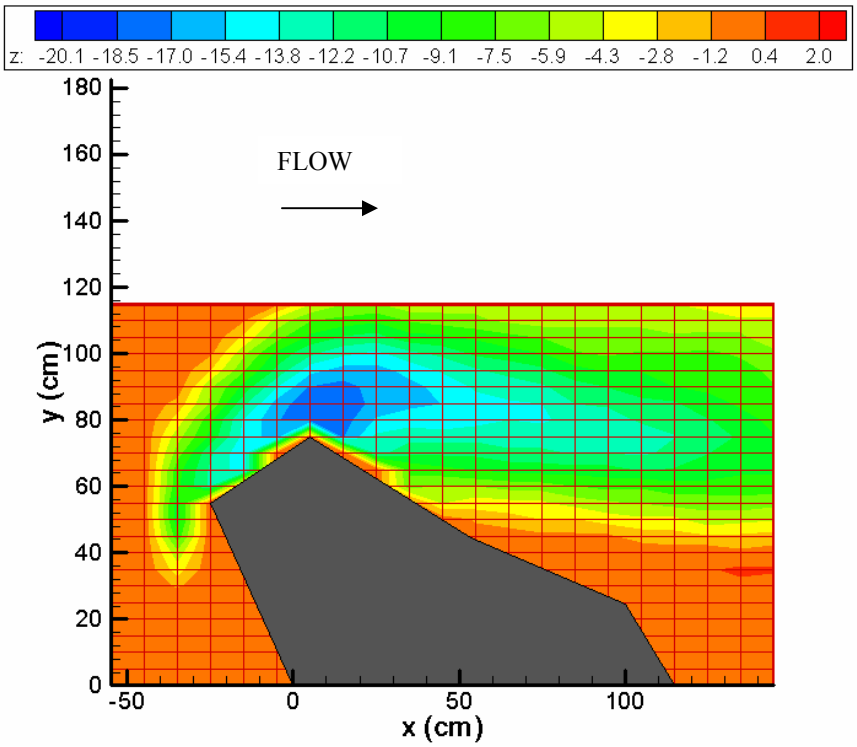

Figure 6.29B Elevation Contour Map in Color Pallets,
Z (Depth) in cm (Test SB6 - 0.136 cms)

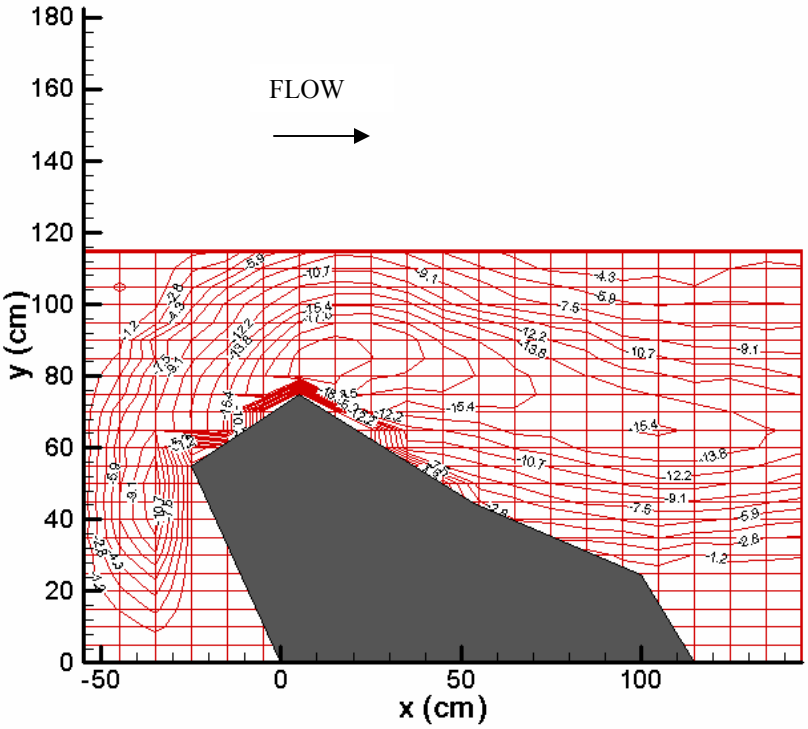

Figure 6.30A Elevation Contour Map,
Z (Depth) in cm (Test SB7 - 0.163 cms)

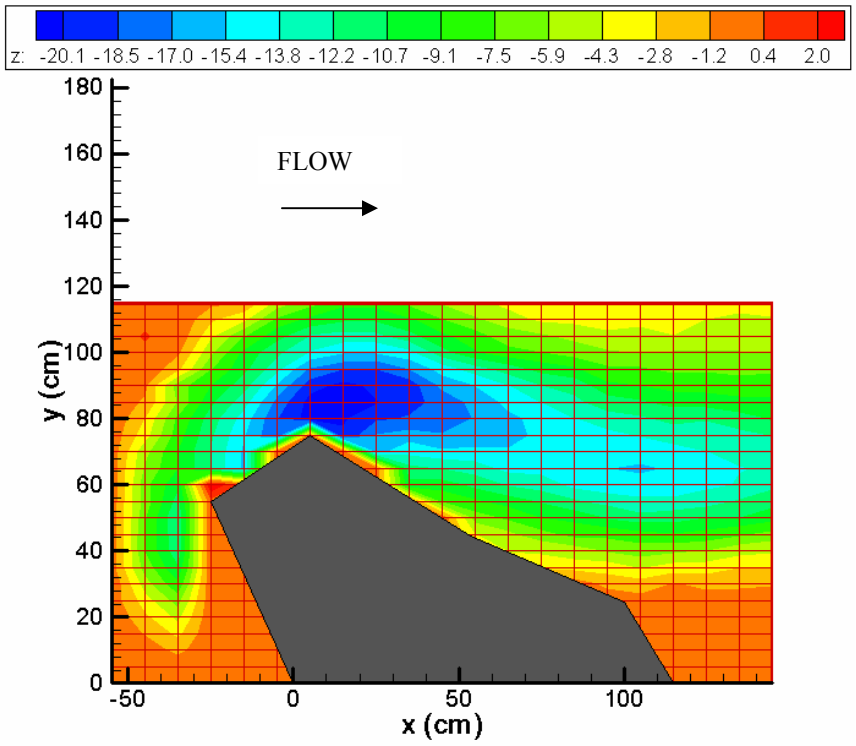

Figure 6.30B Elevation Contour Map in Color Pallets,
Z (Depth) in cm (Test SB7 - 0.163 cms)

6.76.4 Maximum Depth Scour & Deposition

Figure 6.31 shows the location of the maximum depth of scour and deposition within the three main flow regions. The maximum scour depth ranges from 10.7 cm at test SB1 to 21.7 cm at test SB7. The maximum deposition heights are 1.61, 1.57, 3.91, 5.91, 4.62, 0.64, 0.58 for tests SB1 to SB7, respectively. The table within Figure 6.28 quantifies these points in terms of layers (or multiples) of d_{50}.

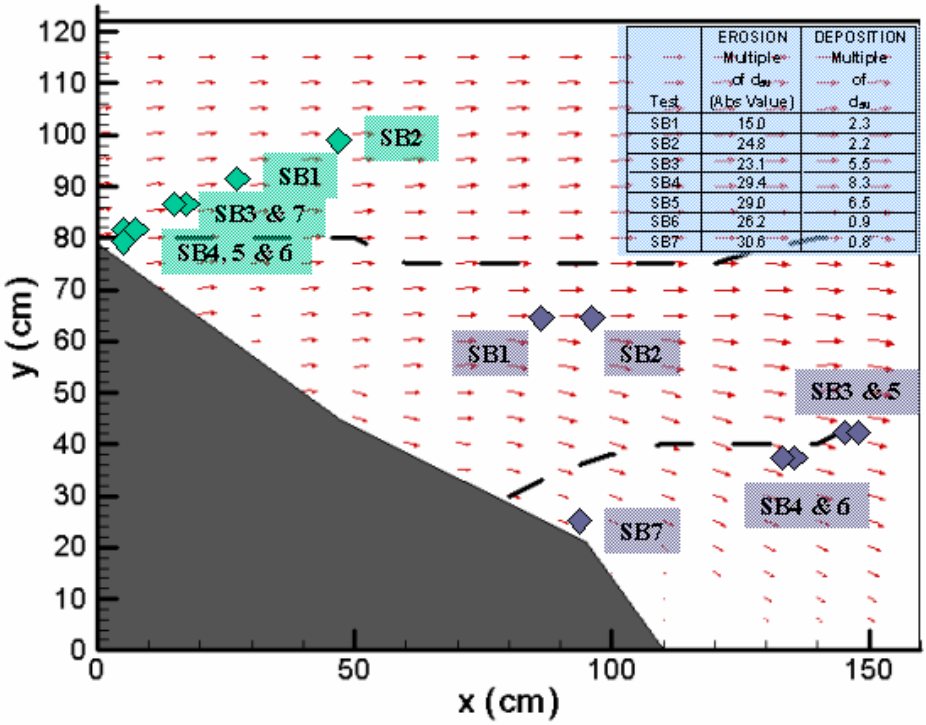

Figure 6.31 Points of Maximum Scour and Deposition

From an engineering point of view it appears that: (i) this design verifies the notion that 135-degree oriented barbs create sizable pools, and (ii) the structure may collapse at the nose area due to the local scour in the this vicinity of the structure.

6.7.5 Volume Versus Time

Figures 6.32 through 6.38 provide unique information (for the first time on gravel bed streams) about the volumetric evolution of a scour hole. Plots of the variation of the dimensionless volumetric ratio, V_i/V_T, with respect to dimensionless time ratio, t_i/t_T, are presented for all experimental cases. The terms V_i and V_T correspond to the volume of the scour hole as related to the incremental time (t_i) and total time (t_T) of each test, where incremental time infers the time at which scour transects were taken and total test time infers the time at which equilibrium scour conditions prevail. Because the same size sediment was used in all tests, t_T is only dependent upon discharge (Q).

Determination of the incremental volume was based on an end area average method. Transect measurements taken at incremental time steps within the scour test were used to calculate cross-sectional areas. The area was then averaged with the subsequent cross sectional area. This was then translated into a volumetric measurement by multiplying the averaged end area by the difference in longitudinal distance between the two areas.

Figure 6.32 (SB1) shows that equilibrium conditions were obtained at a time ratio of approximately 0.48. Figure 6.33 (SB2) shows that the volumetric scour change with time does not approach unity until almost the end of the test (t_T). For this test, the scour geometry never fully realized an equilibrium state, which implies the presence of transient flow features imposed by the relative submergence of the barb (overtopping) and possibly the presence of a plunging jet that caused the shift of d_{sm}, the maximum scour depth, in the main core flow.

Equilibrium conditions are reached at a time ratio of 0.18; 0.5; 0.28; 0.4; and 0.65, respectively, for tests SB3, SB4, SB5, SB6, and SB7. Tests SB3, SB6, and SB7 were performed three times each to examine the variability of the data. It was determined that the deviations of the data are close to the standard experimental error of 6%. Sources of error may be attributed to depth measurement readings obtained via the use of a ruler and /or the time at which the initial transect measurements were made. (In the initial stages of the test, especially at high flows, significant scouring occurs.)

Finally, all data are presented in one plot (Figure 6.39) and compared with the results of Kuhnle et al. (2002) for sand bed streams. It was found that scour hole geometries from the tests of this research were smaller than those reported by Kuhnle (as expected). The maximum depth of scour for this research was 21.7 cm (8.5 inches) and 30.05 cm (11.8 inches) for the Kuhnle experiments. And secondly, it was found that clear water scour equilibrium conditions are reached faster than in the case of a sand bed. Kuhnle et al. did not determine equilibrium times for each test run, however, an elapsed time of 30 hours was used to report their data. It was assumed that 30 hours allowed the scour hole geometry to reach equilibrium conditions.

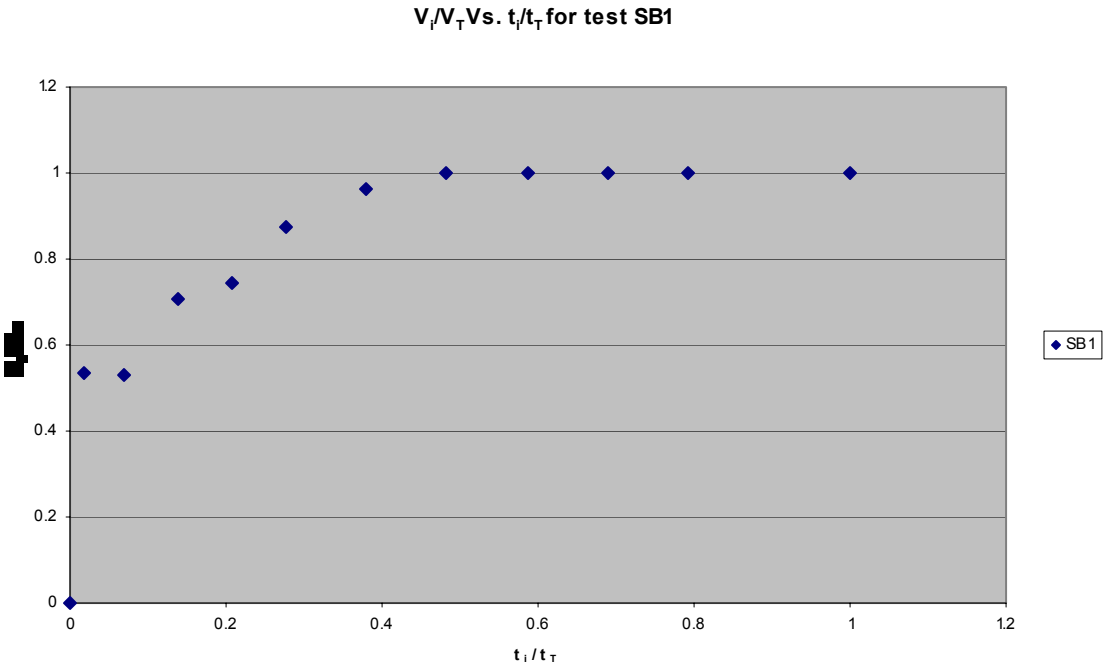

Figure 6.32 Volumetric Scour Ratio Versus Time for Test SB1

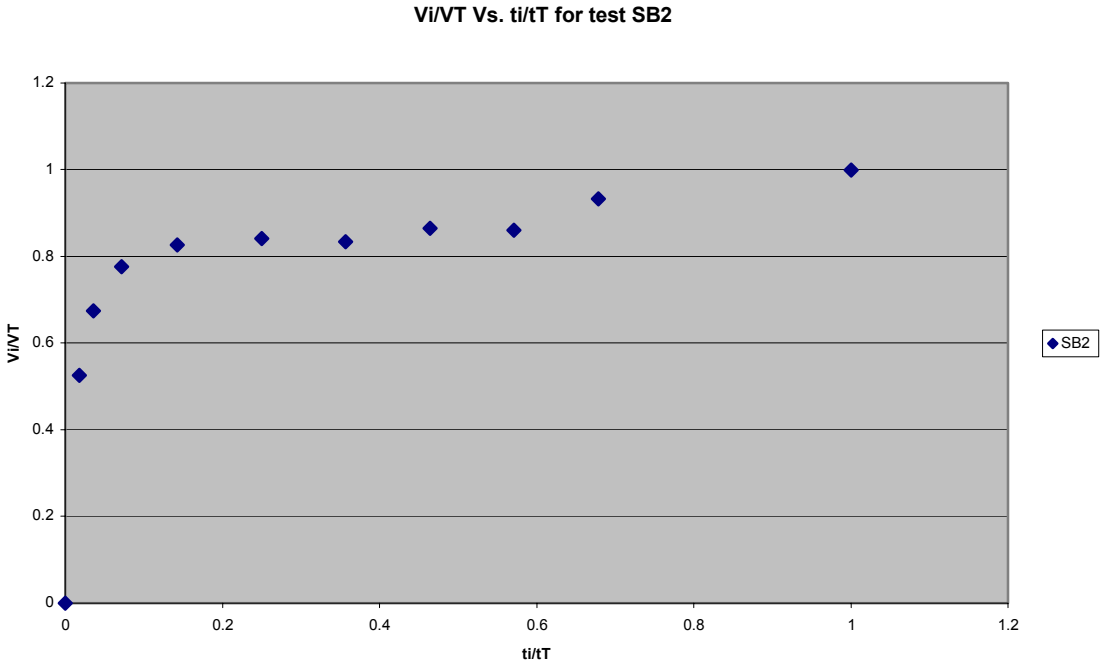

Figure 6.33 Volumetric Scour Ratio Versus Time for Test SB2

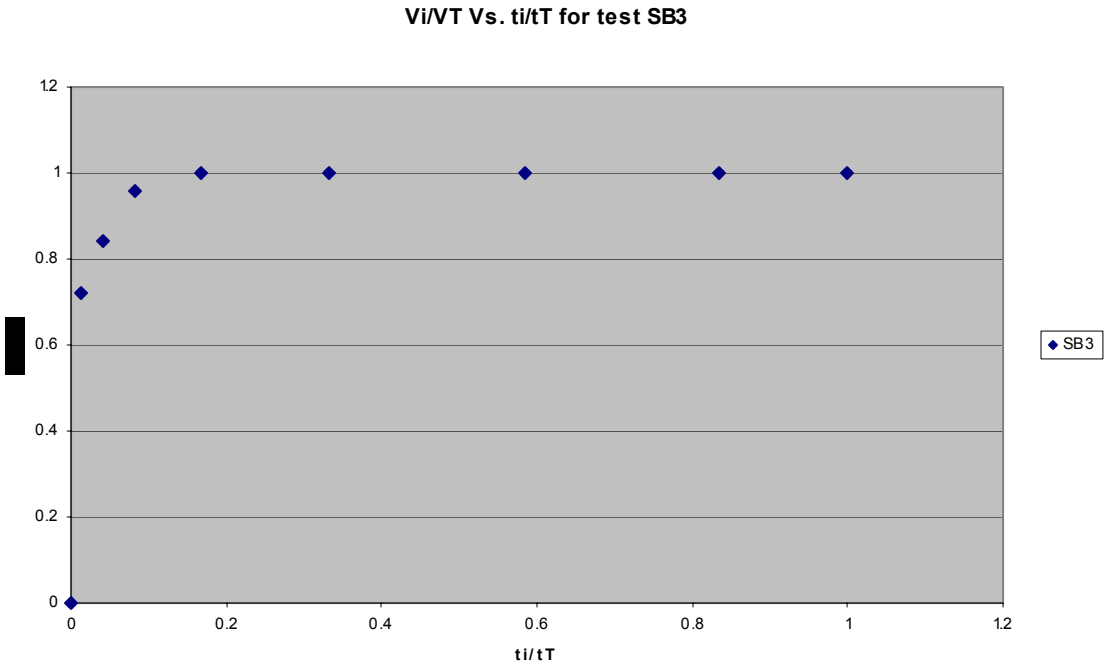

Figure 6.34 Volumetric Scour Ratio Versus Time for Test SB3

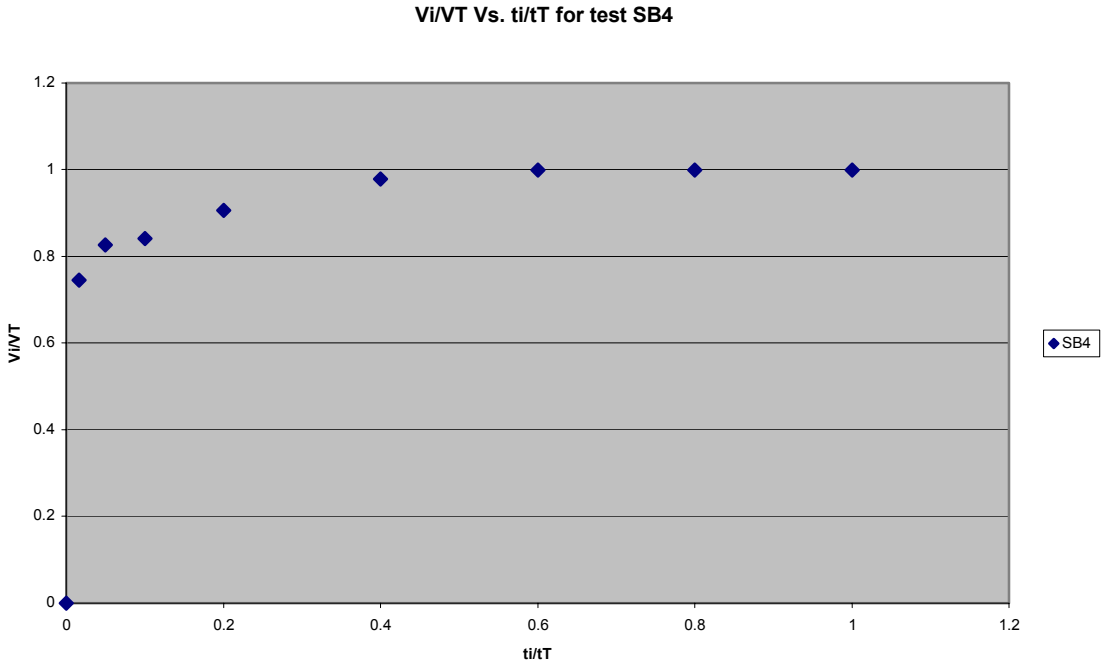

Figure 6.35 Volumetric Scour Ratio Versus Time for Test SB4

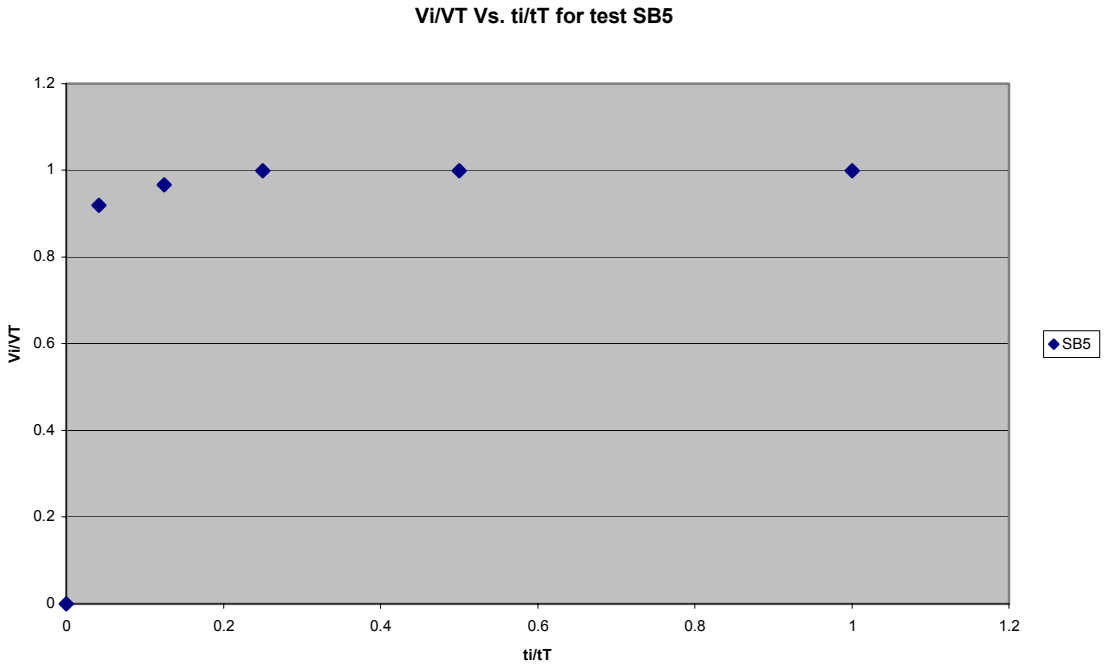

Figure 6.36 Volumetric Scour Ratio Versus Time for Test SB5

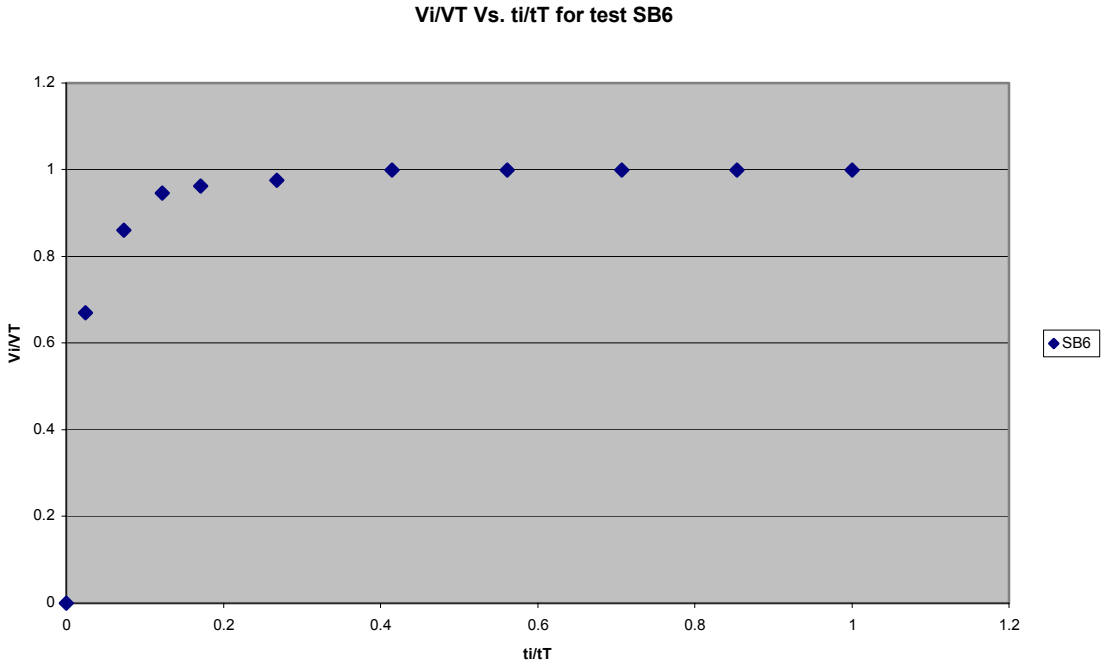

Figure 6.37 Volumetric Scour Ratio Versus Time for Test SB6

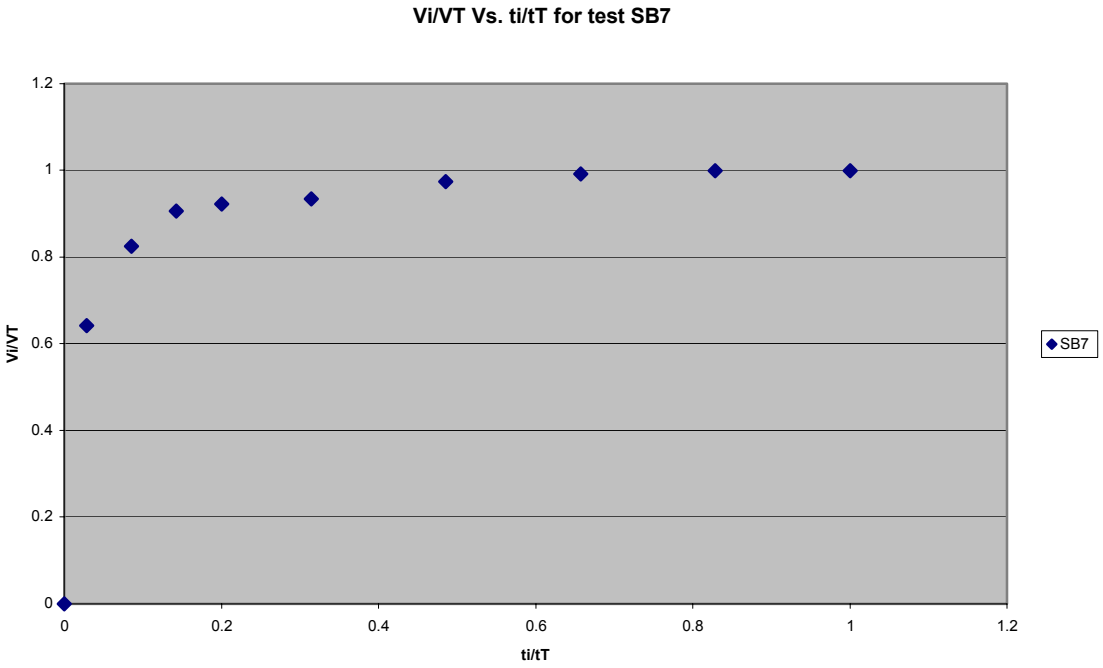

Figure 6.38 Volumetric Scour Ratio Versus Time for Test SB7

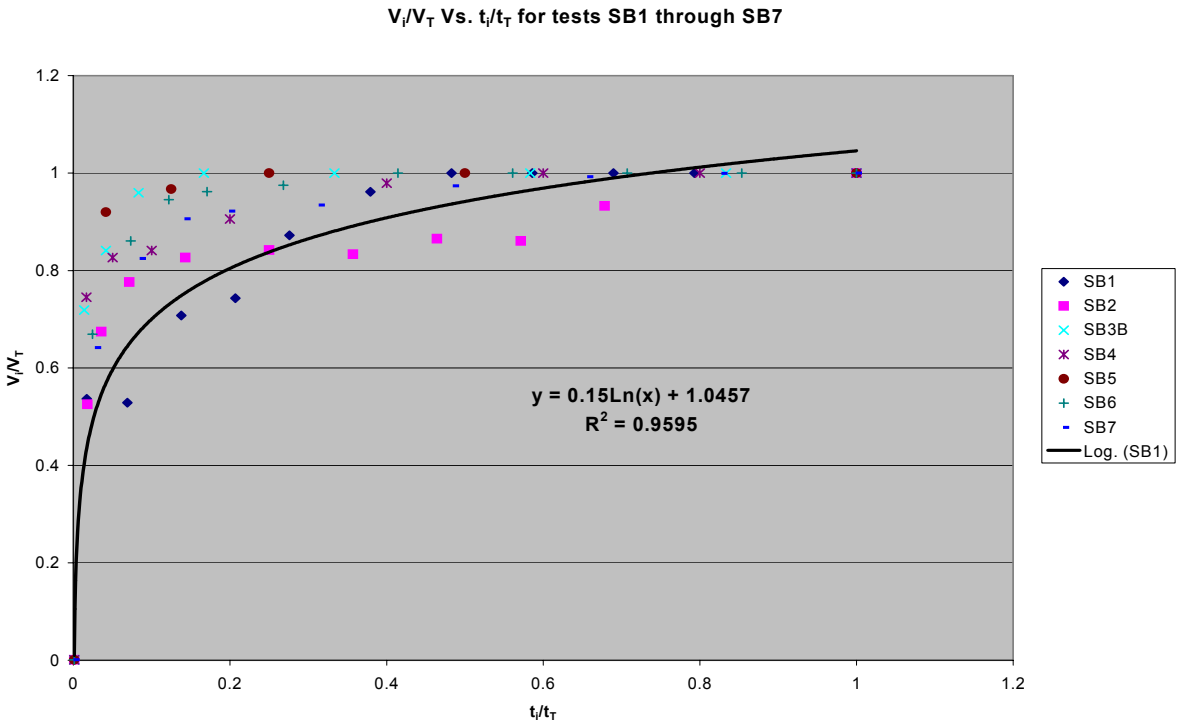

Figure 6.39 Volumetric Scour Ratio Versus Time for Tests SB1 to SB7

Objective 7. Assess barb optimal protected streambank and spacing criteria using large scale particle image velocimetry.

The objective of this task is to provide optimal protected streambank spacing criteria for one and multiple barbs, respectively, in a straight river reach. Using fixed-bed modeling with the modeled channel-forming discharge, large-scale particle image velocimetry is utilized to calculate the time-averaged fluid velocity field.

Streambank protection refers to the distance downstream of the barb for which flow (i.e. fluid kinetic energy responsible for erosion) along the barb-side bank remains reduced in reference to the mean flow. Spacing criteria refers to the placement (construction) distance between subsequent barb structures in the river reach.

Streambank Protection/Spacing Experiments

In order to investigate the length of streambank protected by the barb, large-scale particle image velocimetry (LSPIV) is utilized within a fixed-bed flume. The flume is a 19.5 m long, 0.89 m wide, 1.0 m deep water-recirculating flume and operates similarly to the recirculating flume used for the flow and scour experiments, but is longer and thus captures a reach farther downstream from the barb. Scaling ratios are adjusted to facilitate the longer reach, and thus a smaller model-barb is utilized. Table 7.1 presents flow conditions for the experiments. Manning's roughness, *n*, similarity is achieved after packing a fixed, angular-gravel bed.

Table 7.1. Flow conditions during barb testing for the streambank protection experiment.

S	*B*	*h*	*Q*	*Ubulk*	*Re*	*Fr*	*n*
m/m	m	m	m3/s	m/s	-	-	-
0.0045	0.89	0.055	0.027	0.54	30,000	0.73	0.016

LSPIV is an image-based technology that provides free-surface velocity vectors for open-channel research applications. Measurements are obtained by measuring the displacement of floating fluid-markers (i.e. seeded material) between successive digital images (Kjos 2003). For the present application, use of the LSPIV system relies on the assumption that free-surface velocities justly approximate mean-flow streamlines downstream of the barb.

To facilitate the LSPIV experiment, components, including: illumination, seeding, image recording, and image processing, are utilized. The image area is uniformly illuminated using four 75W-halogen lamps, two upstream and two downstream. Using a dimmer, a lighting scheme is established to suppress light reflection on the flow surface, which adversely affects the image-processing algorithm. The free-surface is seeded with 2-mm white Styropor expanded

polystyrene beads supplied by BASF Corporation. Uniform seeding is accomplished using a wire mesh shaker, located 300 cm upstream of the image area. Images are captured using a 30 Hz Canon Optura Pi Mini DV digital camcorder mounted directly above the image area. The seeded flow is recorded for two minute intervals. Image processing is facilitated by transferring data via a Compaq IEEE1394 Fire Wire connection, pre-processing data using *Adobe Photoshop 4.0.1*, and vector analysis using the *EdPIV* computer software. Within the software, velocity information is extracted using a two-dimensional cross-correlation algorithm applied to successive images. Results from 300 images are averaged to produce free-surface time-averaged velocity vectors, which are plotted using *Tecplot 8.0*.

Streambank Protection/Spacing Results

Figure 7.1 illustrates time-averaged, streamwise (U) velocity contours of the free-surface for the LSPIV experiment. Figure 7.1a depicts the velocity field for unobstructed flow (i.e. no barb present) for comparison with barb obstructed flow in Figure 7.1b. Figure 7.1b is created by connecting four LSPIV windows of the time-averaged results. Flow proceeds from left to right, and the black geometry symbolizes the barb; x- and y-axes represent streamwise and traverse directions (cm). Velocity contours are presented in units of m/s.

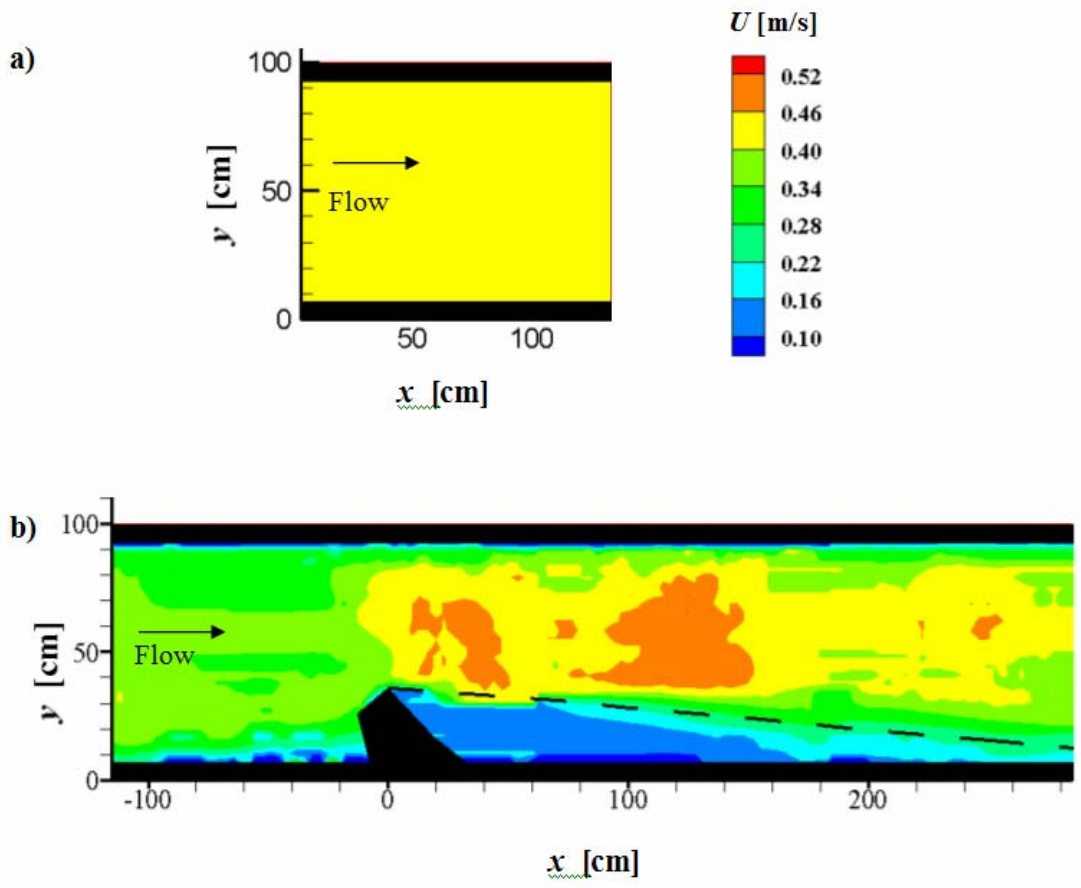

Figure 7.1. Time-averaged, streamwise (U) velocity contours of the free-surface for the LSPIV experiment. Plot (a) depicts the velocity field for unobstructed flow (i.e. no barb present) for comparison with barb obstructed flow in Figure 11b. Plot (b) is created by connecting four LSPIV windows of the time-averaged results. Flow proceeds from left to right, and the black geometry symbolizes the barb; x- and y-axes represent streamwise and traverse directions (cm). Velocity contours are presented in units of m/s.

Upstream of the model barb, the decelerating backwater regime spans the width of the channel, and is typified by relatively uniform flow for the cross-section. A small, slow moving dead zone exists near the flume wall, agreeing with the literature (e.g. Lu and Xu 1991). The constricted backwater flow accelerates at the barb nose, termed the main core, and thereafter expands upon downstream progression (Chow 1959; Rajaratnam and Nwachukwu 1983). The shear-layer and stagnant wake regions produce a reduction in U downstream of the barb, with small velocities at the bank, y=10 cm, and a gradual velocity increase across the flume in the positive y-direction. The reduced flow zone constitutes the streambank *protected region.* The non-uniform flow becomes uniform downstream, with expansion of the main core at the protected region extremity.

For an unsubmerged hydraulic structure, the protected region is separated, recirculating flow. Traditional experimental and numerical studies document the ratio between the protected region length and protrusion length (Y_p) of the hydraulic structure (i.e. the protrusion length is the perpendicular distance the barb extends from the streambank) on the order of 12-14 (Francis et al. 1968; Tingsanchali and Maheswaran 1990). For the partially submerged barb, it is necessary to define the protection region uniquely as the streamwise location where (1) flow uniformity resumes and (2) U at the streambank reaches 30% of the unobstructed, mean free-surface velocity (U_{fs}) (Here U_{fs} is 0.44 m/s.). Using this criteria, the protected region extent is approximately a dimensionless distance equal to 8. The protection region defined in this conservative manner indirectly incorporates additional safety. That is, protection region uncertainty is realized and incorporated due to scouring implications as typified in Section 6. Further, the uniform backwater region and small, slow moving dead zone upstream the barb are realized to impose further bank protection for the application of multiple barbs.

For determination of spacing criteria for successive barbs, a trial-and-error scenario is utilized to assess super-position of the backwater and protected region effects. Figure 7.2 illustrates LSPIV U contours for two barbs in succession. Figure 7.2a is a schematic of the LSPIV setup for the two barb experiments; flow proceeds from left to right, the outline of the two barbs is illustrated, and x- and y-axes represent streamwise and traverse directions (cm). In the experiments, the upstream barb is adjusted at various spacing ($S_p = X_b / Y_p$, where X_b is the distance between successive barbs and Y_p is the barb protrusion length), while the LSPIV imaging window and the downstream barb are fixed. Herein, results are presented for S varied to equal 15, 14, 13, and 12 as presented in Figure 7.2b, c, d, and e, respectively.

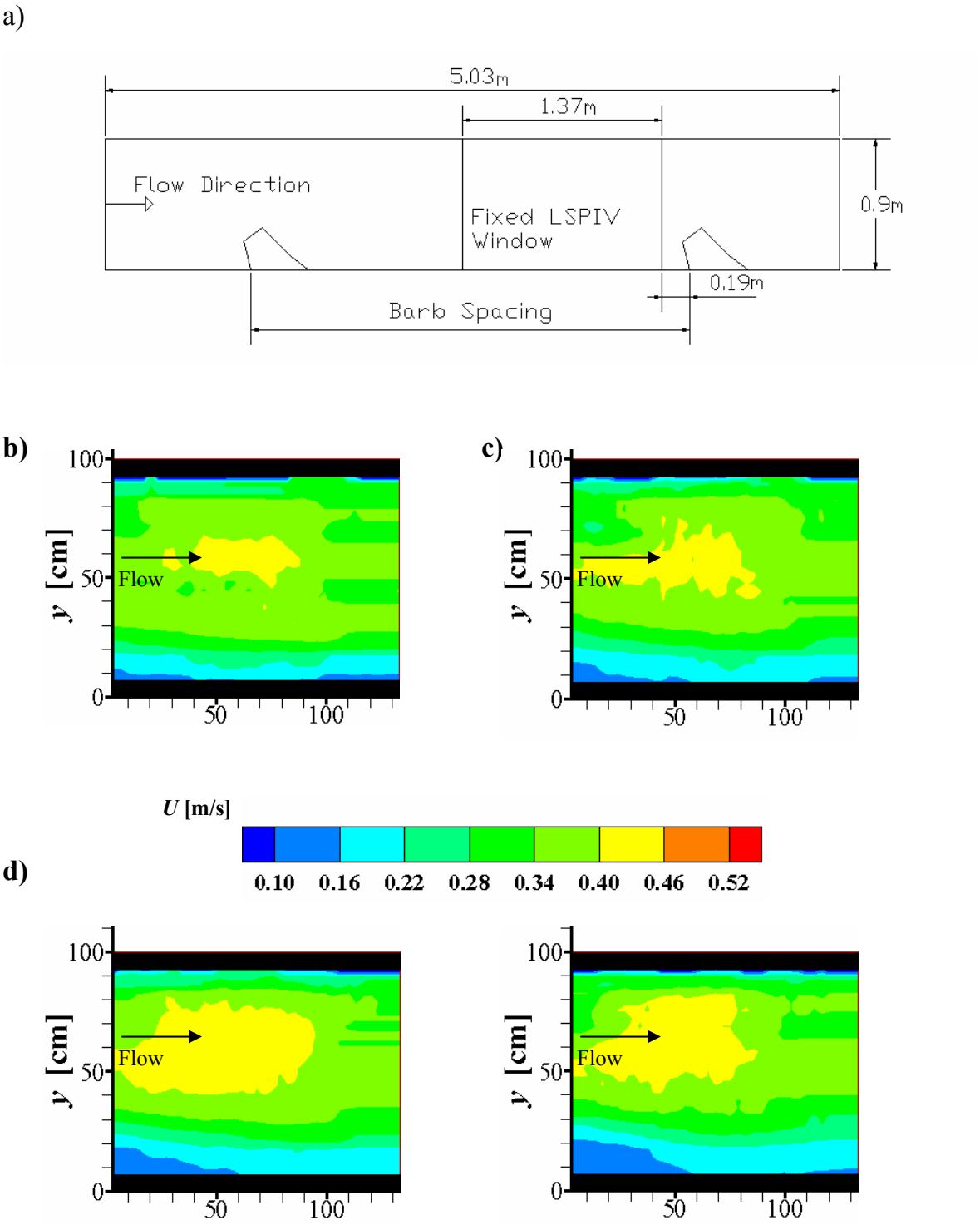

Figure 7.2. LSPIV *U* contours for two barbs in succession. Flow proceeds from left to right. The outline of the two barbs is illustrated, and *x*- and *y*-axes represent streamwise and traverse

directions (cm). S varied to equal 15, 14, 13, and 12 as presented in Figure 12b, c, d, and e, respectively.

For S_p equal to 15 and 14, flow uniformity dominates within the imaging window, as the main core and protected regions have diminished and only backwater from the downstream barb is apparent. S_p equal to 13 presents a threshold condition where main core acceleration and the protected region are still noticeable. The protected region connects with the small, slow moving dead zone of the downstream barb, and a condition persists whereby flow non-uniformity and U at the streambank less than 30% of U_{fs} persists. For S_p equal to 12, flow conditions again show non-uniformity and low U values at the streambank, thus justifying S_p = 13 as the threshold spacing for the barb application in a straight reach typical of mild-sloped, gravel-bed streams in the Pacific Northwest.

Conclusions from Objective 7:

Objective 7 provides dimensionless ratios for the barb protected region and spacing under channel-forming discharge conditions. Criteria is on the re-establishment of flow uniformity downstream of the barb separation zone and U at the streambank reaches 30% of the unobstructed, mean free-surface velocity. The downstream protected region, defined using the dimensionless ratio between the protected region length and protrusion length (Y_p) of the hydraulic structure, has a value of approximately 8. A barb spacing equal to 13, where 13 is the value of a dimensionless ratio, $S_p = X_b / Y_p$, where X_b is the distance between successive barbs and Y_p is the barb protrusion length.

Conclusions

Impact of Study

In the present study, the scour characteristics of barbs in mild sloped gravel bed streams were examined utilizing both an immobile and mobile bed configuration. This was accomplished through hydraulic modeling employing the governing parameters of hydraulic similitude. The collection of flow data and scour evolution was achieved in a controlled environment. Moreover, hydraulic modeling using gravel sediment, which is greatly lacking to date, was successfully modeled in this experiment. And lastly, a new insight to the partnership between scour evolution and velocity distribution was effectively explored.

Scour Prediction Stability of Design

The main goal of this research was to evaluate the scour effects induced by barbs during different flow states, and to provide a tool that enhances the design of stable structures. At maximum flow conditions, the maximum depth of scour produced was 21.7 cm. When compared to the predicted scour depth value of 40.0 cm for a flow rate that was 67% smaller (5 versus 3 times the critical flow rate) it is easily seen that existing equations largely over predict the scour extent; in this study by almost 85%. Analysis of the data from the model yielded an analytical expression that quantifies the equilibrium scour depth as a function of the geometric standard deviation of bed material sediment.

Stability of Design
Structure stability is a complex issue. Using the vertical scaling ratio of $Y_r = 7.12$, results in a prototype scour depth of 1.55 meters. The reader should be cautioned that in nature this depth is conservatively based due to the use of relatively uniform sediment. The other issue of contention is whether a flood event will realize the time required to reach equilibrium scour conditions. Even at a conservative level, it seems intuitive that the structure should be keyed into the channel bottom to alleviate slumping potential. This research provides a framework for future investigations.

New Design Performance
Modern hydraulic engineering, to a large extent, is based on experiment. As such, a modeler is faced with practical restraints such as time, money, and laboratory space. This research offers an inexpensive mode for gaining insightful knowledge on the performance of barb structures in the Pacific Northwest.

The complexity of flow around the WSDOT barb design and the prevalent distinct flow regimes (main core flow, shear layer region, and stagnant wake region) lend insight to the need for a different mode of shear stress determination. The trend to describe flow in nature using expressions for steady uniform flow conditions needs to be addressed. As shown in this research, 3-D turbulent flow conditions require these variables to be addressed for adequate predict.

Environmental Enhancements / Implications
Erosion control structures, such as barbs, supply an economical value to society in the protection of banks and bridges. The potential for environment and aquatic enhancements can be realized with the creation of slack water and resting pools on the leeward side of the barb. With almost any design in the natural environment there are pros and cons that need to be weighed. It is the hope that this thesis will provide information and stimulate new ideas to enhance environmental and economical hydraulic structures.

References

Abt, S. R., and Johnson, T. L. (1991). "Riprap design for overtopping flow." J. Hydr. Engrg., ASCE, 117(8), 959-972.

Abt., S. R., Johnson, T. L., Thornton, C. I., and Trabnant, S. C. (1998). "Riprap sizing at toe of embankment slopes." J. Hydr. Engrg., ASCE 124(7), 672-677.

Ackers, P., White, W.R., Perkins, J.A. and Harrison, A.J.M. Weirs and Flumes for Flow Measurement. John Wiley & Sons, Chichester: 1978.

Ahmad, M. (1953). "Experiments on design and behavior of spur-dikes." Proc., Minnesota International Hydraulic Convention, Minneapolis, Mn (Sept. 1953), 145-159.

Ahmed, F., and Rajarantnam, N. (2000). "Observations on flow around bridge abutments." J. Engrg. Mech., 126(1), 51-59.

Anderson, A. G., Praintal, A. S., and Davenport, J. T. (1970). "Tentative design procedure for riprap lined channels." Water Resour. Bull., 24(6), 1193-1200.

Beckstead, G. (1975). "Design condsiderations for stream groins." Technical Dept., Alberta Department of the Environment, Technical Services Div., Edmonton, Alberta, Canada.

Borah, D. K. (1989). "Scour-depth prediction under armoring conditions," J. Hydr. Engrg., ASCE, 115(10), 1421-1425.

Breusers, H. N. C., and Raudkivi, A. J. (1991). “Scouring.” Hydraulic structures design manual, No. 2, Balkema, Rotterdam, The Netherlands.
146
Buffington, J. M., Lisle, T. E., Woddsmith, R. D., and Hilton, S. (2002). “Controls on the size and occurrence of pools in coarse-grained forest rivers.” River Res. Applic., 18, 507-531.
Cardoso, A. H., and Bettess, R. (1999). “Effects of time and channel geometry on scour at bridge abutments,” J. Hydr. Engrg., 125(4), 388-399.
Chang, H. H. (1998). Fluvial processes in river engineering, Krieger Publishing Company, Malabar, Florida.
Chaudhry, M. H. (1993). Open-channel flow, Prentice Hall, Englewood Cliffs, New Jersey.
Chen, F. and Ikeda, S. (1997). “Horizontal separation flows in shallow open channels with spur dikes.” Journal of Hydroscience and Hydraulic Engineering, Vol. 15, No. 2, 15-30.
Cotton, G. K. (1998). “Riprap design at bridges – factor of safety approach.” Stream Stability and Scour at Highway Bridges, Compendium of Papers, ASCE Water Resources, Engineering Conferences, 1991 to 1998, 879-892.
Cunge, J. (1975). “Rapidly varying flow in power and pumping canals.” In Unsteady flow in open channels, (Edited by Mahmood. K. and Yevjevich, V.) 539-86. Water Resources Publication, Littleton, Colorado.
Cusick, C.F. Flow Meter Engineering Handbook, Third Edition. Minneapolis-Honeywell Regulator Company, Philadelphia: 1961.
Dinehart, R. L. (1992). “Evolution of coarse gravel bed forms: field measurements at flood stage.” Water Resource Research, 28(10), 2667-2689.
147
Dongol, D. M. S. (1993). “Local scour at bridge abutments,” PhD Thesis, Rep. No. 544, School of Engineering, University of Auckland, Auckland, New Zealand.
Escarameia, M. (1998). “River and channel revetments.” Thomas Telford Ltd., Heron Quay, London.
Espinosa, F. A., Rhodes, J. J., and McCullough, D. A. (1997). “The failure of existing plans to protect salmon habitat in the Clearwater National Forest in Idaho”. Journal of Environmental Management, 49, 205-230.
FHWA (1984). “Design of spur-type streambank stabilization structures.” Federal Highway Administration, Final Report No. FHWA/RD-84/101.
Fox, J. F. (2002). “Investigation of flow characteristics around submerged WSDOT barbs,” thesis, Washington State University.
Fox, J.F., Papanicolaou, A.N**.,** and Kjos, L. 2002, An Environmentally Friendly Barb in the State of Washington, Research and Extension Regional Water Quality Conference, February 20- 21, Vancouver, WA
Francis, J.R.D., Pattanaik, A.B. and Wearne, S.H. (1968). “Observations of flow patterns around some simplified groyne structures in channel.” Proceedings of Institution of Civil Engineering, Vol. 41, pp. 828-837.
Franzini, J., Finnemore, E. J., and Daugherty, R. (1997). “Fluid mechanics with engineering applications.” 9th ed., McGraw-Hill, New York.
Froehlich, D. C. (1989). “Local scour at bridge abutments.” Hydr. Engrg., 13-18.
Garde, R. J., Subramanya, K., and Nambudripad, K. D. (1961). “Study of scour around spur-dikes.” J. Hydraul. Div., ASCE, 87(HY6), 23-37.
148
Gessler, J. (1965). “The beginning of bedload movement of mixtures investigated as natural armoring channels.” Ph.D. thesis at the Swill Federal Institute of Technology.
Gessler, J. (1971). “Beginning and ceasing of sediment motion.” River Mechanics, Chapter 7, v.1, edited by H.W. Shen, Water Resources Publications, Fort Collins, Co.
Ghodsian, M. and Tehrani, S. M. H. (2001). “Scour around groins,” International Journal of Sediment Research, 16(1), 60-68.
Gill, M. A. (1970). “Bed ersosion around obstructions in rivers.” PhD. Thesis, University

of London, London, U. K.
Gill, M. A. (1972). “Erosion of sand beds around spur-dikes.” J. Hydraul. Div., ASCE, 98(9), 1587-1602.
Gill, M. A., (1981). “Bed erosion in rectangular long contraction.” J. Hydraul. Div., ASCE, 107(HY3), 273-284.
Heathershaw, A. D. and Simpson, J. H. (1978). “The sampling variability of the reynolds stress and its relation to boundary shear stress and drag coefficient measurements.” Estuarine and Coastal Marine Science, 6, 263-274.
Hunt, J., Brunner, G. E., and Larock, B. E. (1999). “Flow transition in bridge backwater analysis.” J. Hydr. Engrg., 125(9), 981-983.
Johnson, P. A., Hey, R. D., Tessier, M. and Rosgen, D. L. (2001). “Use of vanes for control of scour at vertical wall abutments,” J. Hydr. Engrg., ASCE, 127(9), 772-778.
Kaatz, K. J., and James, W. P. (1997). “Analysis of alternatives for computing backwater at bridges.” J. Hydr. Engrg., 123(9), 784-792.
Kilgore, R. T., and Young, G. K. (1993). “Riprap incipient motion and Shield’s parameter.” Proc. Nat’l Conf. on Hyd. Engrg., ASCE, New York, NY, 1552-1557.
149
Kim, S. C., Friedrichs, C. T., Maa, J. P. Y., and Wright, L. D. (2000). “Estimating bottom shear stress in tidal boundary layer from acoustic doppler velocimeter data.” J. Hyd. Engr., 126(6), 399-406.
Kimura, I., and Hosoda, T. (1997). “Fundamental properties of flows in open channels with dead zone.” J. Hydr. Engrg., ASCE, 123(2), 98-107.
Klingeman, P. C., Kehe, S. M., and Owusu, Y. A. (1984). “Streambank erosion protection and channel scour manipulation using rockfill dikes and gabions.” Rep. No. WRRI-98, Water Resources Institute, Oregon State Univ., Corvallis, Or.
Kong, X. and Cheng, N. (1990). “An experimental study of local head losses at spur dikes.” Proceedings of the 7th Congress APD-IAHR, 273-278.
Kothyari, U. C., and Ranga Raju, K. G. (2001). “Scour around spur dikes and bridge abutments.” Journal of Hydraulic Research, Vol. 39(4), 367-374.
Kothyari, U. C., and Ranga Raju, K. G. (2002). “Scour around spur dikes and bridge abutments.” J. Hydr. Research, 39(4), 367-374.
Kouchakdeh, S., and Townsend, D. R. (1997). “Maximum scour depth at bridge abutments terminating in the floodplain zone.” Can. J. Civ. Engrg., 24(6), 96-1006.
Kuhnle, R. A., Alonso, C. A. and Shields Jr., F. D. (1998). “Volume of scour holes for angled spur dikes,” Water Res. Engrg., 2, 1613-1618.
Kuhnle, R. A., Alonso, C. A. and Shields Jr., F. D. (1999). “Geometry of scour holes associated with 90 degree spur dikes,” J. Hydr. Engrg., ASCE, 125(9), 972-978.
Kuhnle, R. A., Alonso, C. A. and Shields Jr., F. D. (2002). “Local scour associated with angled spur dikes,” J. Hydr. Engrg., 128(129), 1087-1093.
150
Kwan, T. F. (1984). “Study of abutments.” Rep. No. 328, School of Engineering, Univ. of Auckland, Auckland, New Zealand.
Kwan, T. F. (1988). “A study of abutment scour.” Rep. No. 451, Dept. of Civil Engineering, Univ. of Auckland, Auckland, New Zealand.
Lagasse, P. F., Schall, J. D., Johnson, F., Richardson, E.V., and Chang, F. (1995). “Stream stability at highway structures.” Report No. FHWA IP-90-014, HEC-20, FHWA.
Laursen, E. M. (1960). “Scour at bridge crossings.” J. Hydraul. Div., ASCE, 86(HY2), 162-180.
Laursen, E. M. (1962). “Scour at bridge crossings.” Transactions, ASCE 127, Part I. 116-179.
Laursen, E. M. (1963). “An analysis of relief bridge scour.” J. Hydraul. Div., ASCE, 89(HY3), 93-118.
Laursen, E. M., and Toch, A. (1953). “A generalized model study of scour around bridge piers and abutments.” Proc., Minnesota International Hydraulic Convention, Minneapolis, Mn (Sept. 1953), 123-131.

Lim, S. Y. (1997). “Equilibrium clear-water scour around an abutment.” J. Hyd. Engr., 123(3), 237-243.
Lim, S. Y., and Cheng, N. S. (1998). “Prediction of live-bed scour at bridge abutments.” J. Hydr. Engrg., ASCE, 124(6), 635-638.
Lim, S. Y., and Yu, G. (2001). “Study of abutment scour in two-stage channels.” Proc. XXIX IAHR Congress – 21st Century: The Era for Hydraulics Research and its Applications, Beijing, China, Vol. II, Theme D, September 16-21, 8-13.
151
Liu, H. K., Chang, F. M., and Skinner, M. M. (1961). “Effect of bridge constriction on scour and backwater.” Report No. CER60HKL22, Civil Engineering Section, Colorado State University, Fort Collins, Co.
Lloyd, P. M. and Stansby, P. K. (1997). “Shallow-water flow around model conical islands of small side slope. II: submerged.” J. Hyd. Engr., ASCE, 123(12), 1068-1077.
“Loose-boundary flow,” (2000). Hydraulic Modeling: Concepts and Practice, Chapter 4, ASCE Manuals and Reports on Engr. Practice, 97, ASCE, VI, 89-117.
Lu, Yong-jun and Xu, Cheng-wei (1991). “Advances in flow near groin-like structures.” Journal of Hydrodynamics, Ser.b, 3, 57-64.
Lyons, J., Trimble, S. W., Paine, L. K. (August 2000). “Grass versus trees: managing riparian areas to benefit streams of Central North America”. Journal of the American Water Resources Association, 919-930.
Maxwell, A. R., and Papanicolaou, A. N. (2001). “Step-pool morphology in highgradient streams.” International Journal of Sediment Research, 16(3), 380-390.
Mayerle, R., Toro, F.M., and Wang, S.S.Y. (1995). “Verification of a three-dimensional numerical model simulation of the flow in the vicinity of spur dikes.” Journal of Hydraulic Research, Vol. 33, No. 2, 243-256.
Maynord, S. T., Ruff, J. F., and Abt, S. R. (1989). “Riprap design.” J. Hydr. Engrg., 115(7), 937-949.
Melville, B. W. (1992). “Local scour at bridge abutments.” J. Hydr. Engrg., ASCE, 118(4), 615-631.
152
Melville, B. W. (1995). “Bridge abutment scour in compound channels.” J. Hydr. Engrg., ASCE, 121(12), 863-868.
Melville, B. W. (1997). “Pier and abutment scour – an integrated approach.” J. Hydr. Engrg., ASCE, 123(2), 125-136.
Melville, B. W., and Coleman, S. E. (2000). Bridge scour, Water Resources Publications, LLC, Highlands Ranch, Co.
Molinas, A., Kheireldin, K., and Wu, B. (1998). “Shear stress around vertical wall abutments.” J. Hydr. Engrg., 124(8), 822-829.
Nikora, V., and Goring, D. (2000). “Flow turbulence over fixed and weakly mobile gravel beds.” J. Hydr. Engrg., 126(9), 679-690.
Nwachukwu, B. A., and Rajaratnam, W. (1980). “Flow and erosion near groyne-like structures.” Dept. of Civil Eng., Univ. of Alberta, Edomonton, Alberta.
Odgaard, A.J and Kennedy, J.F. (1983). “River-bend bank protection by submerged vanes.” J. Hyd. Engr., Vol. 109, No. 8, 1161-1173.
Ohtsu, I., Yasuda, Y., and Yamanaka, Y. (1997). “Submerged flow regimes of rectangular sharp-crested weirs: discussion.” J. Hyd. Engr., ASCE, 927-929.
Papanicolaou, A. N. (1997). “The role of turbulence in the initiation of sediment motion,” Ph.D. dissertation, Virginia Polytechnic Institute and State University.
Papanicolaou, A. N., and Hilldale, R. (2002). “Turbulence characteristic in a gradual channel transition.” J. of Engrg., ASCE, 128(9), 948-961.
Peng, J., Tamai, N., Kawahara, Y. and Huang, G. W. (1999). “Numerical modeling of local scour around spur dikes,” International Conference in Geomorphology, Genova, Italy.
153
Przedwojski, B. (1995). “Bed topography and local scour in rivers with banks protected

by groynes," J. Hydr. Res., 33(2), 257-273.
Przedwojski, B., Blazejewski R., and Pilarczyk, K. W. (1995). "River Training Techniques." A.A. Balkema, Rotterdam, Brookfield, Vt.
Rajaratnam, N. and Nwachukwu, B.A. (1983). "Flow near groin-like structures." J. Hyd. Engr., ASCE, Vol. 21, No. 4, pp. 277-287.
Rice, C. E., Kadavy, K. C., and Robinson, K. M. (198). "Roughness of loose rock riprap on steep slopes." J. Hydr. 124(2), 179-185.
Richardson, E. V., and Davis, S. R. (1995). "Evaluating scour at bridges." Publication No. FHWA HI-96-031, HEC 18, FHWA.
Richardson, E. V., Simons, D. B., and Julien, P. (1990). "Highways in the river environment." FHWA-HI-90-016, U. S. Dept. of Transportation, Washington, D. C.
Richardson, J. R., and Richardson, E. V. (1993). "The fallacy of local abutment scour equations." Hydr. Engrg., '93, Proc., 1993 Conf. of the Hydr. Div., Vol. 1, ASCE, Reston, Va., 749-754.
Roberson, J. A. and Crowe, C. T. (1997). Engineering fluid mechanics, 6th ed., John Wiley & Sons, Inc., USA.
Rosgen, D. L. (1994). "A classification of natural rivers." Catena, 22, 169-19.
Schmidt, J. C., Rubin, D. M., and Ikeda, H. (1993). "Flume simulation of recirculating flow and sedimentation." Water Resources Research, AGU, 29, 2925-2939.
Shamloo, H., Rajaratnam, N., and Katopodis, C. (2001). "Hydraulics of simple habitat structures." Journal of Hydraulic Research, Vol. 39(4), 351-366.
154
Shields, F. D., Jr., Cooper, C. M., and Testa, S. (1995). "Towards greener riprap: environmental considerations for micro- to macro-scale." River, coastal and shoreline protection: erosion control using riprap and armourstone, C. R. Thorne, S. R. Abt, F. B. J. Barends, S. T. Maynord, and K. W. Pikarczyk, eds., Wiley, Chichester, U. K., 557-574.
Sirovich, L., and Karlsson, S., (1997). "Turbulent drag reduction by passive mechanisms." J. Hydr. Engrg. 388, 753-755.
Sklenar, P. (2002). "Evaluation of flow resistance in straight channel with a group of spur dikes." River Flow 2002, Proc. of the International Conf. on Fluvial Hydraulics, Vol. 1, Louvain-La-Neuve, Belgium, 385-393.
Soulsby, R. L. (1983). "The bottom boundary layer of shelf seas', in Johns, B. (Ed.), Physical Oceanography of Coastal and Shelf Seas, Elsevier Oceanography Series, 35, Amsterdam, Ch. 5B.
Stapleton, K. R. and Huntley, D. A. (1995). "Seabed stress determinations using the inertial dissipation method and the turbulent kinetic energy method." Earth Surface Processes and Landforms, 20, 807-815.
"Streambank Stabilization Handbook," (1998). Surface Armor for Erosion Protection, Chapter 7, U.S. Army Corps of Engineers and Veri-Tech Incorporated.
Strum, T. W., and Janjua, N. S. (1994). "Clear-water scour around abutments in floodplains." J. Hydr. Engrg., 120(8), 956-972.
Sturm, T. W. (1998). "Abutment scour in compound channel." Stream Stability and Scour at Highway Bridges, ASCE, Reston, VA, 443-456.
155
Sturm, T. W., and Janjua, N. S. (1993). "Bridge abutment scour in a floodplain." Proc. Nat. Conf. On Hydraulics, ASCE, New York, NY, 761-766.
Sturm, T. W., and Sadiq, A. (1996). "Water surface profiles in compound channel with multiple critical depths." J. Hydr. Engrg., ASCE, 122(12), 703-709.
Sukhodolov, A., Englehardt, C., Kruger, A. and Bungartz, H. (2000). "A pilot study of turbulent flow and sediment distributions in a groyne field," Department of Ecohydrology, Institute of Freshwater Ecology and Inland Fisheries, Berlin, Germany.
Sukhodolov, A., Thiele, M., and Bungartz, H. (1998). "Turbulence structure in a river with sand bed." Water Resour. Res., 34(5), 1317-1334.
Tillamook County Soil and Water Conservation District, web: www.co.tillmook.or.us/gov/estuary/tbnep/barbs2.html

Tipping, E., Woof, C. and Clarke, K. (1993). “Deposition and resuspension of fine particles in a riverine,” Hydr. Procs. 7, 263-277.
U. S. Bureau of Reclamation (1974). “Design of small dams, a water resource technical publication, U. S. Govt. Printing Office, Washington, D.C..
U. S. Department of Transportation, Federal Highway Administration, (1985). “Design of spur-type streambank stabilization structures.” Report No. FHWA/RD-84/101, McLean, Virginia.
Uijttewaal, W. S. J., Berg, M. H., and van der Wal, M. (2002). “Experiments on physical scale models for submerged and non-submerged groynes of various types.” River Flow 2002, Proc. of the International Conf. on Fluvial Hydraulics, Vol. 1, Louvain-La-Neuve, Belgium, 377-383.
156
Uijttewaal, W.S.J., Lehmann, D. and van Mazijk, A. (2001). “Exchange processes between a river and its groyne fields: model experiments.” J. Hyd. Engr., ASCE, Vol. 127, No. 11, 928-936.
United Panels.com website: http://www.unitedpanel.com/, August 21, 2002.
Wallerstein, N. P. (2003). “Dynamic model for constriction scour caused by large woody debris.” Earth Surf. Process. Landforms, 28, 49-68.
Wang, S., and Shen, H. (1985). “Incipient motion and riprap design.” J. Hydr. Engrg., ASCE, 111(3), 520-538.
Web: www.wa.usgs.gov
Whitehouse, R. J. S. (1997). “Scour at marine structures: A manual for engineers and scientists.” Res. Rep. SR417, HR Wallingford Ltd., Wallingford, U.K.
Whiting, P., and Dietrich, W. (1990). “Boundary shear stresses and roughness over mobile alluvial beds.” J. Hydr. Engrg., 116, 1495-1511.
Wu, S. and Rajaratnam, N. (1996). “Submerged flow regimes of rectangular sharpcrested weirs.” J. Hyd. Engr., ASCE, 122(7), 412-414.
Xiangbai, K., and Niansheng, C. (1990). “An experimental study of local head looses at spur dikes.” 7th Congress APD-AIHR, Beijing, Korea (November), 273-278.
Yalin, M. S. (1971). “On the foundation of dunes and meanders.” Proc. Of the 14th International National Congress of the Hydraulic Research Association, Paris, 1-8.
Yong-jun, L. and Cheng-wei, X. (1991). “Advances in flow near groin-like structures,” J.Hydrodynamics, Ser. B, 3, 57-64.
Zaghloul, N. A. (1983). “Local scour around spur dikes,” J. Hydr. 60, 123-140.